

AFATL-TR-89-19

AD-A212 377

①

# Unsteady Three-Dimensional Thin-Layer Navier Stokes Solutions on Dynamic Blocked Grids

---

L Bruce Simpson

AERODYNAMICS BRANCH  
AEROMECHANICS DIVISION

MAY 1989

FINAL REPORT FOR PERIOD AUGUST 1986 - DECEMBER 1988

APPROVED FOR PUBLIC RELEASE; DISTRIBUTION UNLIMITED

SDTICD  
ELECTE  
JUN 16 1989  
H

AIR FORCE ARMAMENT LABORATORY

Air Force Systems Command ■ United States Air Force ■ Eglin Air Force Base, Florida

89

6

15

069

## REPORT DOCUMENTATION PAGE

Form Approved  
OMB No. 0704-0188

1a. REPORT SECURITY CLASSIFICATION			1b. RESTRICTIVE MARKINGS			
2a. SECURITY CLASSIFICATION AUTHORITY			3. DISTRIBUTION/AVAILABILITY OF REPORT Approved for public release; distribution unlimited.			
2b. DECLASSIFICATION/DOWNGRADING SCHEDULE						
4. PERFORMING ORGANIZATION REPORT NUMBER(S)			5. MONITORING ORGANIZATION REPORT NUMBER(S) AFATL-TR-89-19			
6a. NAME OF PERFORMING ORGANIZATION Aerodynamics Branch Aeromechanics Division		6b. OFFICE SYMBOL (if applicable) AFATL/FXA		7a. NAME OF MONITORING ORGANIZATION Aerodynamics Branch Aeromechanics Division		
6c. ADDRESS (City, State, and ZIP Code) Air Force Armament Laboratory Eglin Air Force Base, FL 32542-5434			7b. ADDRESS (City, State, and ZIP Code) Air Force Armament Laboratory Eglin Air Force Base, FL 32542-5434			
8a. NAME OF FUNDING/SPONSORING ORGANIZATION Air Force Armament Laboratory		8b. OFFICE SYMBOL (if applicable) AFATL/FXA		9. PROCUREMENT INSTRUMENT IDENTIFICATION NUMBER		
8c. ADDRESS (City, State, and ZIP Code) Eglin Air Force Base, FL 32542-5434			10. SOURCE OF FUNDING NUMBERS			
			PROGRAM ELEMENT NO. 61102F	PROJECT NO. 2307	TASK NO. E1	WORK UNIT ACCESSION NO. 26
11. TITLE (Include Security Classification) Unsteady Three-Dimensional Thin-Layer Navier Stokes Solutions on Dynamic Blocked Grids						
12. PERSONAL AUTHOR(S) L. Bruce Simpson						
13a. TYPE OF REPORT Final		13b. TIME COVERED FROM Aug 86 to Dec 88		14. DATE OF REPORT (Year, Month, Day) May 1989		15. PAGE COUNT 147
16. SUPPLEMENTARY NOTATION This report was a thesis; therefore it is not in the AFATL technical report format.						
17. COSATI CODES			18. SUBJECT TERMS (Continue on reverse if necessary and identify by block number) Computational Fluid Dynamics Unsteady Aerodynamics Navier-Stokes Equations			
FIELD	GROUP	SUB-GROUP				
01	01					
19. ABSTRACT (Continue on reverse if necessary and identify by block number)  An efficient scheme for calculating steady and unsteady solutions on blocked grids for several airfoils and wings is presented. Two algorithms are presented, both of which are based on upwind, finite-volume, flux splitting for the convective terms, and an explicit treatment of the diffusive terms. The first algorithm is based on a flux-vector split (FVS) scheme while the second algorithm is based on a flux-difference split (FDS) scheme.  The two algorithms are compared for steady thin-layer Navier-Stokes solutions on a laminar flat plate, RAE 2822 airfoil, and the ONERA M6 wing. The FDS scheme proved to be superior to the FVS in all cases, due to the excessive numerical dissipation in the FVS scheme. A flat plate laminar boundary layer profile is shown with the FDS scheme correctly modeling the boundary layer (compared to a Blasius solution) with only three grid cells internal to the boundary layer; the FVS scheme was not capable of correctly modeling the boundary layer profile.						
20. DISTRIBUTION/AVAILABILITY OF ABSTRACT <input type="checkbox"/> UNCLASSIFIED/UNLIMITED <input type="checkbox"/> SAME AS RPT. <input type="checkbox"/> DTIC USERS			21. ABSTRACT SECURITY CLASSIFICATION UNCLASSIFIED			
22a. NAME OF RESPONSIBLE INDIVIDUAL L. Bruce Simpson			22b. TELEPHONE (Include Area Code) 904-882-3124		22c. OFFICE SYMBOL AFATL/FXA	

UNCLASSIFIED

19. ABSTRACT. (concluded)

The FDS algorithm was used to evaluate the scheme for unsteady viscous calculations. The diffusive terms are time-lagged in the solution process and therefore are treated as source terms to the convective terms, which behave as a hyperbolic set of equations. The scheme is second order accurate in space and first order accurate in time due to the explicit treatment of the diffusive terms. A Newton subiteration technique was implemented to allow for larger time step sizes and second order temporal accuracy. The subiterations are more efficient than a normal time step iteration since the flux Jacobians need not be updated for the subiterations. The result is a more efficient and robust unsteady thin-layer Navier-Stokes algorithm which shows extremely good comparison with unsteady experimental data for oscillating airfoils (NACA 0012) and wings (Langley Rectangular Planform Supercritical Wing), even for calculations using large Courant numbers as high as 45,000.

Engineering solutions for oscillating airfoils and wings can be obtained using the algorithm presented. Accurate viscous results can be obtained at a cost near that of inviscid results (on the same grid), yet with the inclusion of the time-lagged viscous terms the results are superior to those obtained using inviscid schemes.

Accession For	
NTIS GRA&I	<input checked="checked" type="checkbox"/>
DTIC TAB	<input type="checkbox"/>
Unannounced	<input type="checkbox"/>
Justification	
By _____	
Distribution/	
Availability Codes	
Dist	Avail and/or Special
A-1	

UNCLASSIFIED

## PREFACE

This report describes an in-house effort performed by L. Bruce Simpson of the Aeromechanics Division (FXA), Air Force Armament Laboratory (AFATL), Eglin Air Force Base, Florida. The work reported covers the time period of September 1986 to December 1988.

## ACKNOWLEDGEMENTS

I would like to express my appreciation to the Air Force Armament Laboratory for supporting this work, in particular for providing the computer resources. I thank Mr. Steve Korn and Dr. Dave Belk for their support and help during this research period. I would also like to thank Dr. David Whitfield, of Mississippi State University (MSU), my major advisor, and Dr. Boyd Gatlin also of MSU for their help.

# TABLE OF CONTENTS

Section	Title	Page
I.	Introduction. . . . .	1
II.	Navier-Stokes Equations . . . . .	5
	2.1 Vector Form of the Navier-Stokes Equations .	5
	2.2 Curvilinear Coordinate Transformation. . . .	9
	2.3 Thin Layer Navier-Stokes Equations . . . . .	9
III.	Description of Splitting Techniques. . . . .	13
	3.1 Basic Implicit Algorithm. . . . .	13
	3.2 Flux Vector Splitting . . . . .	14
	3.3 Flux Difference Splitting . . . . .	16
	3.4 Flux Vector Splitting for Three Dimensions. .	21
	3.5 Flux Difference Splitting for Three Dimensions . . . . .	26
IV.	Thin Layer Navier-Stokes Algorithm. . . . .	32
	4.1 Explicit Treatment of Viscous Terms. . . . .	32
	4.2 Boundary Conditions. . . . .	34
	4.3 Turbulence Modeling. . . . .	36
	4.4 Time Accuracy and Subiterations. . . . .	38
V.	Steady Results. . . . .	49
	5.1 Flat Plate Boundary Layer. . . . .	49
	5.2 RAE 2822 Airfoil . . . . .	50
	5.3 ONERA M6 Wing. . . . .	54
VI.	Unsteady Results. . . . .	57
	6.1 Oscillating NACA 0012 Airfoil. . . . .	57
	6.2 Oscillating Supercritical Rectangular Planform Wing . . . . .	60
VII.	Conclusions . . . . .	64
TABLES. . . . .		66
FIGURES . . . . .		70
APPENDIX A. Curvilinear Transformation . . . . .		139
References . . . . .		145

# LIST OF TABLES

Table	Title	Page
I.	Second Order Truncation Error . . . . .	67
II.	Summary of Time Step Size Runs. . . . .	68
III.	Summary of Subiteration Runs. . . . .	69

# LIST OF FIGURES

Figure	Title	Page
3.1	Characteristic waves. . . . .	19
4.1	No-slip boundary conditions for dynamic grids . . . . .	35
1.	"C" grid for NACA 0012 airfoil	
a.	221 points in the streamwise direction, 40 points in the normal direction. . . . .	71
b.	Closeup of NACA 0012 section . . . . .	72
2.	Unsteady pressure distribution for different time step sizes . . . . .	73
3.	Unsteady pressure distributions using minimum time step subiterations for first 60 deg of motion $DT=.0511$ . . .	74
4.	Unsteady pressure distributions using minimum time step subiterations for first 60 deg of motion $DT=.2044$ . . .	75
5.	Unsteady pressure distributions using local time step subiterations for first 60 deg of motion $DT=.0511$ . . .	76
6.	Unsteady pressure distributions using local time step subiterations for first 60 deg of motion $DT=.2044$ . . .	77
7.	Unsteady pressure distributions using both min and local subiterations for first 60 deg of motion $DT=.0511$ . . .	78
8.	Unsteady pressure distributions using 1st and 2nd order schemes, 16 min time step subiterations . . . . .	79
9.	Velocity profiles for laminar flat plate. . . . .	80
10.	"C" grid for RAE 2822 airfoil (221x31x2). . . . .	81
11.	Comparison of minmod 2nd order with EMULE for the RAE 2822	
a.	Steady pressure distributions . . . . .	82
b.	Boundary layer velocity profiles at 32% chord (upper surface) . . . . .	83
c.	Boundary layer velocity profiles at 57% chord (upper surface) . . . . .	84
d.	Upper surface skin friction . . . . .	85
12.	Comparison of minmod 3rd order with EMULE for the RAE 2822	
a.	Steady pressure distributions . . . . .	86
b.	Boundary layer velocity profiles at 32% chord	

	(upper surface) . . . . .	87
c.	Boundary layer velocity profiles at 57% chord (upper surface) . . . . .	88
d.	Upper surface skin friction . . . . .	89
13.	Comparison of superbee 2nd order with EMULE for the RAE 2822	
a.	Steady pressure distributions . . . . .	90
b.	Boundary layer velocity profiles at 32% chord (upper surface) . . . . .	91
c.	Boundary layer velocity profiles at 57% chord (upper surface) . . . . .	92
d.	Upper surface skin friction . . . . .	93
14.	Convergence histories for Roe and EMULE schemes . . . .	94
15.	"C-O" wing grid for the ONERA M6 wing	
a.	111 points in the streamwise direction, 40 points in the normal direction. . . . .	95
b.	Distribution of constant spanwise location planes along the wing. . . . .	96
c.	ONERA M6 wing tip model . . . . .	97
16.	Steady pressure distributions for ONERA M6 wing comparing Roe and EMULE schemes	
a.	44% semispan location . . . . .	98
b.	65% semispan location . . . . .	99
c.	95% semispan location . . . . .	100
17.	Pressure contours for ONERA M6 wing using minmod 3rd	
a.	44% semispan location . . . . .	101
b.	65% semispan location . . . . .	102
c.	95% semispan location . . . . .	103
d.	Upper surface pressure contours . . . . .	104
18.	Comparisons of Lift and moment coefficients using 4 min and 4 local subiterations	
a.	Lift coefficient versus time. . . . .	105
b.	Moment coefficient versus time. . . . .	106
19.	Three block version of "C" grid for NACA 0012 . . . . .	107
20.	Unsteady pressure distributions for 1 and 3 blocks	
a.	25 deg of oscillatory motion, AOA increasing ( 1.09) .	108
b.	70 deg of oscillatory motion, AOA increasing ( 2.37) .	109
c.	115 deg of oscillatory motion, AOA decreasing ( 2.29) .	110
d.	160 deg of oscillatory motion, AOA decreasing ( 0.87) .	111
e.	205 deg of oscillatory motion, AOA decreasing (-1.04) .	112
f.	250 deg of oscillatory motion, AOA decreasing (-2.34) .	113
g.	295 deg of oscillatory motion, AOA increasing (-2.26) .	114
h.	338 deg of oscillatory motion, AOA increasing (-0.84) .	115



21.	Pressure contours for 3 block NACA 0012 at 360 deg of oscillatory motion . . . . .	116
22.	Unsteady pressure distributions for 1st and 2nd order time accuracy using 4 min subiterations and DT=.0511	
a.	25 deg of oscillatory motion . . . . .	117
b.	70 deg of oscillatory motion . . . . .	118
c.	115 deg of oscillatory motion . . . . .	119
d.	160 deg of oscillatory motion . . . . .	120
e.	205 deg of oscillatory motion . . . . .	121
f.	250 deg of oscillatory motion . . . . .	122
g.	295 deg of oscillatory motion . . . . .	123
h.	338 deg of oscillatory motion . . . . .	124
23.	"C-H" grid for rectangular supercritical wing	
a.	221 points in the streamwise direction, 40 points in the normal direction. . . . .	125
b.	Distribution of constant spanwise location planes along the wing. . . . .	126
24.	Steady pressure distributions for the rectangular supercritical wing compared with experiment	
a.	34% semispan calculated, 31% experiment . . . . .	127
b.	61% semispan calculated, 58% experiment . . . . .	128
c.	85% semispan calculated, 82% experiment . . . . .	129
d.	95% semispan calculated, 95% experiment . . . . .	130
25.	Magnitude and phase of unsteady rectangular wing pressure distributions	
a.	Magnitude at 34% semispan . . . . .	131
b.	Phase at 34% semispan . . . . .	132
c.	Magnitude at 61% semispan . . . . .	133
d.	Phase at 61% semispan . . . . .	134
e.	Magnitude at 85% semispan . . . . .	135
f.	Phase at 85% semispan . . . . .	136
g.	Magnitude at 95% semispan . . . . .	137
h.	Phase at 95% semispan . . . . .	138

# NOMENCLATURE

## English Letters

a	speed of sound
A,B,C	Jacobian of the flux vectors F,G,H
AOA	angle of attack
c	chord length
$C_{cp}$	constant in turbulence model
$C_p$	pressure coefficient; constant pressure specific heat
$C_f$	skin friction coefficient
$C_{kleb}$	constant in turbulence model
$C_v$	constant volume specific heat
$C_{wk}$	constant in turbulence model
CFL	Courant Number
DT	time step size
e	energy per unit volume
f,g,h	Cartesian coordinate flux vectors
F,G,H	Curvilinear coordinate flux vectors
$F_w$	function in turbulence model
I	identity operator
J	Jacobian of inverse transformation $\frac{\partial(x,y,z)}{\partial(\xi,\eta,\zeta)}$
$J'$	$\frac{\partial(x,y,z,t)}{\partial(\xi,\eta,\zeta,\tau)}$
k	reduced frequency or Strouhal number
K	Clauser constant
l	Prandtl mixing length
$l_r$	reference length
M	Mach number
p	pressure
$P_r$	Prandtl number
q	Cartesian coordinate dependent vector
Q	Curvilinear coordinate dependent vector
R	residual vector
$Re_l$	Reynolds number based on reference length
s	tensor of diffusive fluxes
t	time
T	temperature
u,v,w	Cartesian coordinate velocities
U,V,W	contravariant velocities
$\vec{V}$	total velocity
x,y,z	Cartesian coordinates
Y	normal distance from point to solid surface
$Y'$	inner variable length scale in turbulence model

## Greek Letters

$\alpha$	angle of attack
$\alpha_0$	mean angle of attack
$\alpha_u$	amplitude of unsteady angle of attack
$\gamma$	ratio of specific heats, $C_p/C_v$
$\delta$	central difference operator
$k$	von Karman constant

$\lambda$	second coefficient of viscosity; eigenvalue of flux jacobian matrix
$\mu$	fluid dynamic viscosity
$\nu$	fluid kinematic viscosity
$\xi, \eta, \zeta$	computational coordinates
$\rho$	mass density
$\tau$	time in computational space; fluid stress vector
$x$	distance from trailing edge for turbulence model
$\omega$	oscillatory frequency; vorticity

#### Subscripts

$b$	boundary point
$c$	based on chord length
$f$	field point
$i, j, k$	in the $\xi, \eta, \zeta$ direction
$l$	based on characteristic length; index on eigenvalue and corresponding flux component
$p$	phantom point
$t$	time differentiation
$x, y, z$	space differentiation
$\xi, \eta, \zeta$	differentiation
$\infty$	freestream reference value

#### Superscripts

$d$	diffusive quantity
$i$	computational coordinates index ( $i=1,2,3$ )
$T$	transpose of matrix
$n$	previous time level
$n+1$	current time level
$-1$	inverse of matrix
	dimensional quantity

## SECTION I

### INTRODUCTION

The area of Computational Fluid Dynamics (CFD) has seen tremendous progress in recent years, due to improvements in both computational algorithms and computer hardware. The improvements now make it possible to obtain steady inviscid solutions for very complex configurations such as modern fighter aircraft and the external weapons used on these aircraft (Reference 1). However, many of these aircraft and weapons operate in flow conditions which make inviscid solutions an inappropriate model. Modern fighter aircraft must be able to release stores and missiles while maneuvering at transonic speeds. The analysis of these problems requires unsteady calculations, as does the analysis of aeroelastic problems. Many modern fighter aircraft have internal bays in which to carry their weapons. The analysis of these problems requires that a highly separated unsteady flow field be solved. Solutions which include the effects of viscosity are necessary to appropriately model these flow fields; however, for these types of configurations viscous solutions are not practical with current CFD codes, due to the large computer run times and large memory requirements. The emphasis of the work presented here is development of a scheme which is computationally efficient and accurate enough to make viscous calculations possible for the design and analysis of these configurations in steady and unsteady flow fields.

The approach taken is an extension of two Euler algorithms described by Belk<sup>2</sup> and Whitfield<sup>3</sup>. The schemes used in this work are first, a flux vector split scheme based on Steger-Warming<sup>4</sup> splitting

and secondly, a flux difference split scheme based on Roe's<sup>5</sup> approximate Riemann solver. The inclusion of the viscous terms into these Euler algorithms is accomplished as described by Gatlin<sup>6</sup>, where the viscous terms have been added to the algorithm explicitly, in order to save the cost of computing and storing the viscous flux jacobians. The explicit treatment of the diffusive terms also preserves the computational efficiency peculiar to the inviscid algorithm.

The three-dimensional Navier-Stokes equations in differential form are presented in Section II. The curvilinear coordinate transformation and the thin-layer assumption to reduce the Navier-Stokes equation set are also presented.

A comparison of the two basic implicit algorithms is presented in Section III. A short discussion is presented which compares and contrasts the two splitting techniques, flux vector splitting (FVS) and flux difference splitting (FDS). The advantages and disadvantages of the two algorithms are discussed, with the discussion based on the one-dimensional Euler equations. The two algorithms are then extended to the three-dimensional Euler equations. The FVS algorithm has been presented in some detail by Whitfield<sup>7</sup> (for stationary grids), and Belk<sup>2</sup> (for dynamic grids) and therefore is only summarized here. This algorithm has been used by many people to obtain solutions for the Euler equations which compare well with experimental data for both steady and unsteady transonic flow problems. Lijewski<sup>8</sup> has shown excellent steady results for a complex canard-body-tail configuration at transonic Mach numbers and moderate range of incidence angles, while Belk<sup>9</sup> has shown unsteady results for oscillating airfoils and wings. However, Gatlin<sup>6</sup>

and van Leer<sup>10</sup> have shown that in some cases the FVS scheme is too dissipative to give good numerical results for viscous calculations, especially in high gradient regions such as boundary layers. Also presented in Section III is a discussion of the FDS scheme based on Roe's method of evaluating the numerical fluxes for the three-dimensional Euler equations. Recent works by van Leer<sup>10</sup> and Chakravarthy (References 11,12,13,14) and many others have discussed implementations of this FDS scheme. However, Whitfield, et al.<sup>3</sup> and Janus<sup>15</sup> have described a hybrid Roe algorithm which has been used to obtain excellent inviscid results for complex flow fields<sup>16</sup>.

Section IV discusses the extension of the inviscid algorithms discussed in Section III to the thin-layer Navier-Stokes (TLNS) equations. The viscous terms are added to the explicit side of the solution equation and are therefore treated as source terms to the inviscid equations. This treatment of the viscous terms reduces the cost of normal viscous calculations substantially by saving the cost associated with computing and storing the viscous flux jacobians. Additionally, work was performed to allow for more efficient calculations of unsteady viscous flows using the time lagged viscous terms. One of the major problems with unsteady TLNS calculations is the severe time step size limitations which must be imposed to maintain a reasonable Courant-Friedrichs-Lewy (CFL) number. Efforts to execute the unsteady TLNS code for oscillating airfoils and wings using very large CFL numbers are discussed. In order to maintain stability at these large CFL numbers a form of subiterations similar to those described in Reference 17 has been implemented. The result of subiterations is to converge the solution at a given time step before proceeding to the next step, thus

eliminating linearization and factorization errors and increasing the stability.

Section V describes the steady results obtained for transonic Mach numbers and moderate range of incidence angles for a laminar flat plate, RAE 2822 airfoil and the ONERA M6 wing. All the results presented in this chapter show a comparison between the FVS and FDS algorithms for viscous solutions and are compared with experimental data where available.

Section VI discusses the unsteady results for both oscillating airfoils and wings in transonic flow and moderate range of angles of attack. The oscillating airfoil case (NACA 0012) is compared for various time steps sizes and number of subiterations while the oscillating wing (Langley Rectangular Planform Supercritical Wing) results are compared with the inviscid results of Belk<sup>2</sup> and experimental data.

Conclusions are given in Section VII.

## SECTION II

### NAVIER-STOKES EQUATIONS

#### 2.1 Vector Form of the Navier-Stokes Equations

The compressible, three-dimensional Navier-Stokes equations in Cartesian coordinates, written in strong conservation form (without body forces or external heat addition) are

$$\frac{\partial \hat{q}}{\partial \hat{t}} + \frac{\partial \hat{f}}{\partial \hat{x}} + \frac{\partial \hat{g}}{\partial \hat{y}} + \frac{\partial \hat{h}}{\partial \hat{z}} = 0 \quad (2.1)$$

where  $\hat{q}, \hat{f}, \hat{g}$ , and  $\hat{h}$  are dimensional quantities given by

$$\hat{q} = \begin{bmatrix} \hat{\rho} \\ \hat{\rho}\hat{u} \\ \hat{\rho}\hat{v} \\ \hat{\rho}\hat{w} \\ \hat{e} \end{bmatrix}$$

$$\hat{f} = \begin{bmatrix} \hat{\rho}\hat{u} \\ \hat{\rho}\hat{u}^2 + \hat{p} - \tilde{\tau}_{xx} \\ \hat{\rho}\hat{u}\hat{v} - \tilde{\tau}_{xy} \\ \hat{\rho}\hat{u}\hat{w} - \tilde{\tau}_{xz} \\ (\hat{e} + \hat{p})\hat{u} - \hat{u}\tilde{\tau}_{xx} - \hat{v}\tilde{\tau}_{xy} - \hat{w}\tilde{\tau}_{xz} + \hat{q}_x \end{bmatrix}$$



$$\hat{g} = \begin{bmatrix} \hat{\rho}\hat{v} \\ \hat{\rho}\hat{u}\hat{v} - \tilde{\tau}_{yx} \\ \hat{\rho}\hat{v}^2 + \hat{p} - \tilde{\tau}_{yy} \\ \hat{\rho}\hat{v}\hat{w} - \tilde{\tau}_{yz} \\ (\hat{e} + \hat{p})\hat{v} - \hat{u}\tilde{\tau}_{yx} - \hat{v}\tilde{\tau}_{yy} - \hat{w}\tilde{\tau}_{yz} + \hat{q}_y \end{bmatrix}$$

$$\hat{h} = \begin{bmatrix} \hat{\rho}\hat{w} \\ \hat{\rho}\hat{u}\hat{w} - \tilde{\tau}_{zx} \\ \hat{\rho}\hat{v}\hat{w} - \tilde{\tau}_{zy} \\ \hat{\rho}\hat{w}^2 + \hat{p} - \tilde{\tau}_{zz} \\ (\hat{e} + \hat{p})\hat{w} - \hat{u}\tilde{\tau}_{zx} - \hat{v}\tilde{\tau}_{zy} - \hat{w}\tilde{\tau}_{zz} + \hat{q}_z \end{bmatrix}$$

$$\text{and } \hat{e} = \frac{\hat{p}}{\gamma - 1} + \frac{1}{2}\hat{\rho}(\hat{u}^2 + \hat{v}^2 + \hat{w}^2)$$

The first row in Equation (2.1) corresponds to the continuity equation, the next three rows are referred to as the momentum equations and the last row is the energy equation. In the strictest sense only the momentum equations are the Navier-Stokes equations; however, it is common practice to refer to the entire set of five equations as the Navier-Stokes equations.

The density of the fluid is  $\hat{\rho}$ , the pressure is  $\hat{p}$ , and the velocity components in the Cartesian coordinate directions  $\hat{x}, \hat{y}$ , and  $\hat{z}$  are  $\hat{u}, \hat{v}$ ,

and  $\hat{w}$  respectively. The relationship between  $\hat{e}$  and  $\hat{p}$  is the result of the perfect gas assumption and  $\gamma$  is the ratio of specific heats,

$$\gamma = \frac{C_p}{C_v} \quad (2.2)$$

The components of the viscous stress tensor are given as  $\hat{T}_{ij}$ .

If the fluid is assumed to behave as a "Newtonian fluid", that is, the stress is linearly dependent on the rates of strain of the fluid and the coefficient of bulk viscosity is negligible so that the relationship between  $\hat{\mu}$  (coefficient of viscosity) and  $\hat{\lambda}$  (second coefficient of viscosity) is

$$\hat{\lambda} = -\frac{2}{3}\hat{\mu} \quad (2.3)$$

then the viscous stress tensor in Cartesian coordinates is given as,

$$\begin{aligned} \hat{T}_{xx} &= \frac{2}{3} \hat{\mu} (2\hat{u}_x - \hat{v}_y - \hat{w}_z) \\ \hat{T}_{yy} &= \frac{2}{3} \hat{\mu} (2\hat{v}_y - \hat{u}_x - \hat{w}_z) \\ \hat{T}_{zz} &= \frac{2}{3} \hat{\mu} (2\hat{w}_z - \hat{u}_x - \hat{v}_y) \\ \hat{T}_{xy} &= \hat{T}_{yx} = \hat{\mu} (\hat{u}_y + \hat{v}_x) \\ \hat{T}_{xz} &= \hat{T}_{zx} = \hat{\mu} (\hat{w}_x + \hat{u}_z) \\ \hat{T}_{yz} &= \hat{T}_{zy} = \hat{\mu} (\hat{v}_z + \hat{w}_y) \end{aligned} \quad (2.4)$$

and the heat-flux vector in the Cartesian coordinate directions is given as

$$\begin{aligned} \hat{q}_x &= -\frac{C_p \hat{\mu}}{Pr} \hat{T}_x \\ \hat{q}_y &= -\frac{C_p \hat{\mu}}{Pr} \hat{T}_y \end{aligned} \quad (2.5)$$

$$\hat{q}_z = - \frac{C_F \hat{\mu}}{P_r} \hat{T}_z$$

where  $P_r$  is the Prandtl number.

It should be noted that the subscripts on the velocity components  $\hat{u}, \hat{v}, \hat{w}$  and on the temperature  $\hat{T}$  denote partial differentiation, while those on the stress and heat flux terms denote Cartesian coordinate directions.

The dimensional quantities (denoted by  $\wedge$ ) are nondimensionalized using freestream conditions (denoted by  $\infty$ ),  $\hat{L}$  (the reference length used in the Reynolds number) and,

$$\begin{aligned} x &= \frac{\hat{x}}{\hat{L}} & y &= \frac{\hat{y}}{\hat{L}} & z &= \frac{\hat{z}}{\hat{L}} & t &= \frac{\hat{t} \hat{a}_\infty}{\hat{L}} \\ u &= \frac{\hat{u}}{\hat{a}_\infty} & v &= \frac{\hat{v}}{\hat{a}_\infty} & w &= \frac{\hat{w}}{\hat{a}_\infty} & a &= \frac{\hat{a}}{\hat{a}_\infty} \\ \mu &= \frac{\hat{\mu}}{\hat{\mu}_\infty} & \rho &= \frac{\hat{\rho}}{\hat{\rho}_\infty} & p &= \frac{\hat{p}}{\hat{\rho}_\infty \hat{a}_\infty^2} & T &= \frac{\hat{T}}{\hat{T}_\infty} \end{aligned} \quad (2.6)$$

where  $\hat{a}_\infty = \sqrt{\hat{\gamma} \hat{R} \hat{T}_\infty}$

is the freestream speed of sound.

This nondimensionalization results in a set equations of exactly the same form as Equation (2.1) but without the  $\wedge$ .

$$\frac{\partial q}{\partial t} + \frac{\partial f}{\partial x} + \frac{\partial g}{\partial y} + \frac{\partial h}{\partial z} = 0 \quad (2.7)$$

## 2.2 Curvilinear Coordinate Transformation

Equation (2.7) can be transformed into a curvilinear coordinate system which allows the use of body-conforming grids in order to simplify the implementation of boundary conditions. The curvilinear coordinates used in this transformation are

$$\begin{aligned}\xi &= \xi(x,y,z,t) \\ \eta &= \eta(x,y,z,t) \\ \zeta &= \zeta(x,y,z,t) \\ \tau &= \tau(t)\end{aligned}\tag{2.8}$$

Note the use of time,  $t$ , to define the curvilinear coordinates. This will allow for the time dependent motion of a body. The details of a time dependent transformation to curvilinear coordinates are given for the Navier-Stokes equations in Appendix A.

## 2.3 Thin-Layer Navier-Stokes Equations

A numerical solution of the Navier-Stokes equations can require large amounts of computer time and memory. One assumption often made to reduce the cost of a solution is to neglect all viscous terms which contain derivatives in the direction parallel to the body. The original development of this idea is presented in Reference 18. This assumption is justified since these terms are substantially smaller than the terms with derivatives normal to the body. Also, it would be impractical to think a grid could be refined enough in the direction parallel to the body to resolve the diffusive terms in this direction. The solution of the TLNS set of equations has an advantage over the boundary-layer

equations, which assume also that the normal pressure gradient is negligible. Therefore, the thin layer Navier-Stokes equations (TLNS) are capable of handling flow separation and reverse flow regions with no special considerations necessary.

After the curvilinear coordinate transformation, the Navier-Stokes equations have the form

$$\frac{\partial Q}{\partial \tau} + \frac{\partial F}{\partial \xi} + \frac{\partial G}{\partial \eta} + \frac{\partial H}{\partial \zeta} = 0 \quad (2.9)$$

where the vectors  $Q, F, G$ , and  $H$  are defined in Appendix A, Equation (A.9). If the thin layer assumption is made for the solid surface to exist on a constant  $\eta$  grid line, as is normal for a "C type" numerical grid, then viscous terms inside the  $F$  and  $H$  flux vectors are neglected along with all the terms in flux vector  $G$  which contain derivatives with respect to either  $\xi$  or  $\zeta$ . This results in the thin layer Navier-Stokes equations as follows

$$\frac{\partial Q}{\partial \tau} + \frac{\partial F}{\partial \xi} + \frac{\partial G}{\partial \eta} + \frac{\partial H}{\partial \zeta} = 0 \quad (2.9)$$

where,

$$Q = J' T_1 \begin{bmatrix} \rho \\ \rho u \\ \rho v \\ \rho w \\ e \end{bmatrix}$$

$$\begin{aligned}
F &= J' \begin{bmatrix} \rho U \\ \rho uU + \xi_x p \\ \rho vU + \xi_y p \\ \rho wU + \xi_z p \\ (e+p)U - \xi_t p \end{bmatrix} \\
G &= J' \begin{bmatrix} \rho V \\ \rho uV + \eta_x p - \tilde{T}_{\eta x} \\ \rho vV + \eta_y p - \tilde{T}_{\eta y} \\ \rho wV + \eta_z p - \tilde{T}_{\eta z} \\ (e+p)V - \eta_t p - u\tilde{T}_{\eta x} - v\tilde{T}_{\eta y} - w\tilde{T}_{\eta z} + \Gamma_\eta \end{bmatrix} \\
H &= J' \begin{bmatrix} \rho W \\ \rho uW + \zeta_x p \\ \rho vW + \zeta_y p \\ \rho wW + \zeta_z p \\ (e+p)W - \zeta_t p \end{bmatrix}
\end{aligned} \tag{2.10}$$

and

$$U = \xi_t + \xi_x u + \xi_y v + \xi_z w$$

$$V = \eta_t + \eta_x u + \eta_y v + \eta_z w$$

$$W = \zeta_t + \zeta_x u + \zeta_y v + \zeta_z w$$

$$\tilde{T}_{\eta x} = \eta_x \tau_{xx} + \eta_y \tau_{yx} + \eta_z \tau_{xz}$$

$$\tilde{T}_{\eta y} = \eta_x \tau_{xy} + \eta_y \tau_{yy} + \eta_z \tau_{yz}$$

$$\tilde{T}_{\eta z} = \eta_x \tau_{xz} + \eta_y \tau_{yz} + \eta_z \tau_{zz}$$

(2.11)

$$\Gamma_\eta = \eta_x q_x + \eta_y q_y + \eta_z q_z$$

Applying the thin layer assumption, the viscous stress tensors described in Equation (A.10), become

$$\tau_{xx} = \frac{2\mu M_\infty}{3Re_l} [2\eta_x u_\eta - \eta_y v_\eta - \eta_z w_\eta]$$

$$\tau_{yy} = \frac{2\mu M_\infty}{3Re_l} [2\eta_y v_\eta - \eta_x u_\eta - \eta_z w_\eta]$$

$$\tau_{zz} = \frac{2\mu M_\infty}{3Re_l} [2\eta_z w_\eta - \eta_x u_\eta - \eta_y v_\eta]$$

$$\tau_{xy} = \frac{\mu M_\infty}{Re_l} [\eta_y u_\eta + \eta_x v_\eta]$$

$$\tau_{xz} = \frac{\mu M_\infty}{Re_l} [\eta_z u_\eta + \eta_x w_\eta]$$

$$\tau_{yz} = \frac{\mu M_\infty}{Re_l} [\eta_z v_\eta + \eta_y w_\eta]$$

and the heat flux terms become

$$q_x = \frac{1}{\gamma-1} \frac{\mu M_\infty}{Pr Re_l} \eta_x T_\eta$$

$$q_y = \frac{1}{\gamma-1} \frac{\mu M_\infty}{Pr Re_l} \eta_y T_\eta$$

$$q_z = \frac{1}{\gamma-1} \frac{\mu M_\infty}{Pr Re_l} \eta_z T_\eta$$

### SECTION III DESCRIPTION OF SPLITTING TECHNIQUES

#### 3.1 Basic Implicit Algorithm

A comparison of the FVS and FDS numerical schemes referenced in Section I can be easily understood by considering the one-dimensional Euler equations

$$\frac{\partial Q}{\partial t} + \frac{\partial F}{\partial \xi} = 0 \quad (3.1)$$

An implicit, finite volume discretization of Equation (3.1) may be written as

$$\frac{\Delta Q^n}{\Delta \tau} + \frac{\delta_\xi F^{n+1}}{\Delta \xi} = 0 \quad (3.2)$$

where,

$$\Delta Q^n = Q^{n+1} - Q^n$$

and

$$\delta_\xi F^{n+1} = \frac{(F_{i+1/2} - F_{i-1/2})^{n+1}}{\Delta \xi}$$

Since in the curvilinear coordinate transformation the term  $\Delta \xi$  can be set equal to one, it may be dropped from the equation. Equation (3.2), when solved for  $\Delta Q^n$ , becomes

$$\Delta Q^n = -\Delta \tau \delta_\xi F^{n+1} \quad (3.3)$$

Since the flux  $F$  is a non-linear function of the dependent variables  $(\rho, \rho u, \rho v, \rho w, e)$  then, using a linearization first described by



Briley and McDonald<sup>19</sup> and Beam and Warming<sup>20</sup> where,

$$F^{n+1} = F^n + A^n \Delta Q^n + O(\Delta t^2) \quad (3.4)$$

the first order accurate scheme,  $O(\Delta t)$ , based on the backward Euler differencing formula, Equation (3.3) is

$$(I + \Delta T \delta_\xi A^n) \Delta Q^n = -\Delta T \delta_\xi F^n \quad (3.5a)$$

while a second order accurate scheme,  $O(\Delta t^2)$ , based on the three point backward differencing formula of Equation (3.3), is

$$(I + \frac{2}{3} \Delta T \delta_\xi A^n) \Delta Q^n = -\frac{2}{3} \Delta T \delta_\xi F^n + \frac{1}{3} \Delta Q^{n-1} \quad (3.5b)$$

Note that the dot( ) indicates the  $\delta$  operator acts on the entire term  $\delta_\xi (A^n \Delta Q^n)$ , etc., and the term  $A^n$ , is defined as the jacobian of the flux vector

$$A \equiv \frac{\partial F}{\partial Q}$$

### 3.2 Flux-Vector Splitting

The eigensystem of the flux jacobian matrix  $A$  is necessary to achieve the desired splitting. The flux jacobian matrix can be diagonalized as detailed in Reference 21. The resulting diagonal matrix  $\Lambda$  has the eigenvalues of  $A$  as its diagonal elements,

$$A = T \Lambda T^{-1} \quad (3.6)$$

where  $T$  is a matrix whose columns are the right eigenvectors of  $A$ , and

$T^{-1}$ 's rows are the left eigenvectors.

The one-dimensional Euler equations have three real eigenvalues associated with the jacobian matrix  $A$ . The eigenvalues are the characteristic velocities of the system. The flux vector  $F$  can be written as the sum of two subvectors. The subvectors are written with a superscript (+) which indicates the portion of the flux vector resulting in nonnegative eigenvalues and superscript (-) which indicates the portion of the flux vector resulting in the nonpositive eigenvalues

$$F = F^+ + F^- \quad (3.7)$$

where

$$\Lambda^\pm = \frac{\Lambda \pm |\Lambda|}{2} \quad (3.8)$$

which allows the split flux jacobian matrix  $A^\pm$  to be defined

$$A^\pm = T \Lambda^\pm T^{-1} \quad (3.9)$$

Since the flux vector  $F$  is a homogeneous function of degree one in  $Q$  then

$$F^\pm = A^\pm Q \quad (3.10)$$

The splitting of the flux vector  $F$  described above is the flux vector splitting of Steger and Warming<sup>4</sup>.

An upwind first order spatially accurate scheme using the splitting described can be constructed as

$$F_{i+1/2} = F_i^+ + F_{i+1}^- \quad (3.11)$$

$$= \frac{1}{2} (F_i + F_{i+1}) - (|A|_{i+1} Q_{i+1} - |A|_i Q_i)$$

where

$$|A| = A^+ - A^-$$

van Leer<sup>10</sup> has pointed out that many numerical fluxes may be written in the form

$$F_{i+1/2} = \frac{1}{2}(F_i + F_{i+1}) - \frac{1}{2} D(Q_i, Q_{i+1}) \cdot (Q_{i+1} - Q_i) \quad (3.12)$$

and the freedom of choosing a numerical flux formula essentially lies in the choice of the matrix coefficient,  $D(Q_i, Q_{i+1})$  of the dissipation term.

The dissipation matrix corresponding to the Steger-Warming splitting has been shown to contain too much numerical dissipation. The result of this additional dissipation is a smearing of shocks and contact discontinuities.

### 3.3 Flux Difference Splitting

The flux vector split scheme described above has been described by Barth<sup>22</sup> as being a "point-by-point splitting" or in other words a flux vector at a given point is split without concern of the state of its neighboring points. In contrast to this idea, the flux difference split scheme referred to in Section I is based on the "interaction" of neighboring points through an approximate solution to the Riemann initial-value problem. The FDS scheme used in this work was based on Roe's approximate Riemann solver which uses an intermediate state of the

dependent variables  $\bar{Q}$  to determine the matrix coefficient  $\bar{A}(\bar{Q})$  of the dissipation term described in Equation (3.12). The numerical flux formula for the Roe type scheme is

$$F_{i+1/2} = \frac{1}{2}(F_i + F_{i+1}) - |\bar{A}|_{i+1/2}(Q_{i+1} - Q_i) \quad (3.13)$$

Roe<sup>5</sup> required the matrix  $\bar{A}(Q_i, Q_{i+1})$  to have the following list of properties, which he calls Property U since it ensures uniform validity across discontinuities:

- (i) It constitutes a linear mapping from the vector space  $Q$  to the vector space  $F$ .
- (ii) As  $Q_i \rightarrow Q_{i+1} \rightarrow Q$ , Then  $\bar{A}(Q_i, Q_{i+1}) \rightarrow A(Q)$ , where  $A = \frac{\partial F}{\partial Q}$
- (iii) For any  $Q_i, Q_{i+1}$ ,  $\bar{A}(Q_i, Q_{i+1}) \cdot (Q_{i+1} - Q_i) = F_{i+1} - F_i$
- (iv) The eigenvectors of  $\bar{A}$  are linearly independent.

Property (ii) ensures that the approximate solution approaches the exact solution as the mesh size is decreased. Reference 10 points out that Property (iii) results in the fact that if the eigenvalue of  $\bar{A}(Q_i, Q_{i+1})$  vanishes then the corresponding eigenvalues of the dissipation matrix  $|\bar{A}|$  vanish, since the eigenvalues of  $|\bar{A}|$  are the absolute value of the eigenvalues of  $\bar{A}$ . Since the numerical dissipation vanishes, this results in nice sharp modeling of shocks or contact discontinuities as opposed to the Steger-Warming FVS scheme in which the eigenvalues of the dissipation matrix of  $|A|$  become discontinuous whenever the corresponding eigenvalues of  $A$  vanish.

Let  $\lambda^j$ ,  $j=1,2,\dots,m$  be the eigenvalues of the Roe matrix  $\bar{A}$  and

$r^j$  be the right eigenvectors and  $l^j$  be the left eigenvectors such that  $l^j$  and  $r^j$  are orthonormal then

$$|\bar{A} - \lambda^j I| = 0 \quad (3.14)$$

and

$$(\bar{A} - \lambda^j I)r^j = 0 \quad (3.15a)$$

$$l^j(\bar{A} - \lambda^j I) = 0 \quad (3.15b)$$

Jeffery<sup>23</sup> (see Chapter 2) has shown that the change across each characteristic curve associated with a specific  $\lambda^j$  is proportional to the right eigenvector  $r^j$  associated with that eigenvalue of the Roe matrix  $\bar{A}$

$$Q_{i+1} - Q_i = \sum_{j=1}^m \alpha_j r^j \quad (3.16)$$

Jeffery has also shown that

$$\bar{A} dQ^j = \lambda^j dQ^j \quad (3.17)$$

Therefore, extension to the one-dimensional Euler equations results in

$$F_{i+1} - F_i = \bar{A}(Q_i, Q_{i+1}) \cdot (Q_{i+1} - Q_i) \quad (3.18a)$$

$$= \sum_{j=1}^m \alpha_j \lambda^j r^j \quad (3.18b)$$

$$= \sum_{j=1}^m df^j \quad (3.18c)$$

where  $df^j$  is the change in a flux vector across each characteristic curve associated with the eigenvalue  $\lambda^j$ .

A numerical formula for the flux vector at a cell interface  $i+1/2$  for

the one-dimensional Euler equation might be

$$F_{i+1/2} = F_i + \sum_{j=1}^m \alpha_j \lambda^{-j} r^j \quad (3.19)$$

where the  $(-)$  superscript on  $\lambda$ , indicates that only characteristic curves associated with negative eigenvalues (i.e., nonpositive slope in Figure 3.1) are used.

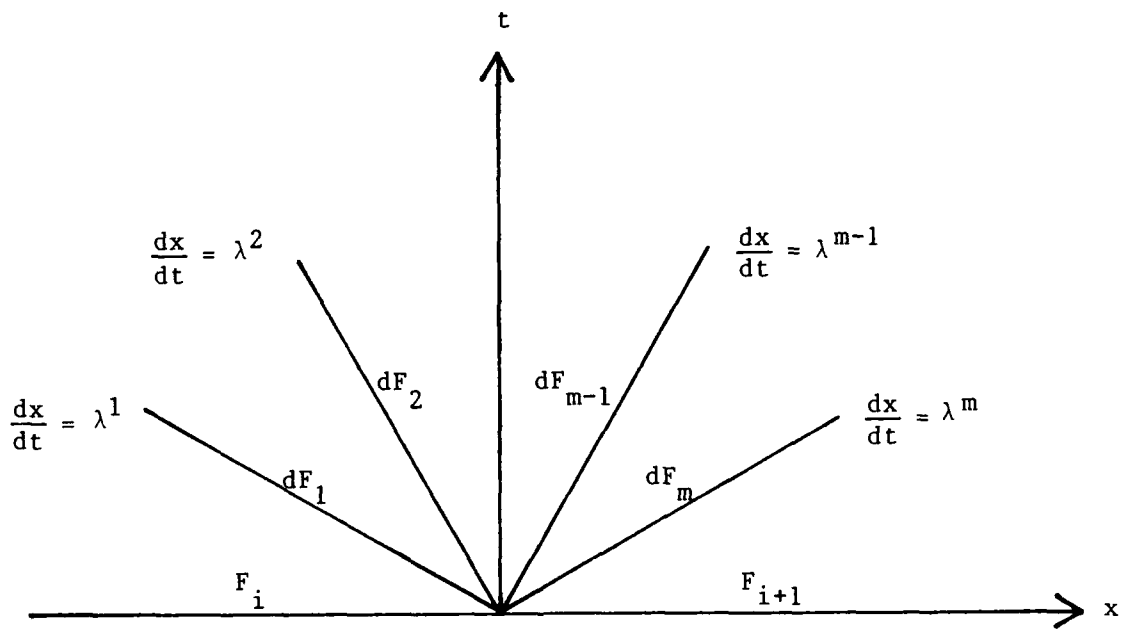


Figure 3.1 Characteristic Waves

Another flux formula is

$$F_{i+1/2} = F_{i+1} - \sum_{j=1}^m \alpha_j \lambda^{+j} r^j \quad (3.20)$$

where the  $(+)$  superscript on  $\lambda$  indicates that only positive

eigenvalues are used. Finally, a third flux formula is obtained by averaging Equations (3.19) and (3.20)

$$F_{i+1/2} = \frac{1}{2}(F_i + F_{i+1}) - \frac{1}{2} \sum_{j=1}^m \alpha_j |\lambda^j| r^j \quad (3.21)$$

The flux formula given in Equation (3.21) can be interpreted to be in the form described by Equation (3.12) by letting

$$\Phi = |\bar{A}| (Q_{i+1} - Q_i) \quad (3.22)$$

and from Equation (3.16)

$$\Phi = \sum_{j=1}^m |\bar{A}| \alpha_j r^j \quad (3.23)$$

The Roe matrix  $\bar{A}$  is diagonalizable just as the flux jacobian matrix  $A$  for the FVS scheme is in Equation (3.6), so that

$$|\bar{A}| = T(\Lambda^+ - \Lambda^-)T^{-1} \quad (3.24)$$

and

$$\Phi = \sum_{j=1}^m T(\Lambda^+ - \Lambda^-)T^{-1} \alpha_j r^j \quad (3.25)$$

Equation (3.25) can be shown to reduce to the following (see Reference 3)

$$\Phi = \sum_{j=1}^m \alpha_j |\lambda^j| r^j \quad (3.26)$$

Therefore Equation (3.21) can be written as

$$F_{i+1/2} = \frac{1}{2}(F_i + F_{i+1}) - \frac{1}{2} |\bar{A}|_{i+1/2} (Q_{i+1} - Q_i) \quad (3.27)$$

The extension of both of these schemes (FVS and FDS) to higher order accuracy and full three-dimensional equations is considered next. The discussion will deal with the set of equations as though they were purely hyperbolic partial differential equations (i.e., 3-D Euler equations). This is possible by treating the diffusive flux terms explicitly and therefore placing them on the right hand side of Equation (2.9) as source terms. The details of this explicit treatment of the viscous flux terms are discussed in Section IV.

### 3.4 Flux-Vector Splitting for Three Dimensions

Since the viscous flux terms are to be treated explicitly the remaining terms form a set of hyperbolic partial differential equations characterized by a limited domain of dependence. The solution at a point is not dependent on every other point in the field and information travels only in certain characteristic directions. If a numerical scheme is selected to take advantage of this fact, then information for numerical differencing is taken only from the direction from which information is propagating (i.e., upwinding). The use of upwind differencing normally alleviates the necessity for adding numerical dissipation to smooth the results near discontinuities such as shocks. This becomes apparent when one considers the discussion in paragraph 3.1 concerning the nature of the dissipation matrix at or near discontinuities. The details of the upwind, finite volume, flux-vector split scheme for the three dimensional Euler equations have been reported many times (References 3,7,9,and 21), and thus only the highlights will be provided here.

The flux jacobian matrices A,B, and, C for the three-dimensional



unsteady Euler equations are

$$A \equiv \frac{\partial F}{\partial Q}$$

$$B \equiv \frac{\partial G}{\partial Q}$$

$$C \equiv \frac{\partial H}{\partial Q}$$

The eigenvalues of the flux jacobian matrices are the characteristic velocities in the three coordinate directions. The flux vectors F, G, and, H can be written as the sum of two subvectors as shown in Equation (3.7) for the one-dimensional equation. The subvectors are written with a superscript (+) which indicates the portion of the flux vector resulting in nonnegative eigenvalues and superscript (-) which indicates the portion of the flux vector resulting in the nonpositive eigenvalues

$$F = F^+ + F^-$$

$$G = G^+ + G^- \quad (3.28)$$

$$H = H^+ + H^-$$

Each of the split flux vectors are linearized the same as described in Equation (3.4)

$$F^{+n+1} = F^{+n} + A^+ \Delta Q^n + O(\Delta t^2) \quad (3.29a)$$

$$F^{-n+1} = F^{-n} + A^- \Delta Q^n + O(\Delta t^2) \quad (3.29b)$$

and similarly for  $G^{+n+1}$ ,  $G^{-n+1}$ ,  $H^{+n+1}$ , and  $H^{-n+1}$ .

The split flux jacobians are now defined as the true jacobians matrices obtained by differentiating the positive and negative flux vectors

instead of the splitting defined in Equation (3.9)

$$A^+ = \frac{\partial F^+}{\partial Q} \quad (3.30)$$

$$A^- = \frac{\partial F^-}{\partial Q}$$

and similarly for  $B^+, B^-, C^+$ , and  $C^-$ . The derivation of these split flux jacobian matrices are given in excruciating detail for dynamic grids in Reference 2.

When the split form for the fluxes given by Equation (3.29) is used, Equation (3.5), when expanded to three dimensions, becomes

$$[I + \Delta T (\delta_\xi A^+ + \delta_\xi A^- + \delta_\eta B^+ + \delta_\eta B^- + \delta_\zeta C^+ + \delta_\zeta C^-)] \Delta Q^n = -\Delta T R^n \quad (3.31a)$$

and

$$R^n = (\delta_\xi F^+ + \delta_\xi F^- + \delta_\eta G^+ + \delta_\eta G^- + \delta_\zeta H^+ + \delta_\zeta H^-) \quad (3.31b)$$

The flux vector splitting results in a seemingly simple expression but one which proves impractical to solve for most problems of any practical size due to the wide bandwidth of the matrix system. Many different factorizations have been used for this system by Whitfield<sup>7</sup>. The factorization used in this work was the two factor scheme, in which all terms corresponding to nonnegative eigenvalues (+) are lumped together and all terms corresponding to nonpositive eigenvalues (-) are lumped together.

$$\begin{aligned} & [I + \Delta T (\delta_\xi A^+ + \delta_\eta B^+ + \delta_\zeta C^+)] \\ & [I + \Delta T (\delta_\xi A^- + \delta_\eta B^- + \delta_\zeta C^-)] \Delta Q^n = -\Delta T R^n \end{aligned} \quad (3.32)$$

The factorization error created is no larger than the linearization error already inherent in the scheme,  $O(\Delta t^2)$ .

The solution to Equation (3.32) is carried out as follows

$$[I + \Delta T(\delta_{\xi} A^{+} + \delta_{\eta} B^{+} + \delta_{\zeta} C^{+})] X^1 = -\Delta T R^n \quad (3.33a)$$

$$[I + \Delta T(\delta_{\xi} A^{-} + \delta_{\eta} B^{-} + \delta_{\zeta} C^{-})] X^2 = X^1 \quad (3.33b)$$

$$\Delta Q^n = X^2 \quad (3.33c)$$

The solution of Equation (3.33) results in two passes through the computational field. The first pass, Equation (3.33a), solves a sparse block lower triangular system and the second pass, Equation (3.33b), solves a sparse block upper triangular system. This results in a very efficient numerical scheme since only forward and backward substitution are required and not a matrix inversion.

Now only a description of the central difference operators in Equation (3.33) is needed to complete the description of the flux vector split scheme. Since the scheme is finite volume, dependent variables are known at cell centers; however, the central difference operators represent flux differences at cell faces. The value of the dependent variables at cell faces are determined by an extrapolation. For a positive extrapolation a value at the cell face labeled  $(i+1/2, j, k)$  is determined from

$$Q_{i+1/2}^{+} = \frac{3}{2}Q_i - \frac{1}{2}Q_{i-1} + O(\Delta \xi^2) \quad (3.34a)$$

or

$$Q_{i+1/2}^{+} = Q_i + O(\Delta \xi) \quad (3.34b)$$

and for a negative extrapolation

$$Q_{i+1/2}^- = \frac{3}{2}Q_{i+1} - \frac{1}{2}Q_{i+2} + O(\Delta\xi^2) \quad (3.35a)$$

or

$$Q_{i+1/2}^- = Q_{i+1} + O(\Delta\xi) \quad (3.35b)$$

The first order extrapolations are used for the difference operators on the left-hand (implicit) side of Equation (3.33) where only first order spatial accuracy is necessary since for steady results  $\Delta Q^n \rightarrow 0$ . The second order extrapolations are used on the right-hand (explicit) side of Equation (3.33) to give a second order spatial accurate scheme.

In order to evaluate the split flux difference terms in the residual vector, Equation (3.31b), using  $F^+$  and  $F^-$  as examples, a set of positive eigenvalues,  $\lambda_1(Q^+)$ , and positive split fluxes,  $F_1(Q^+)$ , are found using the dependent variables described in Equation (3.34), where  $F_1(Q)$  is the component of the flux,  $F$ , associated with the eigenvalue  $\lambda_1$ .

Similarly, using Equation (3.35) a set of negative eigenvalues,  $\lambda_1(Q^-)$ , and negative split fluxes,  $F_1(Q^-)$ , are determined.

The total flux through a cell face  $(i+1/2, j, k)$  is determined using

$$F_{i+1/2} = F^+ + F^-$$

$$F^+ = \frac{1}{2} \sum_{i=1}^5 [\lambda_1(Q^+) + |\lambda_1(Q^+)|] F_1(Q^+) \quad (3.36a)$$

and

$$F^- = \frac{1}{2} \sum_{i=1}^5 [\lambda_1(Q^-) - |\lambda_1(Q^-)|] F_1(Q^-) \quad (3.36b)$$

The numerical scheme described here has been labeled BMULE (Brown's Mule) by Whitfield<sup>7</sup>.

### 3.5 Flux Difference Splitting for Three Dimensions

The FDS scheme used here has been described in detail by Whitfield<sup>3</sup> for application to the three-dimensional Euler equations. The FDS scheme of Roe is based on an approximate Riemann solver which solves the linear Riemann problem (shown in one-dimension, where  $\bar{A}$  is the jacobian matrix).

$$\frac{\partial Q}{\partial t} + \bar{A}(Q_i, Q_{i+1}) \frac{\partial Q}{\partial x} = 0 \quad (3.37)$$

The flux formulas discussed in paragraph 3.3 can easily be extended to three-dimensions by splitting the wave into the three curvilinear coordinate directions since the eigenvalues are dependent on the contravariant velocities normal to a cell face. The wave motions are split based on these eigenvalues resulting in a set of equations in which the wave motion is normal to the cell interface just as though they were a set of one-dimensional equations.

The jacobian matrix  $\bar{A}(Q_i, Q_{i+1})$  is evaluated using a set of special averaged values. The "Roe averaged" variables for the three-dimensional Euler equations are

$$\begin{aligned} \rho &= \sqrt{\rho_i \rho_{i+1}} \\ u &= \frac{\sqrt{\rho_i} u_i + \sqrt{\rho_{i+1}} u_{i+1}}{\sqrt{\rho_i} + \sqrt{\rho_{i+1}}} \\ v &= \frac{\sqrt{\rho_i} v_i + \sqrt{\rho_{i+1}} v_{i+1}}{\sqrt{\rho_i} + \sqrt{\rho_{i+1}}} \\ w &= \frac{\sqrt{\rho_i} w_i + \sqrt{\rho_{i+1}} w_{i+1}}{\sqrt{\rho_i} + \sqrt{\rho_{i+1}}} \end{aligned} \quad (3.38)$$

and

$$a^2 = \frac{\gamma p}{\rho} = (\gamma - 1) h - \frac{1}{2}(u^2 + v^2 + w^2) \quad (3.39a)$$

$$e = \frac{p}{\gamma - 1} + \frac{1}{2}\rho(u^2 + v^2 + w^2) \quad (3.39b)$$

where  $h$  is the total enthalpy. Roe and Pike<sup>24</sup> have shown that these averaged variables are the only ones having the required properties to satisfy the Property U requirements. The details of the derivation of the "Roe averaged" variables are given in Reference 5.

An implicit algorithm using the flux difference described in Equations (3.19) and (3.20) is obtained by linearization of the first order flux. The metrics, denoted by  $M$ , are included in the expansion of the flux vector and the jacobian matrix in order to note the spatial location that the metrics are to be evaluated. Also, noted as a superscript is the time step to which the metrics correspond, this becomes important for calculations using dynamic grids. Equations (3.19) and (3.20) are written in the following form using the same development as described in Reference 3, where

$$\bar{F}_{i+1/2}^{n+1} = F_i^{n+1} + \bar{A}_{i+1/2}^{-} (Q_{i+1}^{n+1} - Q_i^{n+1}) \quad (3.40a)$$

and

$$\bar{F}_{i-1/2}^{n+1} = F_i^{n+1} + \bar{A}_{i-1/2}^{-} (Q_i^{n+1} - Q_{i-1}^{n+1}) \quad (3.40b)$$

A formal linearization of Roe's numerical flux (Equation (3.40)) is extremely complicated as recognized by Barth<sup>22</sup>. An assumption often made to simplify the linearization is to neglect the spatial derivatives of the Roe matrix  $\bar{A}^{-}$ . If this assumption is made then the

linearized flux difference at cell i is

$$\begin{aligned} \bar{F}_{i+1/2}^{n+1} - \bar{F}_{i-1/2}^{n+1} &= \bar{F}_{i+1/2}^n - \bar{F}_{i-1/2}^n + \bar{A}_{i+1/2}^- \Delta Q_{i+1}^n - \bar{A}_{i-1/2}^+ \Delta Q_{i-1}^n + \\ &[A(Q_i^n, M_{i+1/2}^{n+1}) - \bar{A}_{i+1/2}^- - A(Q_i^n, M_{i-1/2}^{n+1}) + \bar{A}_{i-1/2}^+] \Delta Q_i^n \end{aligned} \quad (3.41)$$

If the locations of the metrics in the jacobian metrics A are neglected then Equation (3.41) results in

$$\begin{aligned} \bar{F}_{i+1/2}^{n+1} - \bar{F}_{i-1/2}^{n+1} &= \bar{F}_{i+1/2}^n - \bar{F}_{i-1/2}^n + \bar{A}_{i+1/2}^- \Delta Q_{i+1}^n - \bar{A}_{i-1/2}^+ \Delta Q_{i-1}^n + \\ &[-\bar{A}_{i+1/2}^- + \bar{A}_{i-1/2}^+] \Delta Q_i^n \end{aligned} \quad (3.42)$$

or if

$$\delta(A\Delta Q)_i = A_{i+1/2} \Delta Q_{i+1}^n - A_{i-1/2} \Delta Q_{i-1}^n \quad (3.43)$$

then

$$\bar{F}_{i+1/2}^{n+1} - \bar{F}_{i-1/2}^{n+1} = \bar{F}_{i+1/2}^n - \bar{F}_{i-1/2}^n + \delta \bar{A}^- \Delta Q^n + \delta \bar{A}^+ \Delta Q^n \quad (3.44)$$

The remaining two flux terms, G and H, follow in a similar manner. Therefore, Equation (3.5), when expanded to the three-dimensional Euler equations for the FDS scheme, results in

$$[I + \Delta \tau (\delta_\xi \bar{A}^+ + \delta_\xi \bar{A}^- + \delta_\eta \bar{B}^+ + \delta_\eta \bar{B}^- + \delta_\zeta \bar{C}^+ + \delta_\zeta \bar{C}^-)] \Delta Q^n = -\Delta \tau R^n \quad (3.45a)$$

and

$$R^n = (\delta_\xi \bar{F}^+ + \delta_\xi \bar{F}^- + \delta_\eta \bar{G}^+ + \delta_\eta \bar{G}^- + \delta_\zeta \bar{H}^+ + \delta_\zeta \bar{H}^-) \quad (3.45b)$$

Note that Equation (3.45) has the same form as Equation (3.31) from the flux vector split form of Equation (3.5), however, the flux jacobian matrices in Equation (3.45) are the Roe matrices, and the jacobian matrices in Equation (3.31) are the true partials of the positive and

negative flux vectors. Solutions to Equations (3.31) have been obtained but as noted in Reference 3, in all cases tested improved results and convergence rates were obtained from solving Equation (3.31a) but using the residuals from Equation (3.45b)

$$[I + \Delta T (\delta_{\xi} A^+ + \delta_{\xi} A^- + \delta_{\eta} B^+ + \delta_{\eta} B^- + \delta_{\zeta} C^+ + \delta_{\zeta} C^-)] \Delta Q^n = -\Delta T R^n \quad (3.46a)$$

and

$$R^n = (\delta_{\xi} \bar{F}^+ + \delta_{\xi} \bar{F}^- + \delta_{\eta} \bar{G}^+ + \delta_{\eta} \bar{G}^- + \delta_{\zeta} \bar{H}^+ + \delta_{\zeta} \bar{H}^-) \quad (3.46b)$$

Therefore, the implicit solution from the FVS scheme is used with the residuals for the FDS scheme.

The reason for the improved results using the implicit portion of the FVS scheme, Equation (3.31a), instead of the implicit portion of the FDS scheme, Equation (3.45a), is due to the fact that approximated flux jacobians are used for the FDS scheme while, the FVS scheme uses the true partials of the flux split jacobians. Any approximations for these flux jacobian terms have nearly always degraded the convergence rates of the solution.

The numerical fluxes discussed in paragraph 3.3 are only first order accurate in space. Higher order methods used here (second and third order) are due to Osher and Chakravarthy<sup>25</sup>. The implementation of the higher order methods is described by Whitfield<sup>3</sup> (refer to Equation (54)).

Using Equation (3.19) for the first order flux, a second or third order scheme for the flux at cell interface  $i+1/2$  may be obtained by



adding a correction term. If all "Roe variables" and metric terms used in computing the eigenvalues and eigenvectors are evaluated at the cell face  $i+1/2$ , then the higher order flux formula becomes

$$\begin{aligned} \bar{F}_{i+1/2} = & F(Q_i)_{i+1/2} + \sum_{j=1}^m \sigma_{j,i+1/2}^- r_{i+1/2}^j + \\ & \sum_{j=1}^m \left\{ \frac{1-\psi}{4} [L_j^+(-1,1) - L_j^-(3,1)] + \right. \\ & \left. - \frac{1+\psi}{4} [L_j^+(1,-1) - L_j^-(1,3)] \right\} r_{i+1/2}^j \end{aligned} \quad (3.47)$$

where

$$\sigma_{j,i+1/2}^\pm = \lambda_{i+1/2}^{\pm j} \alpha_{j,i+1/2} \quad (3.48)$$

and

$$\alpha_{j,i-1/2} = \frac{1}{2} (Q_i - Q_{i-1}) \quad (3.49a)$$

$$\alpha_{j,i+1/2} = \frac{1}{2} (Q_{i+1} - Q_i) \quad (3.49b)$$

$$\alpha_{j,i+3/2} = \frac{1}{2} (Q_{i+2} - Q_{i+1}) \quad (3.49c)$$

Two flux limiters were tested in this work; they are defined as the minmod and superbee limiters:

$$L_j^\pm(1,n) = \text{minmod} \left( \sigma_{j,i+1/2}^\pm, b \sigma_{j,i+n/2}^\pm \right) \quad (3.50a)$$

$$\text{minmod}(x,y) = \text{sign}(x) \max \{0, \min[|x|, y \text{ sign}(x)]\} \quad (3.50b)$$

$$b = \frac{3 - \psi}{1 - \psi} \quad (3.50c)$$

The minmod limiter, where  $b$  is the compression parameter, uses two arguments,  $x$  and  $y$ . When these arguments are of opposite sign the value returned is zero. When they have the same sign the value returned is the smaller absolute value. The minmod limiter uses as its two arguments the unlimited flux value at a cell interface and compares this value with the product of the compression parameter and the flux value at the

neighboring interface on either side. When these values have the same sign then the value returned is nearly always the unlimited flux value since the compression parameter used in these calculations was large (two for the second order scheme and four for the third order scheme). Points in the solution where these values might have different signs are the maxima or minima of fluxes (i.e., shocks or strong gradients). In these cases the unlimited fluxes can easily have different signs, in which case the minmod limiter returns a zero and the solution reverts to first order.

The superbee limiter used in conjunction with Equation (3.47) is simply

$$L_j^+(1,n) \approx L_j^+(n,1) \quad (3.51a)$$

$$L_j^+(1,n) = \text{cplim} \left( \sigma_{j,1+1/2}^+, \sigma_{j,1+n/2}^+ \right) \quad (3.51b)$$

$$\begin{aligned} \text{cplim}(x,y) = \text{sign}(x) \{ \max 0, \min[|x|, \beta y \text{sign}(x)] , \\ \min[\beta |x|, y \text{sign}(x)] \} \end{aligned} \quad (3.51c)$$

where  $\beta$  is the compression parameter, which was set to 2 for all results shown here.

The second order truncation error is presented for several combinations of  $\psi$  and  $b$  in Table I from Reference 13.

# SECTION IV

## THIN-LAYER NAVIER-STOKES ALGORITHM

### 4.1 Explicit Treatment of Viscous Terms

The diffusive terms may be written as separate vectors in the thin-layer Navier-Stokes equations, Equation (2.9) becomes

$$\frac{\partial Q}{\partial \tau} + \frac{\partial F}{\partial \xi} + \frac{\partial (G-S_v)}{\partial \eta} + \frac{\partial H}{\partial \zeta} = 0 \quad (4.1)$$

where

$$S_v = J' \begin{bmatrix} 0 \\ \tilde{T}_{\eta x} \\ \tilde{T}_{\eta y} \\ \tilde{T}_{\eta z} \\ (u\tilde{T}_{\eta x} + v\tilde{T}_{\eta y} + w\tilde{T}_{\eta z} - \Gamma_\eta) \end{bmatrix}$$

and  $\tilde{T}_{\eta k}$  ( $k=x, y, \text{ or } z$ ) are defined in Equation (2.11).

Since the  $S_v$  vector is made up of diffusive terms which do not have the characteristics of a set of hyperbolic partial differential equations in which a set of characteristic velocities exist, it is impossible to split the diffusive terms into subvectors associated with any characteristic velocities and impossible to upwind difference these terms. Therefore, the inclusion of these terms into the left-hand side of either Equation (3.31) or Equation (3.45) would destroy the efficiency of the upper and lower triangular matrix solution, by requiring a central

differencing of these terms. In an effort to include the effects of viscosity and yet maintain the efficient structure of the algorithm Gatlin<sup>6</sup> has for stationary grids neglected the inclusion of the viscous flux jacobians in the left-hand side thereby treating the viscous terms explicitly. The result is the viscous terms at each iteration (n+1) are evaluated using the information (dependent variables and metrics) from the previous iteration (n).

An implicit, finite volume discretization of Equation (4.1) with the viscous terms becomes

$$\frac{\Delta Q^n}{\Delta \tau} + \frac{\delta F^{n+1}}{\Delta \xi} + \frac{\delta G^{n+1}}{\Delta \eta} + \frac{\delta H^{n+1}}{\Delta \zeta} = \frac{\delta S_v^{n+1}}{\Delta \eta} \quad (4.2)$$

However, instead of the linearization of Equation (3.4) for the viscous terms, they are linearized as

$$S_v^{n+1} = S_v^n + O(\Delta t) \quad (4.3)$$

The remaining fluxes are split and then linearized according to Equation (3.29) and the equation is factored into two factors in the same manner as described for Equations (3.33) as

$$\begin{aligned} & [I + \Delta \tau (\delta_\xi A^+ + \delta_\eta B^+ + \delta_\zeta C^+)] \\ & [I + \Delta \tau (\delta_\xi A^- + \delta_\eta B^- + \delta_\zeta C^-)] \Delta Q^n = -\Delta \tau R^n \end{aligned} \quad (4.4)$$

except now the residual term includes the viscous fluxes which contain derivatives with respect to the normal to solid surfaces,

$$R^n = (\delta_\xi F^n + \delta_\eta G^n + \delta_\zeta H^n + \delta_\eta S_v^n) \quad (4.5)$$

The residual vector in Equation (4.5) can be used in either a FVS (Equation (3.31b)) scheme or a FDS (Equation (3.45b)) scheme. This implementation maintains the solution algorithm efficiency of the original Euler algorithm (average increase in computational time is less than 10%) while including the viscous effects neglected in an Euler algorithm. Gatlin<sup>6</sup> has shown this algorithm to give reasonable engineering solutions for high Reynolds number flows when used with the FVS scheme for stationary grids. Results will be shown in this work for both FVS and FDS schemes and for both stationary and dynamic grids. The method used to evaluate the viscous flux terms has been described in detail by Gatlin<sup>6</sup> and is not repeated here.

#### 4.2 Boundary Conditions

All of the boundary conditions used have been applied explicitly. The boundary conditions are implemented using one layer of phantom points outside of the computational field, which results in a first order in space extrapolation at the boundaries and enhances the vectorization of the computer code. The phantom points at farfields are set to enforce a certain condition (supersonic or subsonic inflow or outflow) at the cell face, which is on the boundary, while at solid surfaces they are set to enforce the no-slip condition. The change in dependent variable,  $\Delta Q$ , is set equal to zero for all boundaries except at block boundaries.

All farfield and downstream boundaries used characteristic variable boundary conditions as derived in Reference 21 for stationary grids and

Reference 2 for dynamic grids. Characteristic variable boundary conditions are designed to allow information to flow into or out of the computational field as dictated by the signs of the eigenvalues.

The boundary conditions for impermeable surfaces are set using a no-slip implementation of the zero pressure gradient boundary conditions. These boundary conditions have been adapted for dynamic grids by observing the grid speed  $\vec{X}_b$  and the equations

$$\rho_p = \rho_f \quad (4.6a)$$

$$p_p = p_f \quad (4.6b)$$

$$\vec{V}_p = 2\vec{X}_b - \vec{V}_f \quad (4.6c)$$

$$e_p = p_p + \frac{1}{2} \frac{1}{(\gamma-1)} \rho_p (u_p^2 + v_p^2 + w_p^2) \quad (4.6d)$$

where, the subscripts p, f, and b, denote phantom points, field points, and boundary points respectively. Figure 4.1 shows graphically the implementation of no-slip condition for a cell centered formulation.

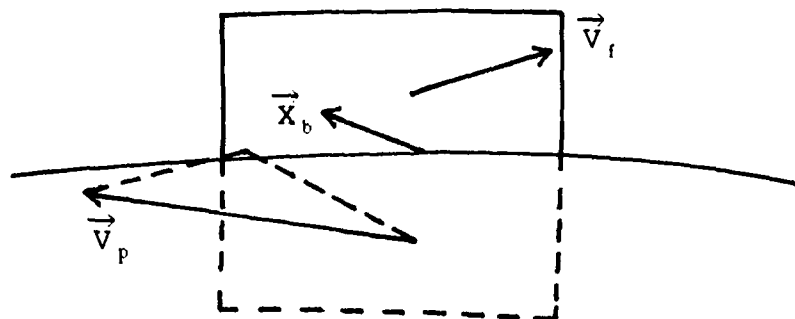


Figure 4.1 No-slip boundary conditions for dynamic grids.

Finally, the block-block boundary conditions were derived by Belk<sup>2</sup> for both stationary and dynamic grids. To summarize the discussions of different block-block boundary conditions, many combinations of treatment for  $\Delta Q^n$  and dependent variables at block boundaries exist. Those used for the results obtained here were, two phantom points,  $\Delta Q$  approximated (which results in local truncation error of  $O(\frac{\Delta t^2}{\Delta x})$ , see Belk<sup>2</sup>) and synchronized dependent variables.

#### 4.3 Turbulence Modeling

The numerical solution of the Navier-Stokes equations (Equation 2.1) for turbulent flows require the viscosity to be determined by the relation

$$\mu = \mu_0 + \mu_t \quad (4.7)$$

where  $\mu_0$  is the molecular viscosity and  $\mu_t$  is the eddy viscosity and is supplied by the turbulence model. Similarly, the thermal conductivity is determined by

$$K = K_0 + K_t \quad (4.8)$$

where  $K_0$  is the laminar conductivity and is obtained from

$$K_0 = \frac{\mu_0}{Pr(\gamma-1)} \quad (4.9)$$

while  $\mu_t$  is the turbulent conductivity determined from

$$K_t = \frac{\mu_t}{P_{rt}(\gamma-1)} \quad (4.10)$$

where  $P_r=0.72$  and  $P_{rt}=0.90$  for air.

Since the configurations studied here are airfoils and wings with little or no flow separation, the Baldwin-Lomax<sup>26</sup> turbulence model was selected. The Baldwin-Lomax turbulence model is a two-layer algebraic eddy viscosity turbulence model which uses a simple algebraic expression to determine a value for  $\mu_{t,i}$  in the inner layer nearer the wall and  $\mu_{t,o}$  in the outer layer. The Baldwin-Lomax model has the advantage of not requiring the determination of the edge of the boundary layer but relies instead on the vorticity profile to determine the  $\mu_t$  for the inner region:

$$\mu_{t,i} = \rho l^2 |\omega| \quad (4.11)$$

where

$$l = \kappa Y [1 - \exp(-Y^*/26)] \quad (4.12)$$

and

$$Y^* = Y \sqrt{\rho \tau_m} / \mu_w \quad (4.13)$$

$\omega$  is the vorticity,  $Y$  is the normal distance from the solid surface,  $\kappa=0.4$  is the von Karman constant,  $\tau_m$  is the maximum of  $\tau_w$  and  $\tau_s$ , where  $\tau_w$  is the wall shear stress and  $\tau_s$  is the maximum shear flow in a local velocity profile. The results of the selection of  $\tau_m$  in the flow solution is discussed by Gatlin<sup>6</sup>.



For the outer region the eddy viscosity is given by

$$\mu_{t,o} = KC_{cp} F_w F_{kleb} \quad (4.14)$$

where  $C_{cp}=1.6$  is a constant and  $K=0.0168$  is the Clauser constant.

$F_{max}$  is the maximum of the profile  $F(Y)$  given by

$$F_w = \min (Y_{max} F_{max}, C_{wk} Y_{max} \frac{U_{diff}^2}{F_{max}}) \quad (4.15)$$

and

$$F(Y) = Y|\omega| [1 - \exp(-Y^4/26)] \quad (4.16)$$

$Y_{max}$  is the  $y$  value at which  $F_{max}$  occurs.  $C_{wk}=0.25$

is a constant.  $F_{kleb}$  is the Klebanoff intermittency factor determined from

$$F_{kleb}(Y) = [1 + 5.5 (\frac{C_{kleb} Y}{Y_{max}})^6]^{-1} \quad (4.17)$$

where  $C_{kleb}=0.3$ .

$U_{diff}$  was defined by Baldwin and Lomax as the difference between the maximum and minimum velocity magnitudes in a profile

$$U_{diff} = (\sqrt{U^2 + V^2 + W^2})_{max} - (\sqrt{U^2 + V^2 + W^2})_{min}$$

#### 4.4 Time Accuracy and Subiterations

Calculations of unsteady aerodynamics requires a time accurate numerical scheme in which each grid cell is advanced in time an equal amount (i.e., minimum time stepping). The size of a time step is limited

by the Courant-Friedrichs-Lewy number (CFL), which is the number of cells across which a characteristic wave will propagate in one time step. If steady state solutions are of interest then it is possible to update each grid cell by an amount in time which places that cell at an optimum CFL number for convergence (i.e., local time stepping). This is not time accurate since each grid cell will be at different time levels, but this does not matter when a steady state solution is being sought where  $\Delta Q' \rightarrow 0$ . All the steady calculations presented here resulted from local time steps, while all the unsteady calculations resulted from minimum time steps in which each grid cell was updated the same increment in time.

The use of minimum time steps can be very expensive for viscous solutions since grid cells near solid surfaces are very small compared to grid cells in outer regions of the flow field (6-7 orders of magnitude difference in cell volumes). This means very small time steps must be used over the entire flow field for minimum time stepping to maintain a reasonable maximum CFL in the grid cells near solid surfaces. If a maximum CFL of 100 is occurring in the grid cells near a solid surface then, most of the flow field is being advanced in time with CFL's of much less than one ( $CFL \approx 0.001-0.00001$ ).

Belk<sup>2</sup> has shown good inviscid unsteady results using this FVS scheme for an oscillating airfoil in transonic flow using a maximum CFL of approximately 100. To obtain a maximum CFL of 100 on the inviscid grid it was necessary to take 500 time steps per cycle of oscillatory motion of the airfoil. To obtain the same approximate maximum CFL (100) on a viscous grid would require approximately 500,000 time steps for one

cycle of motion. Obviously unsteady viscous calculations for maximum CFL numbers on the order of 100 are very expensive and are not practical even on today's fastest computers.

If unsteady viscous calculations are to become a practical tool for use in design and analysis of transonic fighter aircraft and weapons then it will be necessary to reduce the number of time steps needed for a calculation (i.e., increase the max CFL allowed). With this implicit algorithm a linear stability analysis indicates an unconditionally stable scheme. Gatlin<sup>6</sup> discusses stability concerning the explicit treatment of the viscous terms. His linear stability analysis indicates the scheme maintains its unconditional stability for high Reynolds number flows only. For unsteady problems it is not enough to simply remain stable, one must also maintain time accuracy when using these large CFL numbers.

A test case used to study the effect of CFL on stability and time accuracy was the NACA 0012 airfoil oscillating in pitch about its quarter chord point in transonic conditions. The conditions used in these calculations were taken from the experiment by Landon<sup>27</sup>, with Mach number of 0.755, mean angle of attack,  $\alpha_0$ , of  $0.016^\circ$ , an unsteady angle of attack amplitude,  $\alpha_u$ , of  $2.51^\circ$ , and a reduced frequency or Strouhal number,  $k$ , of 0.1628 based on chord length,

$$k = \frac{\hat{\omega} \hat{c}}{\hat{V}_\infty} \quad (4.19)$$

where

$\hat{\omega}$  = frequency

$\hat{c}$  = chord length

and

$$\hat{V}_{\infty} = \text{freestream velocity}$$

The angle of attack of the airfoil was varied according to

$$\alpha(t) = \alpha_0 + \alpha_u \sin(\hat{\omega}t) \quad (4.20)$$

Unsteady viscous calculations for the NACA 0012 airfoil at these conditions were made for different time step sizes to determine the effects of large CFL numbers on unsteady viscous calculations. All of the NACA 0012 calculations presented were obtained using a "C" type numerical grid shown in Figure 1 with 221x40 points. The grid was generated using the Numerical Grid Generation Code - EAGLE written by Thompson (Reference 28). A great deal of effort was expended to generate a grid which had as much orthogonality as possible at the airfoil surface (see Figure 1.b), since the FDS scheme was found to be very sensitive to orthogonality. The spacing set for the first point off the body was 0.000001 which gave approximately 15-20 grid cells inside the boundary layer and resulted in a minimum  $Y^+$  of much less than 1 (actually 0.1) over the entire airfoil.

The unsteady calculations were performed by first obtaining a steady solution for the airfoil at the mean angle of attack,  $\alpha_0 = 0.016^\circ$ . The motion was impulsively started with the angle of attack varied according to Equation (4.20). The entire grid was oscillated as a rigid body. The pressure distributions for several different time step sizes are presented in Figure 2. These pressure distributions are "snap-shots" of the pressure in time as the airfoil is in motion. The airfoil is at the 60° of motion point which corresponds to an increasing angle of

attack through  $2.20^\circ$ . The small time step size  $\Delta T = 0.00102$  was used as a reference time step to compare with other results in order to check for time accuracy. As the time step increases the solution deteriorates to the point of being unusable even though the solution did not "blow-up" and continued for a complete cycle. Table II summarizes the results in Figure 2, two additional time step sizes have been included in Table II for comparison purposes.

The results shown in Figure 2 certainly indicate that if unsteady viscous calculations for the oscillating airfoil are to be practical or affordable, additional considerations must be made to allow calculations on the order of 1000 time steps per cycle of motion or less. An approach taken to help in this cause was a use of Newton iterations to converge the solution at each time step before updating to the next time step. These Newton iterations, referred to here as subiterations, have been tried successfully by others (see Reference 17), but not with the two algorithms described in paragraphs 3.1 and 3.2 and not with the explicit treatment of the viscous terms.

The implementation of subiterations into the scheme described by Equations (3.31 or 3.46) is a simple additional term added to the right-hand side and a redefinition of  $\Delta Q^n$  on the left-hand side. Using the FVS scheme as an example (the implementation is exactly the same for the FDS scheme), one has

$$[I + \Delta T (\delta_\xi A^+ + \delta_\eta B^+ + \delta_\zeta C^+)]$$

$$[I + \Delta T (\delta_\xi A^- + \delta_\eta B^- + \delta_\zeta C^-)] \Delta Q^n = -\Delta T R^n \quad (4.21a)$$

$$-\Delta T R^p = -\Delta T \left[ \frac{Q^p - Q^n}{\Delta T} + (\delta_\xi F^p + \delta_\eta G^p + \delta_\zeta H^p + \delta_\eta S_v^p) \right] \quad (4.21b)$$

where  $\Delta Q^p$  is defined as

$$\Delta Q^p = Q^{n+1} - Q^p \quad (4.21c)$$

where  $p$  is the subiteration count. When  $p=0$ ,  $Q^p = Q^n$ , and the system reverts to the noniterative scheme of Equation (3.31). At convergence,  $Q^p \rightarrow Q^{n+1}$ . Note that in this case the viscous terms are not time lagged. The normal operating procedure was to simply set the number of subiterations desired rather than check the convergence level after each subiteration.

Oretga and Rheinboldt<sup>29</sup> write the Newton iteration in the form

$$X^{p+1} = X^p - F'(X^{k(p)})^{-1} F(X)^p \quad p=0,1,2,\dots \quad (4.22)$$

where  $k(p)$  is an integer less than or equal to  $p$ . When  $k(p)$  is less than  $p$  then the  $F'(X)$  is re-evaluated less than each iteration which translates into "freezing" the flux jacobians. When  $k(p) = p$  the jacobians are evaluated each iteration and Equation (4.22) results in the normal Newton iteration

$$X^{p+1} = X^p - F'(X^p)^{-1} F(X)^p \quad p=0,1,2,\dots \quad (4.22)$$

When  $k(p) = 0$  the jacobians are never updated and Equation (4.22) is then referred to as the simplified Newton method

$$X^{p+1} = X^p - F'(X^0)^{-1} F(X)^p \quad p=0,1,2,\dots \quad (4.23)$$

The significance of freezing the jacobians and the resulting simplified Newton method is a tremendous savings in computations since the cost to recalculate the flux jacobians is between 40% - 45% of the cost of doing an entire iteration. Both methods were tried with no noticeable differences in the results, therefore, only the simplified Newton method results will be reported on.

Pressure distributions for the NACA 0012 at 60° motion are shown in Figure 3 for two time step sizes. The smaller time step size,  $DT = 0.0511$ , (see Table III for a description of the conditions for the subiteration check cases) shows some moderate wiggles for the zero subiterations while for only four subiterations the solution is much smoother and is suitable for determining the lift and moment coefficients for use in design and analysis studies. However, for the larger time step size,  $DT = 0.2044$ , the original solution without subiterations is very irregular and even after 32 subiterations the solution still shows (Figure 4) a significant number of wiggles. The solution could be smoothed but would require numerous subiterations due to the slow convergence rates for the subiterations and would not be cost effective.

The idea of using subiterations for unsteady calculations was to converge the solution at each time step and therefore allow for much larger time steps sizes. However, Swanson and Turkel<sup>30</sup> have reported on the problems of converging solutions with numerical grids designed for viscous flows which have a large variation in grid cell aspect ratio between grid cells near a solid surface and grid cells in the far field. A solution for the convergence rate problem in

subiterations which worked well was to use the idea for accelerating steady state convergence, that is local time stepping.

Local time steps used for the subiterations seemed to have a tremendous impact on the convergence rate for the subiterations. The local time steps were implemented such that the overall time accuracy of the minimum time step iterations was preserved. Equation (4.21b) then becomes

$$-\Delta T R^p = -\Delta T_{local} \left[ \frac{Q^p - Q^n}{\Delta T_{min}} + (\delta_{\xi} F^p + \delta_{\eta} G^p + \delta_{\zeta} H^p + \delta_{\eta} S_v^p) \right] \quad (4.25)$$

The result of using local subiterations, Equation (4.25), was a significant increase in the convergence rate for subiterations as long as the CFL for the local subiterations was small enough to maintain stability. Numerical experiments showed that the local CFL must usually be less than one. This fact would eventually become the Achilles heel for local subiterations since, determining the optimum local CFL number which allowed the Newton subiterations to remain stable and still converge rapidly, proved to be extremely difficult. A method guaranteed of selecting the optimum local CFL number was not found; however, provided a proper value for the local CFL was found the local subiterations converged faster than the minimum time steps.

The pressure distributions in Figure 5 show very smooth results for time step size,  $DT = 0.05111$ , using local time stepping subiterations even for only two subiterations. The results in Figure 6 show much smoother pressure distributions for time step size,  $DT = 0.2044$ , than did the minimum time steps (Figure 4). Even though there is a



significant amount of ringing near the shock, this solution would seem to be sufficiently smooth to give reasonable engineering answers for lift and moment coefficients.

Figure 7 shows a comparison for the time step size,  $\Delta T = 0.05111$ , with 4 minimum subiterations and 4 local subiterations. The results are very similar for the two cases. However, both subiteration cases show the shock wave farther aft than does the smaller time step size with no subiterations. Since the shock is still building in strength and moving aft, the larger time step size shock position is said to be "leading" the smaller time step size. This situation was consistently observed for these large time step size calculations.

The time accurate calculation of unsteady aerodynamics would at first glance seem to require a second order temporal accurate scheme. However, Belk<sup>2</sup> has shown that for Euler calculations on oscillating airfoils and wings there is very little difference between solutions obtained with a second order accurate scheme and those obtained using a first order accurate scheme. The extension of the Euler algorithm to include the diffusive terms (paragraph 4.1) requires the diffusive terms to be time lagged and results in a first order scheme regardless of the time discretization used. For example, consider the linearization as described in Equation (3.4)

$$F^{n+1} = F^n + A^n \Delta Q^n + O(\Delta t^2) \quad (3.4)$$

When this linearization is used in conjunction with the second order time discretization given in Equation (3.5b) the result is a second order

accurate scheme. When Equation (3.4) is used in conjunction with the first order time discretization given in Equation (3.5a), the result is a first order accurate scheme. When the viscous terms are added explicitly using the linearization given in Equation (4.34), the formal time accuracy is dropped to  $O(\Delta t)$  regardless of the order of the time discretization used, either Equation (3.5a) or (3.5b).

The use of subiterations would, it appears, alleviate this problem of time accuracy, since at convergence, the linearization and factorization errors go to zero. Therefore, using the second order time discretization described in Equation (3.5b) with subiterations, gives a second order accurate in time scheme at convergence. A comparison of a first and second order differencing with,  $DT = 0.0511$ , is shown in Figure 8 using 16 minimum subiteration time steps, which resulted in an order of magnitude reduction in the residuals. There are some differences, with the major difference being the shock location. Since the shock at this point in the motion is still strengthening and moving aft very rapidly, then, as would be expected, the first order shock position lags the second order shock position.

The result of these investigations was to help select the time step sizes, number and type of subiterations to be used for calculations of the oscillating airfoil and wings for several cycles of motion. Minimum time step subiterations were used because of the problems of selecting the local CFL for the local time step subiterations. A time step size considered appropriate for inviscid calculations was used with 4-5 subiterations, which resulted in a good tradeoff between cost and accuracy. These results will be presented in Section VI, but first a

comparison of the FVS and FDS schemes for steady viscous calculations will be presented in Section V.

## SECTION V

### STEADY RESULTS

The description of the splitting techniques in Section III indicated the FDS scheme based on Roe's approximate Riemann solver should outperform the FVS scheme (BMULE) based on the Steger-Warming splitting. Van Leer and Gatlin have pointed out that the numerical dissipation for the FVS scheme is too large to allow the accurate modeling of flow discontinuities such as shocks and boundary layers. In order, to document the effects of numerical dissipation for viscous flow solutions, several steady configurations were tested to compare the FDS scheme with the FVS scheme.

#### 5.1 Flat Plate Boundary Layer

The first configuration was a laminar flat plate boundary layer calculation for Mach = 0.5 and a Reynolds number based on plate length of  $Re = 10,000$ . Flow solutions for a laminar boundary layer on a flat plate were obtained using two grids. Both grids used 70 points in the freestream direction with 10 points in front of the plate stretched from the outer boundary, located 4.0 plate lengths in front of the plate to the plate leading edge. The next 50 points were uniformly distributed on the plate, and the last 10 points were placed aft of the plate, stretched from the plate trailing edge to 5 plate lengths downstream of the plate. The two grids differed in the number of grid lines in the normal direction from the plate and in the spacing set for the first point off the plate. The first grid used 20 points in the normal direction with the first point off the plate set at 0.002 plate lengths (fine grid), while the second grid used 15 points in the normal direction and the

first spacing was 0.02 plate lengths (course grid).

The laminar boundary layer profiles are presented in Figure 9 for the Roe scheme on the course grid, and EMULE on both the course and fine grids. The calculations are shown compared with the Blasius solution for a laminar flat plate. The Roe scheme matches very well with the Blasius solution using the course grid. Note that the Roe scheme has successfully modeled the laminar boundary layer profile with only three mesh points internal to the boundary layer. The fine grid results with the EMULE scheme do not compare as well as the Roe scheme. The additional grid refinements did not improve the EMULE results. The EMULE scheme has too much numerical dissipation to capture the laminar boundary layer profile, even on the fine grid.

Calculations with the two schemes were also completed for a turbulent flat plate boundary layer. While the Roe scheme still outperformed the EMULE scheme, the differences were not so dramatic. The Roe scheme was able to model the turbulent boundary layer with a relatively course grid once again. However, it was necessary to ensure that at least one grid point was inside the laminar sublayer of the turbulent boundary layer. Therefore, the Roe scheme or the EMULE scheme requires a spacing for the first grid point off the body to be such that a minimum  $Y^+$  (Equation 4.13) of less than 2-3 occurs. This criterion was used in the remaining calculations to ensure the turbulent boundary layers were being satisfactorily modeled.

## 5.2 RAE 2822 Airfoil

The RAE 2822 airfoil was used as a check case for the thin-layer

Navier-Stokes algorithms using both Roe and EMULE. The RAE was selected because of the experimental data<sup>31</sup> which exists for pressure, skin friction, and velocity profiles.

The RAE 2822 is a supercritical airfoil as shown in Figure 10, with a design Mach number of 0.66. A  $221 \times 31 \times 2$  grid was used to compute the flow for the case presented. The 31 grid points were stretched from  $1 \times 10^{-6}$  spacing for the first point off the body (close enough to guarantee a minimum  $Y^+ < 1$ ), 5 chord lengths to the front farfield boundary, and 10 chord lengths to the top and bottom farfield boundaries. The downstream boundary was set at 15 chord lengths with 30 points in the wake. The remaining points (160) were spread around the airfoil, with clustering at the leading and trailing edges.

Flow solutions were obtained for the RAE using the grid described above for four algorithm combinations. The Roe scheme was used with minmod limiter in both the second and third order spatially accurate mode, and with the superbee limiter, which is second order accurate. The EMULE scheme was used to compare with each of the Roe scheme algorithms. The flow conditions for the computation were taken at Mach = 0.73 and angle of attack =  $3.19^\circ$ . The flow conditions were corrected to account for flow angularity and wall effects to the condition recommended by Cook et al<sup>31</sup>. The calculations were at Mach = 0.734 and angle of attack =  $2.79^\circ$ . The Reynolds number for both the experiment and the calculations was  $6.5 \times 10^6$ , based on chord length.

Figures 11.a - 11.d show the comparison for the Roe minmod limiter with 2nd order spatial accuracy and the BMULE 2nd order accurate scheme. Figure 11.a shows the pressure distribution, while 11.b, and 11.c show comparison of velocity profiles at two stations on the upper surface of the airfoil. Figure 11.b shows the velocity profile at 32% of the chord, which is well ahead of the upper surface shock, while Figure 11.c shows the velocity profile at 57% chord, which is very near the upper surface shock. Figure 11.d shows a comparison of skin friction between the two algorithms and experimental data for the upper surface.

Figures 12.a - 12.d and Figures 13.a - 13.d follow the same pattern as Figures 11.a - 11.d, with Figures 12 comparing the Roe minmod 3rd order scheme with the BMULE, and Figure 13 comparing the Roe superbee 2nd order scheme with the BMULE scheme.

Each of the algorithm cases compare very favorably with the pressure data (Figures (11 - 13).a). Roe schemes match better in the shock regions due to the numerical dissipation in the BMULE scheme smearing the shocks. The Roe superbee scheme was the only one to accurately model the leading edge expansion for the RAE. However, the Roe superbee did not do as well in the shock region due to superbee predicting a small shock induced boundary layer separation bubble, which was not evident in the experimental data or in the other calculations.

The velocity profiles shown in Figures (11,12,13)b-c are plotted as  $UC/U_e$  (contravariant velocity/contravariant velocity at the edge) versus the normal coordinate distance from the upper surface. The edge of the boundary layer was determined to be the cell at which the

maximum  $U^*$  and contravariant velocity values occurred. When these maximum values did not occur in the same grid cell, a simple averaging was used to determine  $U_e$ . As is evident in all the plots, the Roe scheme is far superior to the BMULE scheme. The BMULE scheme consistently predicts a thicker boundary layer than that shown in the experimental data. This again is attributed to the numerical dissipation in the BMULE scheme. The superbee limiter as discussed above predicts some flow separation behind the shock which is made more evident by observing the velocity profile for 57% chord position, Figure 13.c. In all other cases the Roe scheme compares very well with the experimental velocity profiles, and this is true for these calculations even though the grid contained 10 less points in the normal direction than did Gatlin's 6, which would be considered by some as already being a sparse grid. (See References 32 and 33.)

A comparison of skin friction between the Roe scheme, BMULE scheme, and experiment are shown in Figures (11-13)d. Both the Roe scheme and BMULE tend to overpredict the skin friction when compared to experimental data. Most of the calculations match well with the experimental data up to the shock location, but both schemes tend to greatly overpredict the skin friction behind the shock. The skin friction data near the trailing edge for Figures 11.d and 12.d was lost due to a data file transfer error. Once again the evidence of superbee's separated region behind the shock is evident in Figure 13.d.

Even though the Roe scheme gives improved results in almost all cases shown, the improvements do not come cheaply. Figure 14 shows a convergence history for the two schemes. Obviously, the BMULE scheme



converges much faster than does the Roe scheme, so much so that after only 800 iterations at a CFL = 15, the BMULE residuals are nearly an order of magnitude smaller than are the Roe scheme residuals. Numerical experimentation showed that 800 iterations was the minimum necessary to obtain engineering answers (after which the solution did not change) for the Roe scheme while only 500 was necessary for BMULE. This translates into many fewer iterations necessary to arrive at the same convergence level for the BMULE scheme. When this is added to the fact that the Roe scheme has a higher operations cost than does BMULE, nearly 20%, since BMULE runs at  $6.185 \times 10^{-5}$  CPU sec/iteration/point while Roe runs at  $7.417 \times 10^{-5}$  CPU sec/iteration/point, it becomes evident the Roe scheme is much more expensive to use.

### 5.3 ONERA M6 Wing

The ONERA M6 is a symmetric 12% thick airfoil section with a sweep angle of 30 degrees. The wing is tapered with a taper ratio of 0.56 and has an aspect ratio of 3.8. Extensive wind tunnel test data exist for the ONERA, in particular pressure data for transonic flow conditions (Reference 34). The ONERA is used here to compare the BMULE scheme and the Roe scheme with experimental data for a steady three-dimensional configuration at Mach = 0.84, angle of attack = 3.06 degrees, and  $Re = 2.6 \times 10^6$ .

The grid used in these calculations was a 111 x 40 x 25 "C-0" type grid. The grid was generated using a distribution similar to that used for the NACA 0012 airfoil grid described in paragraph 4.4. The upper and lower airfoil sections in this grid were generated independently with the first point in the grid (1,1,1) being at the wing leading edge. The grid

used a spacing  $1 \times 10^{-6}$  for the first spacing off the body, which resulted in a  $\min Y^+ < 1$  over the entire grid. The outer boundaries were extended to 10 chord lengths in all directions. Figure 15 shows a closeup of two K planes (constant spanwise location) and the airfoil section. The grid was generated by letting the  $K=1$  plane be the plane of grid points on the upper wing surface at the root section. The K-planes were then distributed linearly along the upper surface to  $K=8$  at the upper surface tip (Figure 15.b). Planes 9 through 17 were then rotated in a circular arc to model the wing tip, while K-planes 18 through 25 on the lower surface were distributed linearly from the tip to the root. This wraparound wing tip grid shown in Figure 15.c, allows the modeling of the wing tip as it existed in the wind tunnel model.

The test case was run for four algorithms just as for the RAE airfoil. The BMULE algorithm was compared to the Roe algorithm using the 2nd order minmod limiter, 3rd order minmod, and 2nd order superbee limiter. The test case was a transonic condition which results in a double shock configuration, which is evident in Figure 16.a at near midspan point (44%). Figure 16.b at the 65% semispan location also shows a double shock, but with the separation distance between the two shocks decreasing. Finally, Figure 16.c shows the pressure distribution at 95% semispan location, where only a single shock exists in the flow. The configuration obviously results in the lambda double shock pattern for transonic conditions on a swept wing, where the two shocks coalesce to form a single shock near the wing tip. The results follow the same pattern as the RAE airfoil, where the Roe scheme consistently models shocks in much fewer points with less smearing. None of the schemes show any sign of flow separation, which also agrees with the experimental

data. Figure 17 shows a series of pressure contours along the wing span. The contours in Figure 17.a at 44% semispan location clearly show a weak shock at the 20% chord position and a much stronger shock near the 60% chord position. Figure 17.b shows the result at 65% semispan location. Strong shocks exist at about the 20% and 50% chord positions, and the rear most shock is located further forward. The 95% semispan location (Figure 17.c) clearly shows the shocks having coalesced to form one at the 25% chord position and this shock is by far the strongest shock of all those observed in Figure 17. Figure 17.d shows a view of the contours along the upper surface and the double shock pattern coalescing into a single shock at the tip. These solutions compare well with the experimental data. The comparison of the Roe scheme with the BMULE scheme is as expected. The Roe scheme shows slightly improved results in the leading edge expansion region and directly downstream. The Roe scheme is obviously superior again in all shock regions where BMULE has smeared the shocks over several grid cells. There is little or no difference between the two solutions for the lower surface calculations.

## SECTION VI

### UNSTEADY RESULTS

#### 6.1 Oscillating NACA 0012 Airfoil

Unsteady two-dimensional calculations were performed for the NACA 0012 airfoil oscillating in pitch about the 25% chord point as described in paragraph 4.4. The grid used was the same as previously presented in Figure 1. The calculations presented in paragraph 4.4 were all for only the first 60 degrees of oscillatory motion. The calculations were all stopped at this point in the cycle to compare results from different time step sizes and subiteration combinations. The results to be presented here are examples of taking selected cases from those presented previously and continuing the motion for a full 4 cycles (1,440 degrees of oscillatory motion) and comparing the lift and moment coefficient time histories and selected "snap-shots" of the pressure distributions from the last cycle of motion.

The first case presented is a comparison of 4 minimum time step subiterations and 4 local time step subiterations both for  $DT = 0.05111$ , which corresponds to a maximum CFL of 45,000 compared with a 0 subiteration case using a  $DT = 0.005111$  time step. The 0 subiteration case at  $DT = 0.005111$  was used at the small time step for comparison purposes instead of the  $DT = 0.00102$ , which was used for the first 60° motion cases. This larger time step was selected for cost savings, since to calculate 4 cycles of motion with the small time step ( $DT = 0.00102$ ) would require 200,000 iterations, while the larger ( $DT = 0.005111$ ) required 40,000 iterations. The lift coefficient versus time plot is shown in Figure 18.a and the moment versus time shown in Figure 18.b.

Only a slight difference in the lift curve is noticeable at the maximum and minimum values of lift due primarily to the slight displacement of the shock location resulting from the larger time steps. The difference is more pronounced for the moment curves (Figure 18.b).

The second case presented is a comparison of a one-block grid and a three-block grid shown in Figure 19 for the NACA 0012 airfoil. Four minimum time step subiterations were used for both the one-block and the three-block grids with a time step of  $DT = 0.05111$ . Figure 20.a - 20.h show snap-shots in time of unsteady pressure distributions for the two blocking arrangements. The slight differences in some of the pressure distributions can be attributed to a couple of reasons. First, as mentioned in Section IV the boundary conditions used at block interfaces were those developed by Belk, and the error generated by approximating the  $\Delta Q$  ( $O(\Delta t^2/\Delta x)$ ) causes a slight misplacement of the shock position between the one and three block cases, especially for the times when the shock is traveling the fastest (i.e., Figures 20.a and 20.e). Secondly, the use of blocks degrades the convergence rates for steady solutions (see Belk<sup>2</sup>) and as a result the subiterations for the three-block case do not converge as rapidly as do the subiterations for the one-block case, which accounts for the slight differences in the unsteady pressure distributions elsewhere in the solution.

Figure 21 shows the pressure contours for the three-block case at the end of the fourth cycle of motion. Note that even though the airfoil is back to the 0 degree angle of attack position, the flow field is not symmetric and a relatively strong shock still exists on the lower surface. This is a good example of how the aerodynamics lag the

time-dependent motion of the body.

The third and last two-dimensional case presented is a comparison of the same 4 minimum time step subiteration case using the first order backward Euler differencing formula, Equation (3.5a), compared with 4 minimum time step 2nd order subiteration using the three-point backward difference formula given in Equation (3.5b). Figure 22 show snap-shots of the unsteady pressures at the same times as shown in Figure 20, compared with the experimental data<sup>27</sup>. As noted by Belk<sup>2</sup> this data is somewhat suspect due to obvious asymmetric properties, even though the solution should be very nearly a symmetric solution. Belk determined a steady angle of attack somewhat larger than the  $0.016^\circ$  should be used to improve the correlation between experimental data and calculations.

The second order solutions show the shock leading the shock location predicted by the first order solutions for  $DT = 0.005111$  and  $DT = 0.05111$  with 4 minimum subiterations. The largest difference occurs when the shock is traveling the fastest, such as the  $70^\circ$  of oscillatory motion (Figure 22.b). Note that at the point where the shock is basically stationary (i.e.,  $160^\circ$  of motion) the two  $DT = 0.05111$  cases for first and second order schemes are essentially identical. At all the times shown in Figure 22 the second order solution shows a closer agreement with the experimental data than does the two first order solutions.

The comparison of the 2nd order solution and the experimental data indicates an even closer agreement between the two would be possible if a

slightly larger steady angle of attack was used for the calculations. For example, a larger steady angle of attack added to the unsteady angle of attack would in Figures 22.b - 22.d result in a larger expansion region and a shock location farther aft as indicated by the experimental data. Likewise, in Figures 22.f - 22.h when the airfoil is at negative angle of attack a larger (more positive) steady angle of attack would result in a smaller expansion region on the lower surface and the shock located farther forward as indicated by the experimental data. This confirms Belk's findings on the same subject.

## 6.2 Oscillating Supercritical Rectangular Planform Wing

The supercritical rectangular planform wing was used as the three-dimensional unsteady check case for this work due to the extensive amount of wind tunnel test data<sup>35</sup> that exist. The wing has an aspect ratio of 2 and was oscillated about the wing pitch axis located at the 40% chord. The experimental data used was taken in Freon, and therefore the ratio of specific heats is  $\gamma = 1.131$  with a transonic Mach number of 0.7 and a steady angle of attack of  $4^\circ$ .

The grid for this case had  $221 \times 40 \times 15$  points. The grid used a "C" mesh in the streamwise direction and a "H" mesh in the spanwise direction. Each of the K planes (constant spanwise location) have the same point distribution as the two-dimensional grid used for the NACA 0012 airfoil calculations, Figure 1.a, with clustering at the leading and trailing edges. The distribution was selected to give the most orthogonal grid possible, Figure 23.a. There are 10 such planes of data distributed down the wing span, with the planes being clustered near the

tip. The wing tip was not modeled in this case as was done for the ONERA M6 wing, but instead the airfoil was simply collapsed to a line at the  $K=11$  plane, which was placed just out from the wing tip. An additional 4 grid planes were distributed in the spanwise direction to the farfield boundary (Figure 23.b). The spacing for the first point off the wing was such that a minimum  $Y^+$  of 1.5 occurred on the wing.

The grid described was used for steady calculations to compare with the experimental data from Reference (35) to verify the quality of the grid before performing the unsteady calculations. The results near the wing tip are of particular interest since the grid used did not model the tip correctly. The transonic flow conditions were  $Mach = 0.701$  and  $4.0^\circ$  angle of attack, which was considerably different from the supercritical design conditions of  $Mach = 0.8$  and  $0.0^\circ$  angle of attack, and results in a sharp shock near the 20% chord. The Figures 24.a - 24.d show excellent agreement with the experimental data and confirm the quality of the grid (including the collapsed wing tip) to accurately model the flow field for the rectangular wing. Belk<sup>2</sup> has reported a predicted shock position downstream of the position shown in the experimental data using an inviscid approximation. The inclusion of the viscous terms has corrected the position of the predicted shock to more nearly coincide with the experimental data.

The three-dimensional unsteady calculations were obtained at a Mach number 0.699 and a steady angle of attack of  $4.03^\circ$ . The angle of attack was varied according to Equation (4.20) with an unsteady amplitude of  $1.035^\circ$  and a reduced frequency, Equation (4.19), of 0.358.



A steady starting condition was obtained using a CFL of 5 for 1,000 iterations, after which the motion was impulsively started. The calculations were run for three cycles of motion. During the third cycle the pressure coefficients were saved at each time step. The time step size was  $DT = 0.069$ , which corresponds to 360 time steps per cycle of motion (same as used by Belk<sup>2</sup> for the inviscid calculations), and 5 minimum time step subiterations were used to converge the solution at each time step by nearly one order of magnitude. The maximum CFL for this case was approximately 17,000.

The magnitude and phase of the unsteady pressure coefficients from the third cycle of motion was obtained by Fourier analysis. The magnitude and phase of the unsteady pressure coefficients are presented along with the inviscid results from Belk<sup>2</sup> and the experimental data<sup>35</sup>, for the semispan locations in Figures 25.a - 25.g. Again the predicted results compare well with the experimental data. Belk<sup>2</sup> reported a misplacement of the sharp spike in magnitude of the unsteady pressure coefficient due to the inviscid code misplacing the shock. Once again the inclusion of the viscous terms has seemingly corrected this problem to give good agreement with the experimental data.

The good comparisons tend to drop off as the wing tip is approached, such that at the 95% semispan location the phase comparison with the experimental data (Figure 25.f and 25.g) is not as good. The shift in the phase for the upper surface is obviously misplaced, and the phase for the lower surface is consistently under predicted. The story is similar but not as severe at 85% semispan location. It should be noted that the experimental data at this station for the lower surface is highly

suspect, since the data does not follow the obvious trend of the data at the stations on either side (inboard or outboard). The reduced accuracy at the tip should come as no great surprise considering the grid treatment of the wing tip. Belk's <sup>2</sup> results, while showing some decline in accuracy near the tip, do not show as dramatic a change. This strengthens the argument for blaming the grid topology used ("C-H") since Belk used a ("C-O") type grid similar to the one used in this work for the ONERA wing.

## SECTION VII

### CONCLUSIONS

Two algorithms have been presented for computing unsteady thin-layer Navier-Stokes solutions for oscillating airfoils and wings. The algorithms, flux vector split (FVS) and flux difference split (FDS) were first compared for steady viscous calculations. The computed laminar boundary layer profiles for a flat plate were compared with the Blasius solutions and the FDS was the clear winner since it managed to capture the laminar profile with only three grid points inside the boundary layer, while with four times as many grid points inside the boundary layer, the FVS scheme could still not match the comparison of FDS with the Blasius solutions. The inability of the FVS scheme to capture a laminar boundary layer is due to the excessive numerical viscosity in the scheme. Similar improvements in the computed steady solutions for the RAE 2822 airfoil and the ONERA M6 wing were observed for the FDS scheme. The numerical dissipation in the FVS scheme is also observed in shocks in the form of smearing the shock waves over several grid cells. The improved solutions for the FDS scheme did not come cheap, since the FDS scheme has a higher operational count than does the FVS (approximately 20% higher), and the convergence rate for the FDS scheme is slower than the FVS scheme, therefore requiring more iterations to reach the same convergence level (approximately 25% more iterations).

The second order FDS scheme with the minmod limiter was selected as the algorithm to be used for the unsteady thin-layer Navier-Stokes computations. The emphasis was placed on obtaining time-accurate viscous

solutions for oscillating airfoils and wings as cheaply as possible. Since the diffusive terms were treated explicitly, the formal temporal accuracy of the algorithm without subiterations was limited to 1st order accurate. A form of Newton subiterations was implemented to converge the unsteady calculations at each time step before progressing the solution to the next time step. The use of these subiterations then allowed the calculations to progress at much larger time step sizes (and CFL number) than would otherwise be possible. The use of subiterations also provided the capability for a 2nd order time accurate scheme at convergence of the subiterations.

The use of subiterations were shown to significantly improve the quality of the solution, and in some cases allow a solution to be obtained which otherwise would have been impossible at the time step size being used. Unsteady calculations for the two-dimensional NACA 0012 airfoil were performed to help select the proper combinations of the step size and subiteration number to give the best possible solution. The results from these calculations were used to make more extensive two and three-dimensional unsteady calculations to compare with experimental data. The three-dimensional calculations for the supercritical rectangular planform wing showed excellent agreement with the experimental data, and the use of subiterations with the FDS scheme resulted in a relatively efficient algorithm which could be used in more complex three-dimensional unsteady viscous calculations.

TABLES

TABLE I  
SECOND ORDER TRUNCATION ERROR

$\psi$	NAME	$b$	2nd order TE
$1/3$	Third-Order	4	0
-1	Fully Upwind	2	$\frac{1}{3}(\Delta x)^2$
0	Fromm's	3	$\frac{1}{12}(\Delta x)^2$
$1/2$	Low <del>TE</del> 2nd order	5	$-\frac{1}{24}(\Delta x)^2$
1	Central	$\infty$	$-\frac{1}{6}(\Delta x)^2$
$-1/3$	No Name	$\frac{5}{2}$	$\frac{1}{6}(\Delta x)^2$

TABLE II

## SUMMARY OF TIME STEP SIZE RUNS \*

TIME STEP	# ITERATIONS	CPU SECONDS	# SUBS
0.0010	8250	46060	0
0.0051	1640	9161	0
0.0102	833	737	0
0.0511	167	149	0
0.1022	83	76	0
0.2044	42	39	0

\* First 60° of motion.

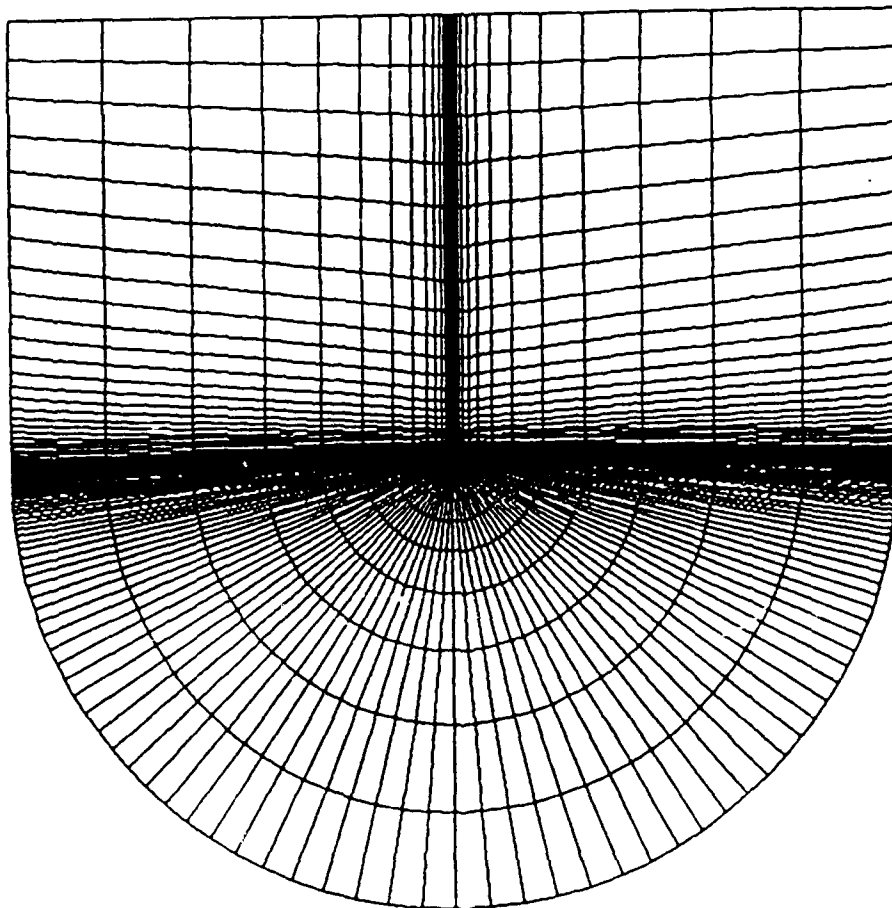
TABLE III  
SUMMARY OF SUBITERATION RUNS \*

TIME STEP	# ITERATIONS	CPU SECONDS	# SUBS
0.0511	167	1546	16 MIN
0.0511	167	497	4 MIN
0.0511	167	324	2 MIN
0.2044	42	729	32 MIN
0.2044	42	383	16 MIN
0.2044	42	214	8 MIN
0.0511	167	1530	16 LOCAL
0.0511	167	495	4 LOCAL
0.0511	167	322	2 LOCAL
0.2044	42	735	32 LOCAL
0.2044	42	382	16 LOCAL
0.2044	42	208	8 LOCAL

\* First 60° of motion.

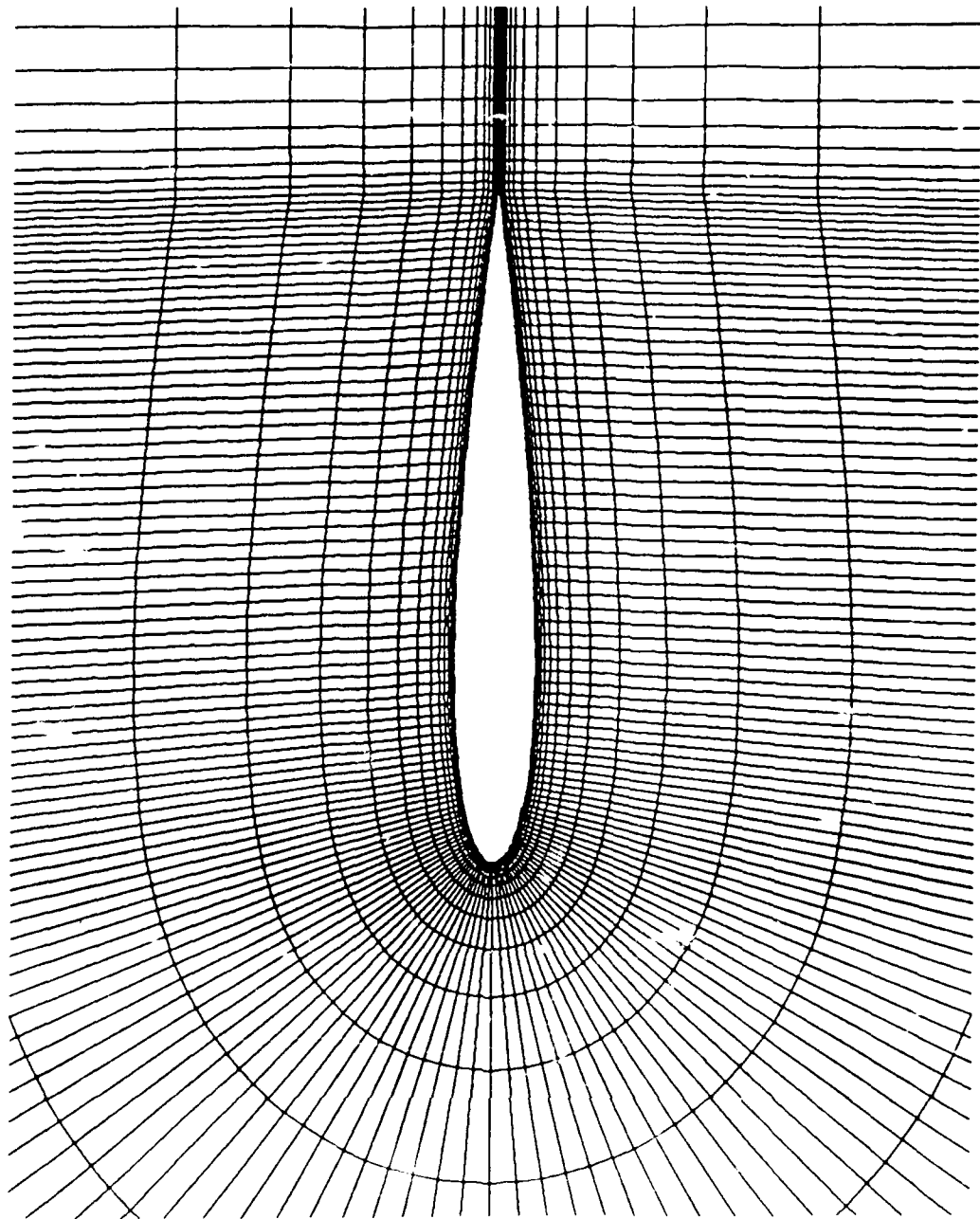


FIGURES



a. 221 points in the streamwise direction, 40 points in the normal direction

Figure 1. "C" grid for NACA 0012 airfoil



b. Close-up of NACA 0012 section

Figure 1. (concluded)

# NACA 0012 UNSTEADY PRESSURE DISTRIBUTION

MACH=0.755 RE=5.5E06 ALPHA=0.016  
(ZERO SUBITERATIONS)

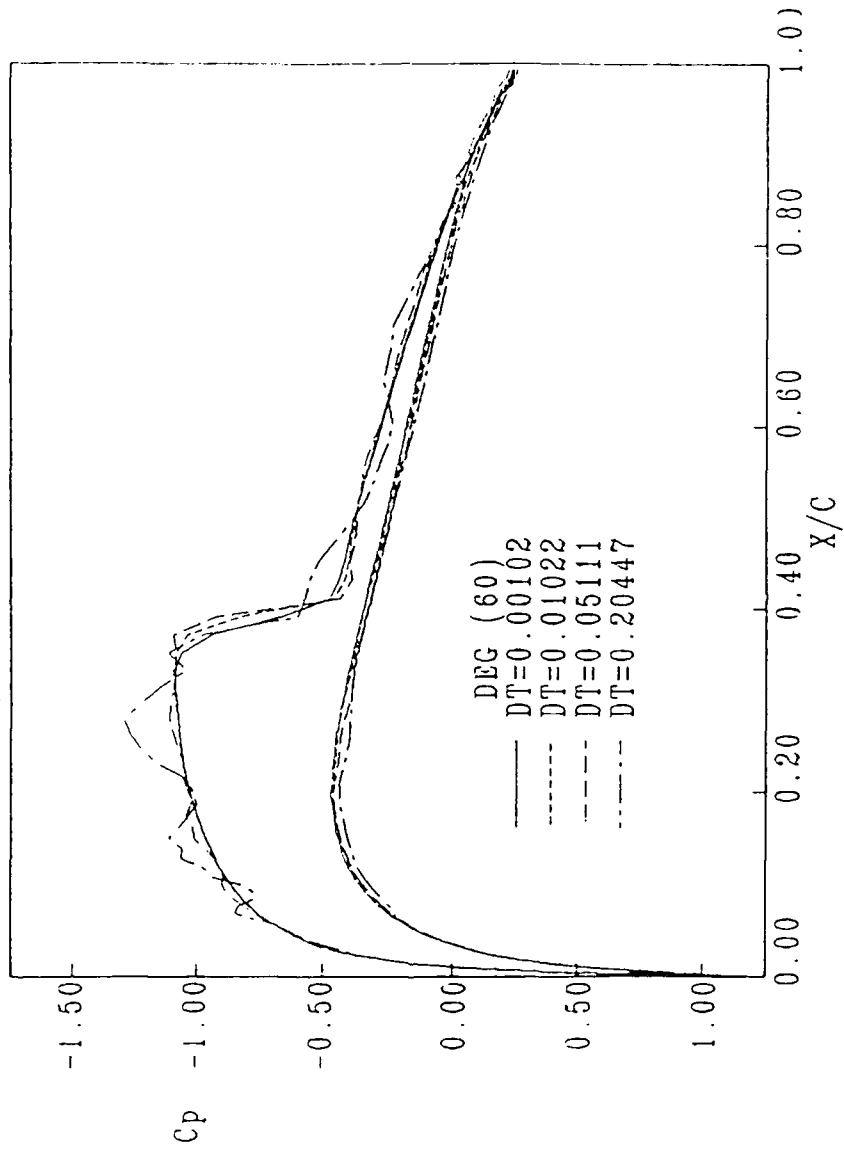


Figure 2. Unsteady pressure distribution for different time step sizes

# NACA 0012 UNSTEADY PRESSURE DISTRIBUTION

MACH=0.755 RE=5.5E06 ALPHA=0.016  
(DT=0.051111)

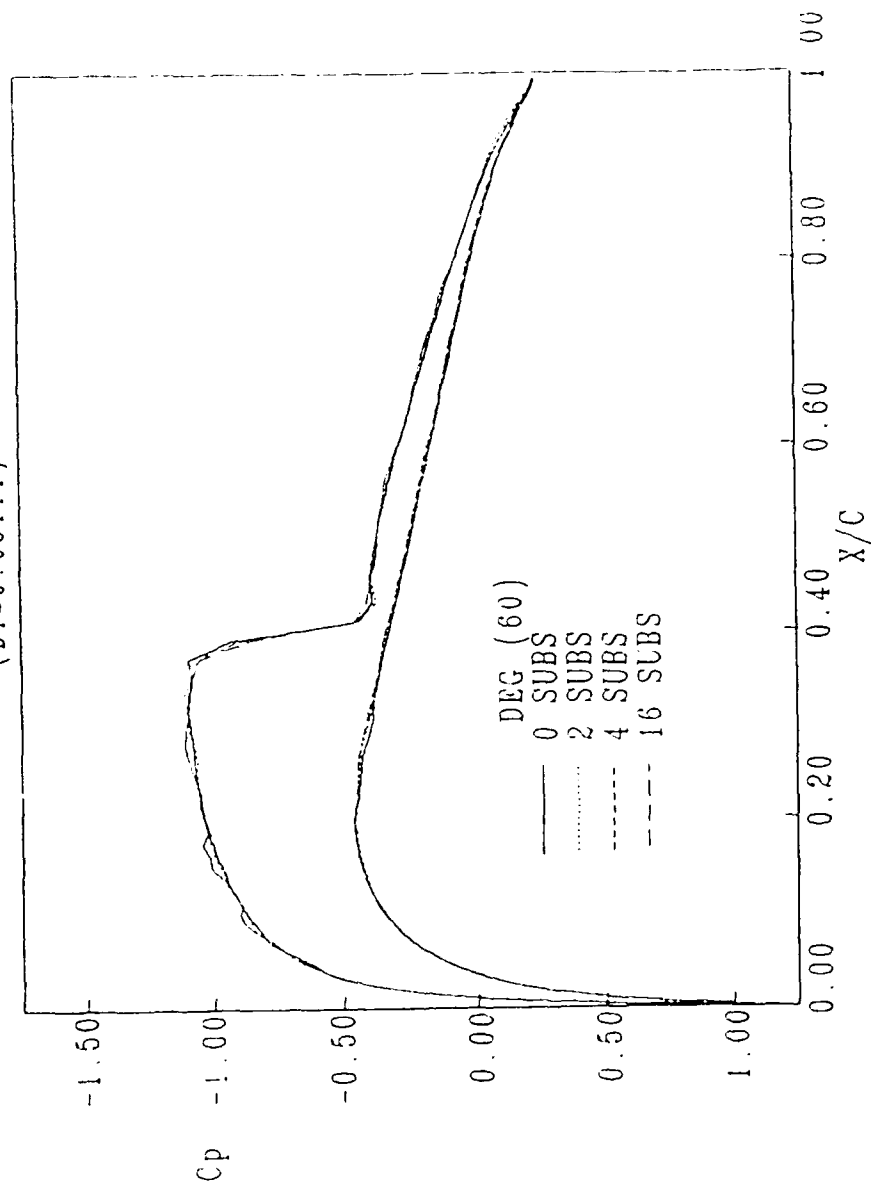


Figure 3. Unsteady pressure distributions using minimum time step subiterations for first 60 degrees of motion DT = .0511

# NACA 0012 UNSTEADY PRESSURE DISTRIBUTION

MACH=0.755 RE=5.5E06 ALPHA=0.016  
(DT=0.2044)

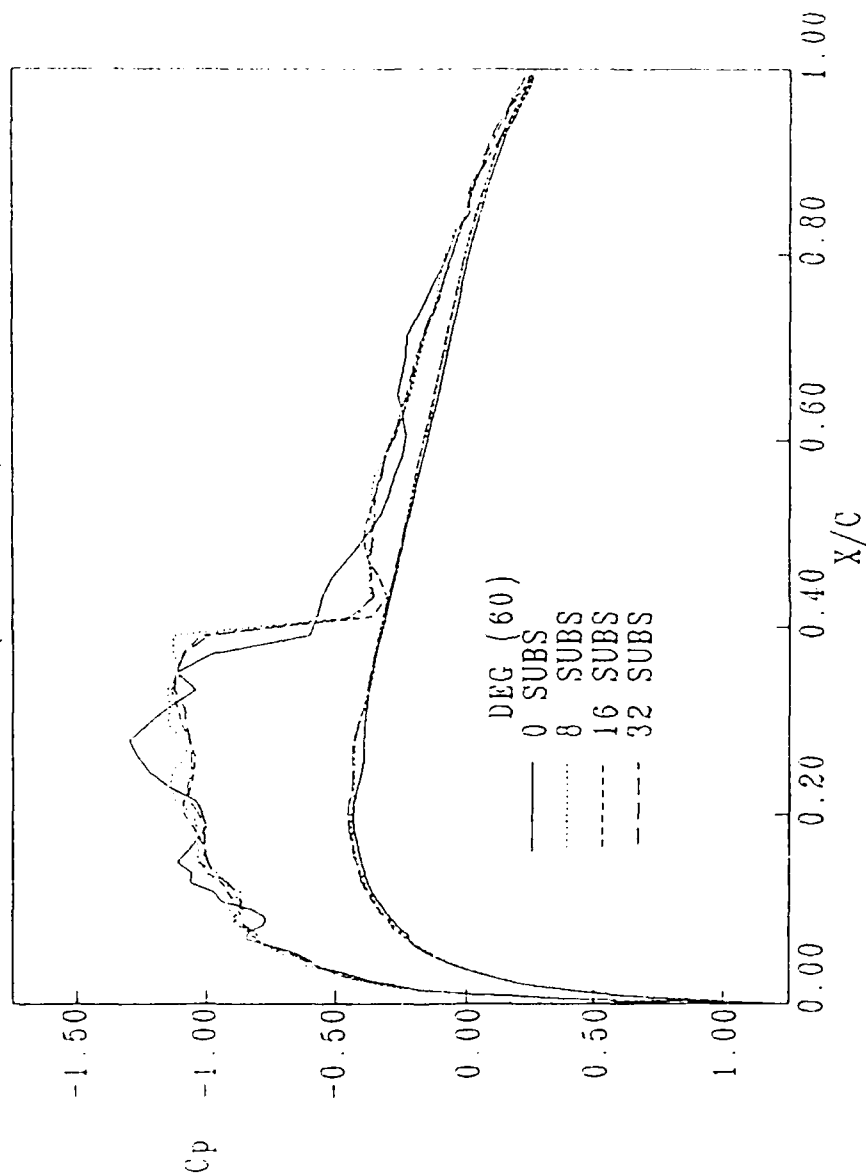


Figure 4. Unsteady pressure distributions using minimum time step subiterations for first 60 degrees of motion DT = .2044

# NACA 0012 UNSTEADY PRESSURE DISTRIBUTION

MACH=0.755 RE=5.5E06 ALPHA=0.016  
(DT=0.05111)

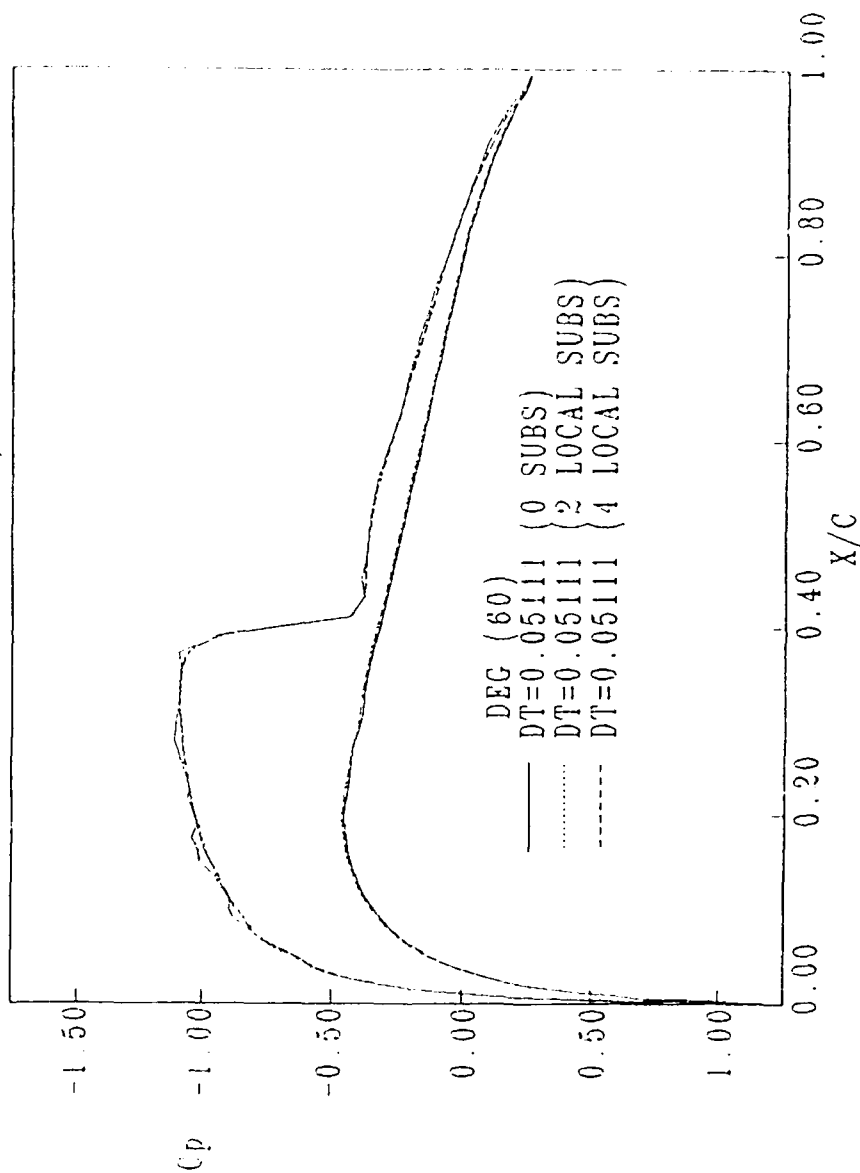


Figure 5. Unsteady pressure distributions using local time step subiterations for first 60 degrees of motion DT = .0511

# NACA 0012 UNSTEADY PRESSURE DISTRIBUTION

MACH=0.755 RE=5.5E06 ALPHA=0.016  
(DT=0.2044)

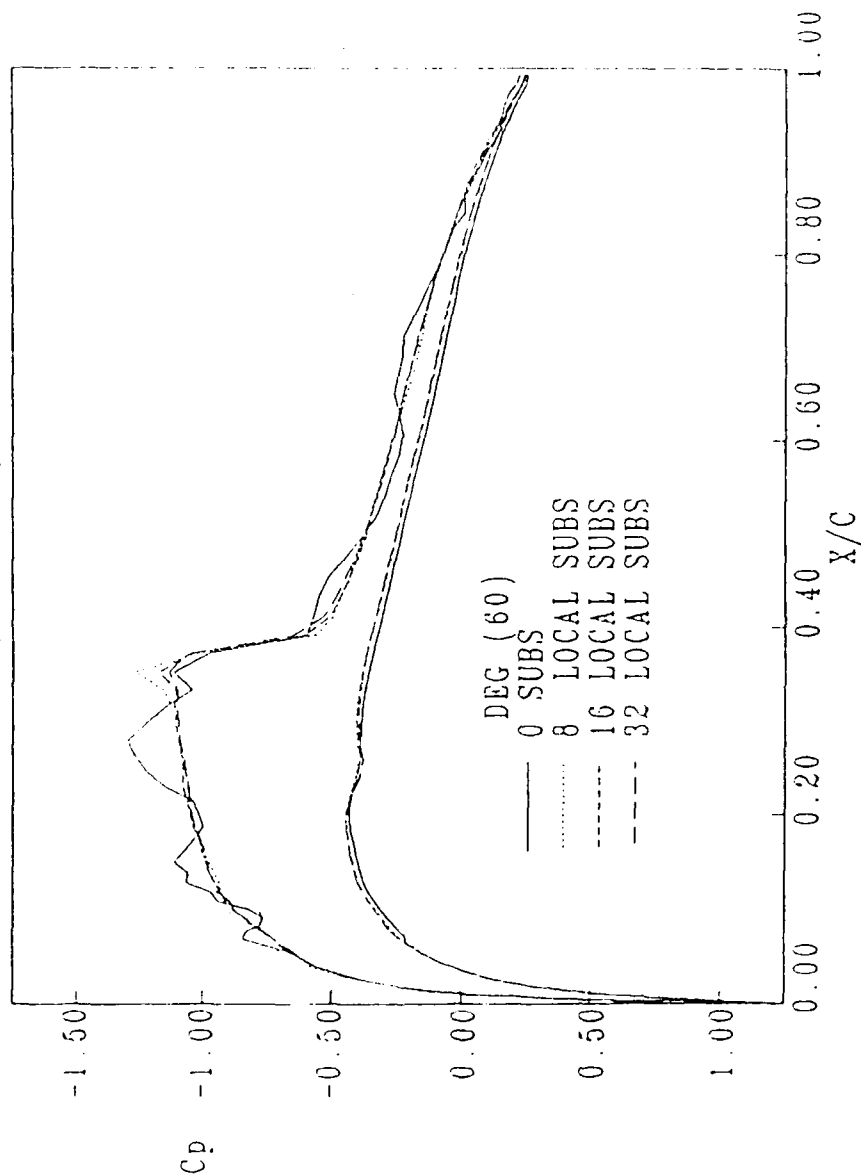


Figure 6. Unsteady pressure distribution using local time step subiterations for first 60 degrees of motion DT = .2044



# NACA 0012 UNSTEADY PRESSURE DISTRIBUTION

MACH=0.755 RE=5.5E06 ALPHA=0.016

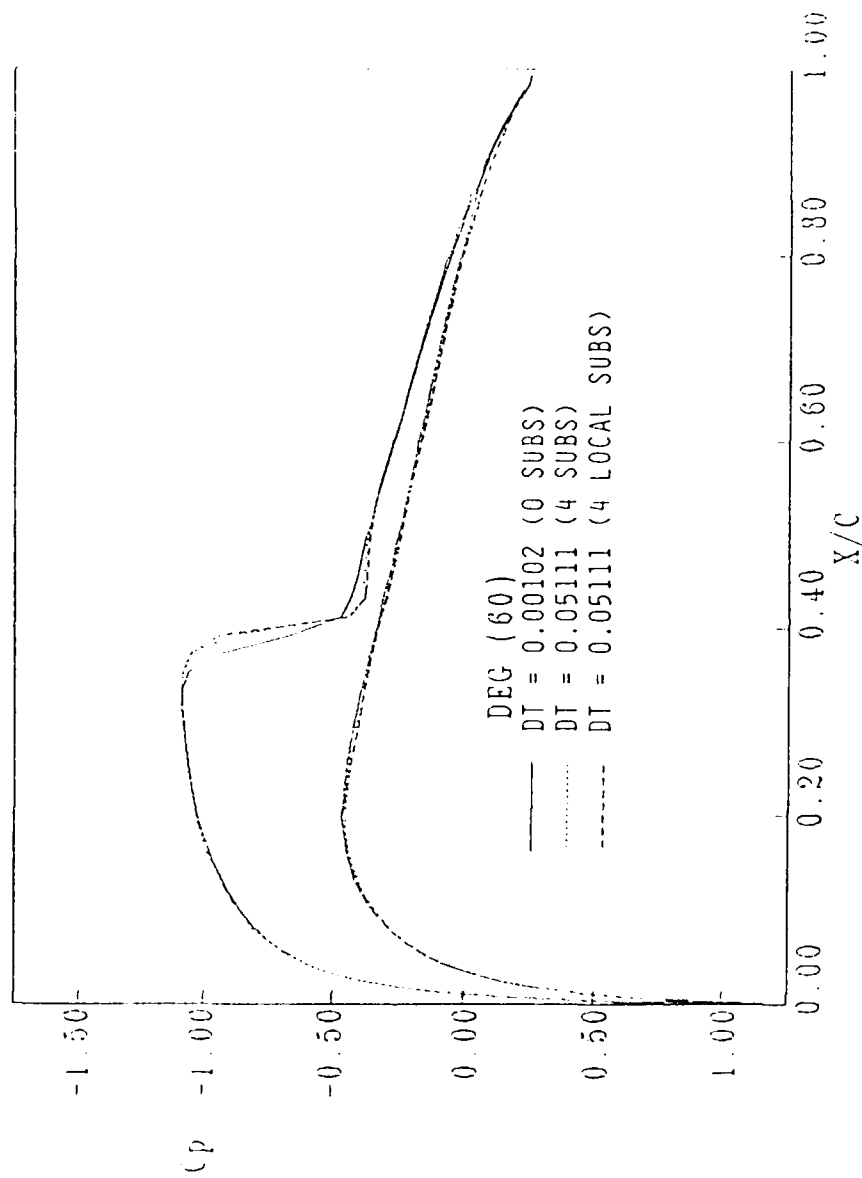


Figure 7. Unsteady pressure distributions using both min and local subiterations for first 60 degrees of motion DT = .0511

# NACA 0012 UNSTEADY PRESSURE DISTRIBUTION

NACH=0.755 RE=5.5E06 ALPHA=0.016  
(16 SUBITERATIONS)

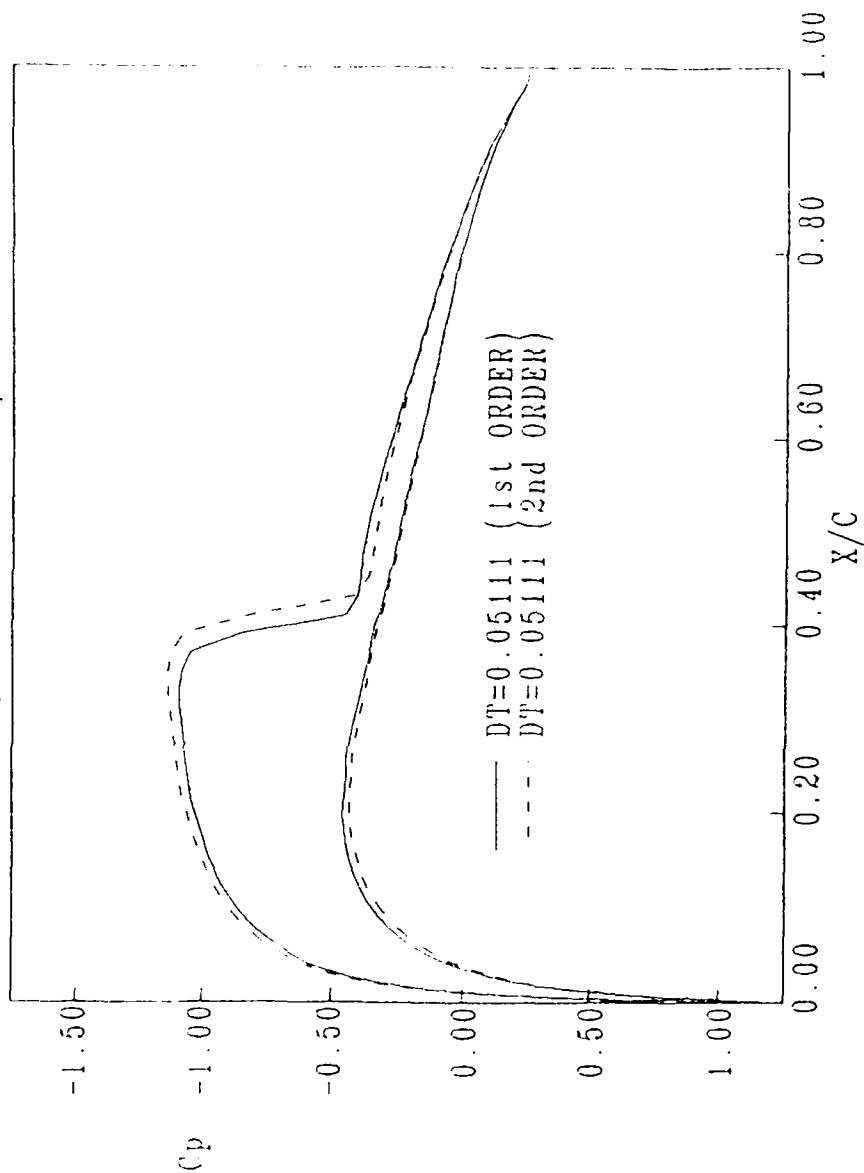


Figure 8. Unsteady pressure distributions using 1st and 2nd order schemes, 16 min time step subiterations

# LAMINAR FLAT PLATE VELOCITY DISTRIBUTION

MACH=0.5 REL=10,000

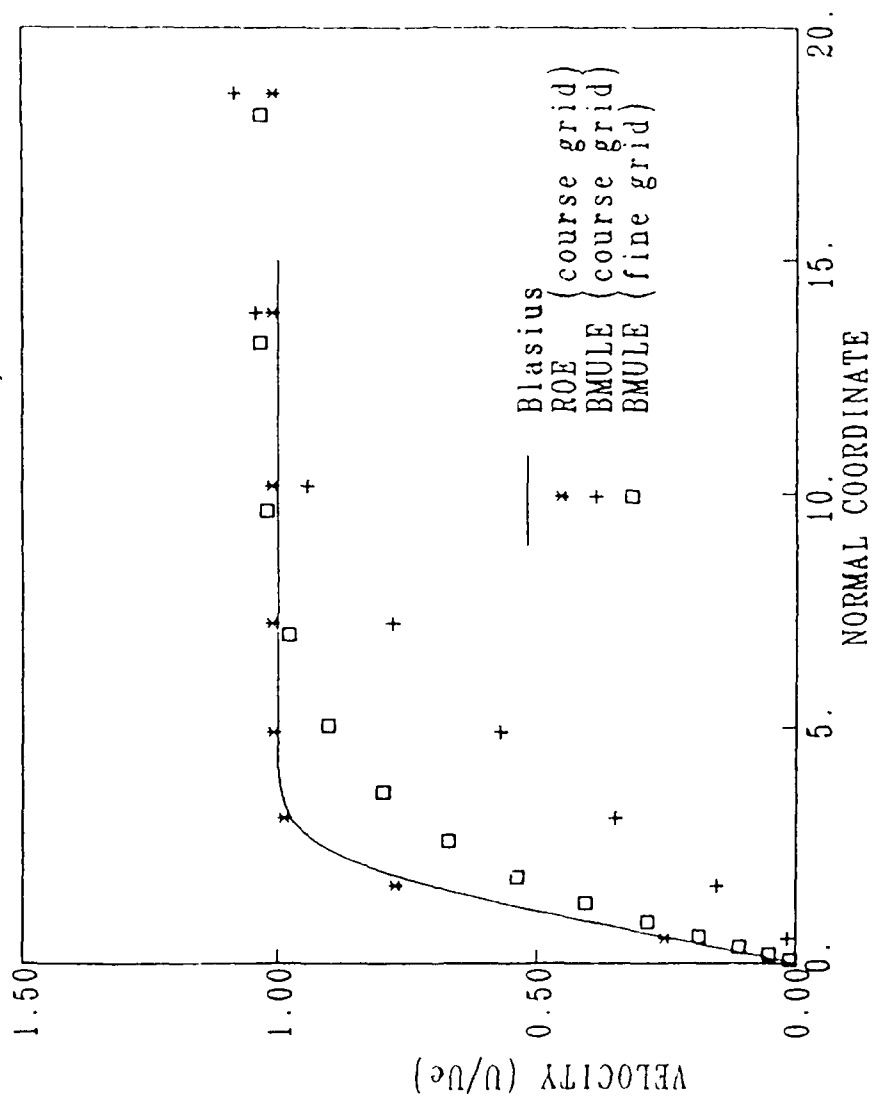


Figure 9. Velocity profiles for laminar flat plate

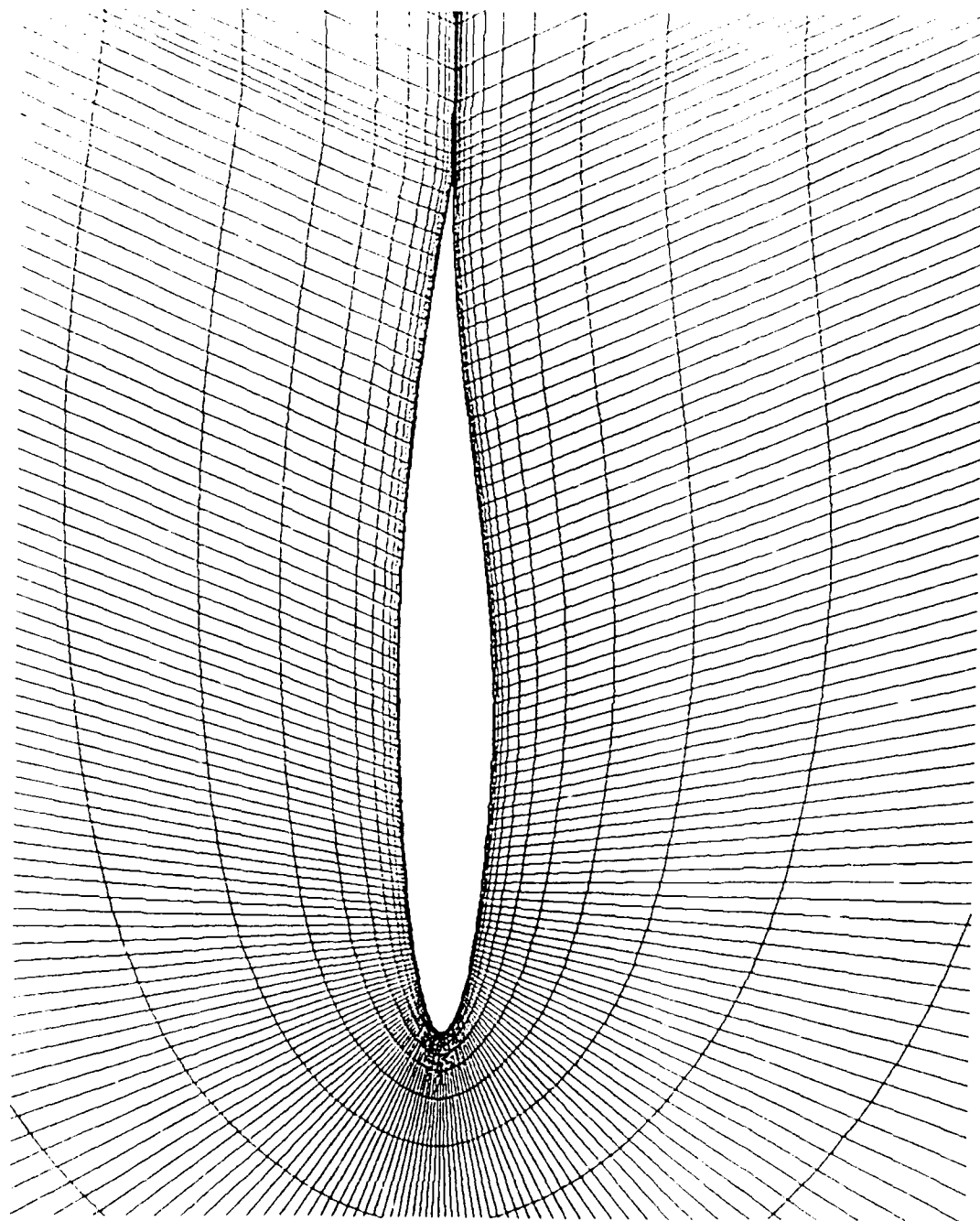
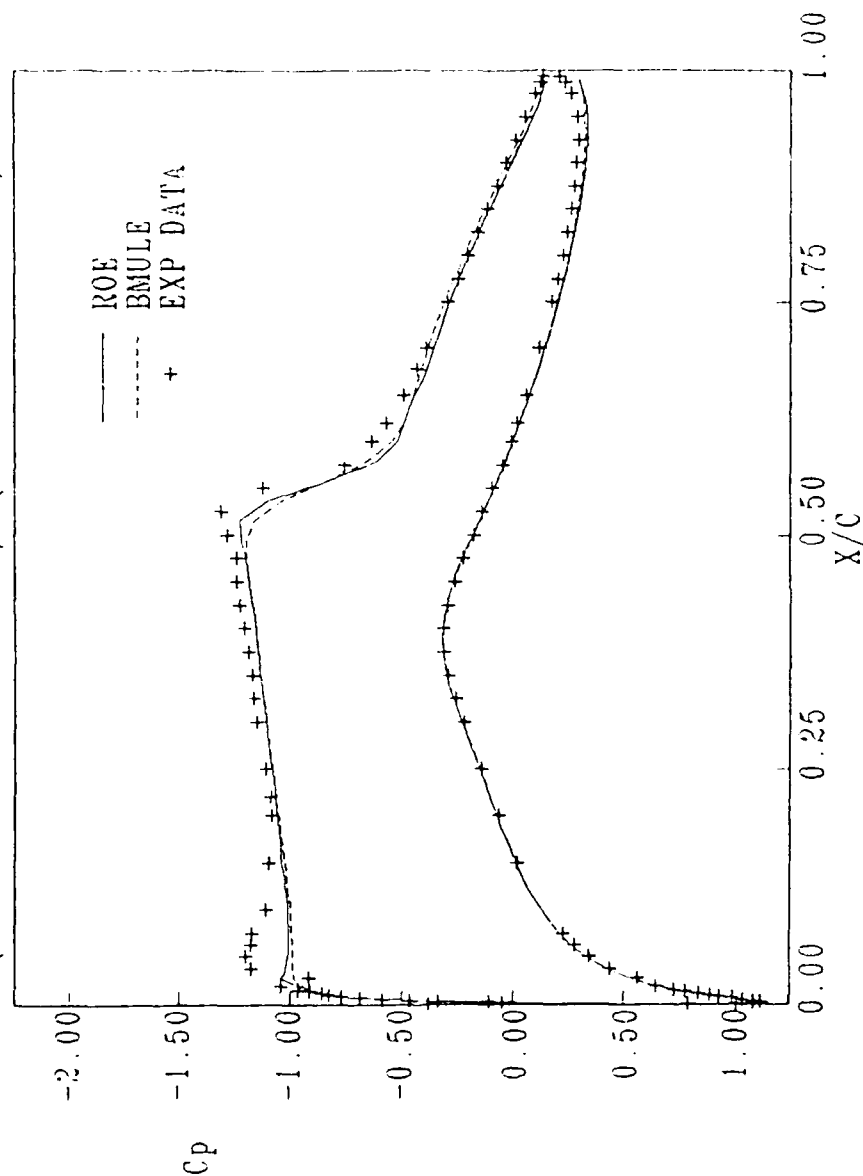


Figure 10. "C" grid for RAE 2822 airfoil (221 x 31 x 2)

# RAE 2822 STEADY PRESSURE DISTRIBUTION

CASE=9 MACH=0.734 RE=6.5E06 ALPHA=2.79  
(ROE - MINMOD 2<sup>nd</sup> ORDER) (BMULE - 2<sup>nd</sup> ORDER)

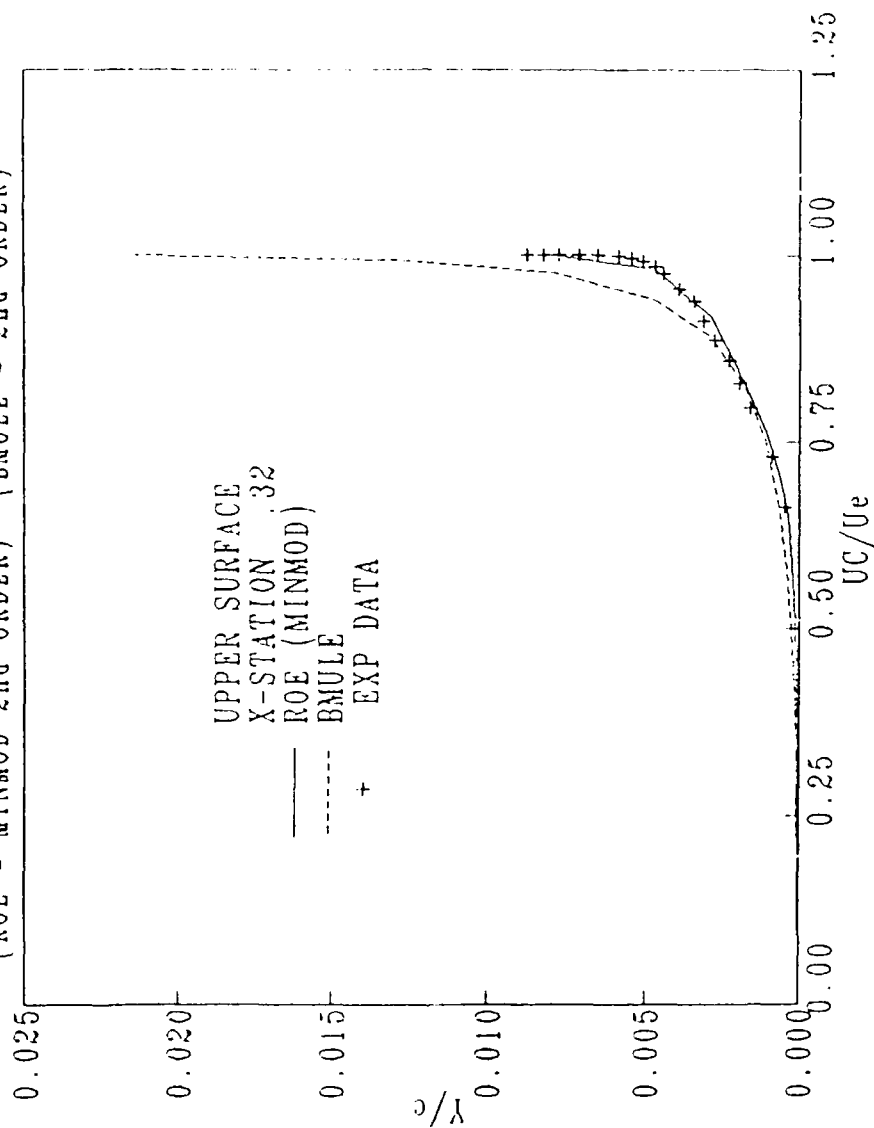


a. Steady pressure distributions

Figure 11. Comparison of minmod 2nd order with BMULE for the RAE 2822

# RAE 2822 BOUNDARY LAYER PROFILE

CASE=9 MACH=0.734 RE=6.5E06 ALPHA=2.79  
(ROE - MINMOD 2nd ORDER) (BMULE - 2nd ORDER)

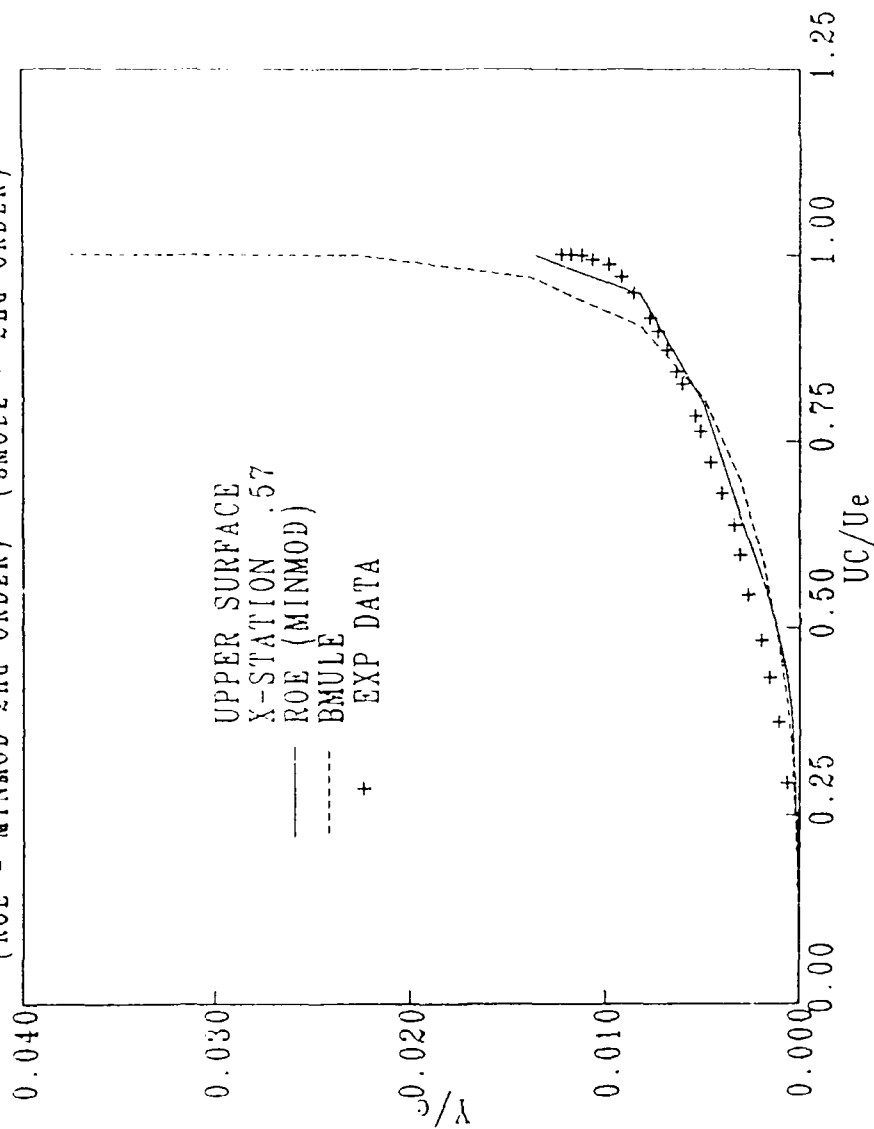


b. Boundary layer velocity profiles at 32% chord (upper surface)

Figure 11. (continued)

# RAE 2822 BOUNDARY LAYER PROFILE

CASE=9 MACH=0.734 RE=6.5E06 ALPHA=2.79  
(ROE - MINMOD 2nd ORDER) (BMULE - 2nd ORDER)

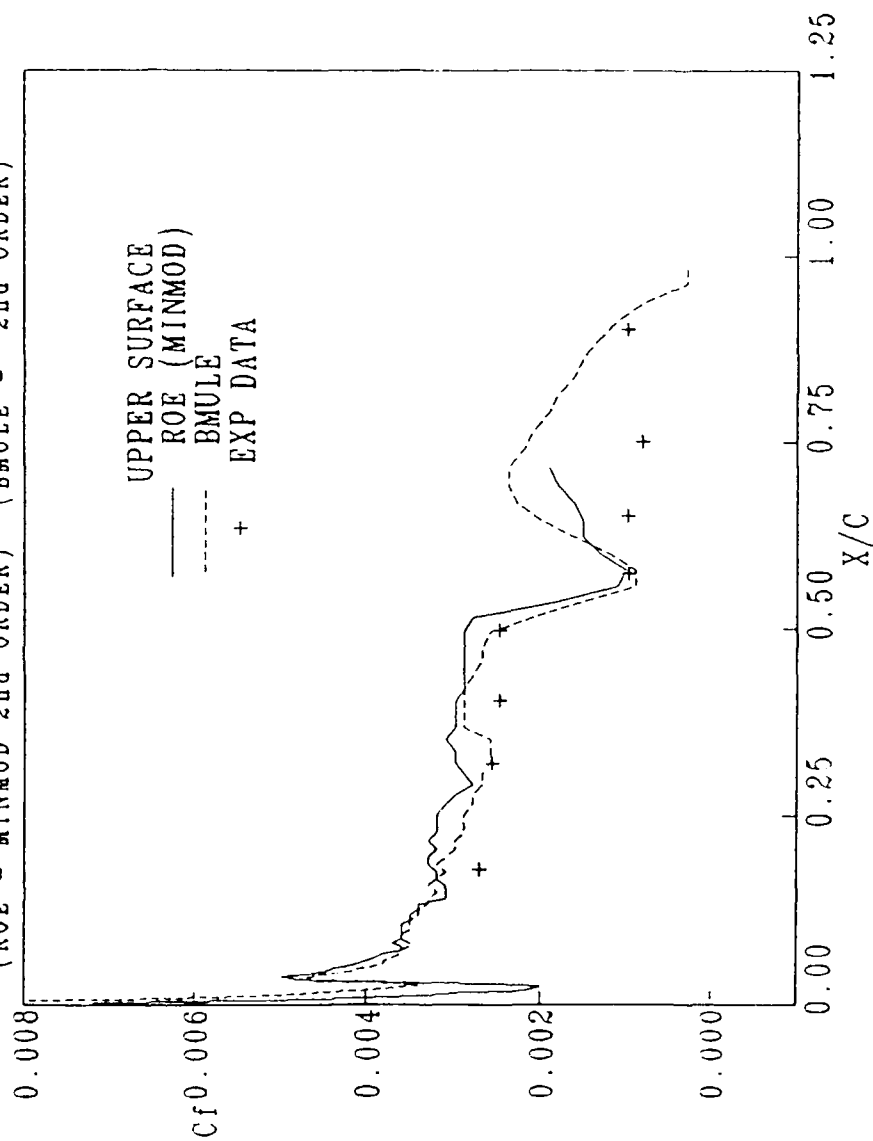


c. Boundary layer velocity profiles at 57% chord (upper surface)

Figure 11. (continued)

# RAE 2822 SKIN FRICTION

CASE=9 MACH=0.734 RE=6.5E06 ALPHA=2.79  
(ROE - MINMOD 2nd ORDER) (BMULE - 2nd ORDER)



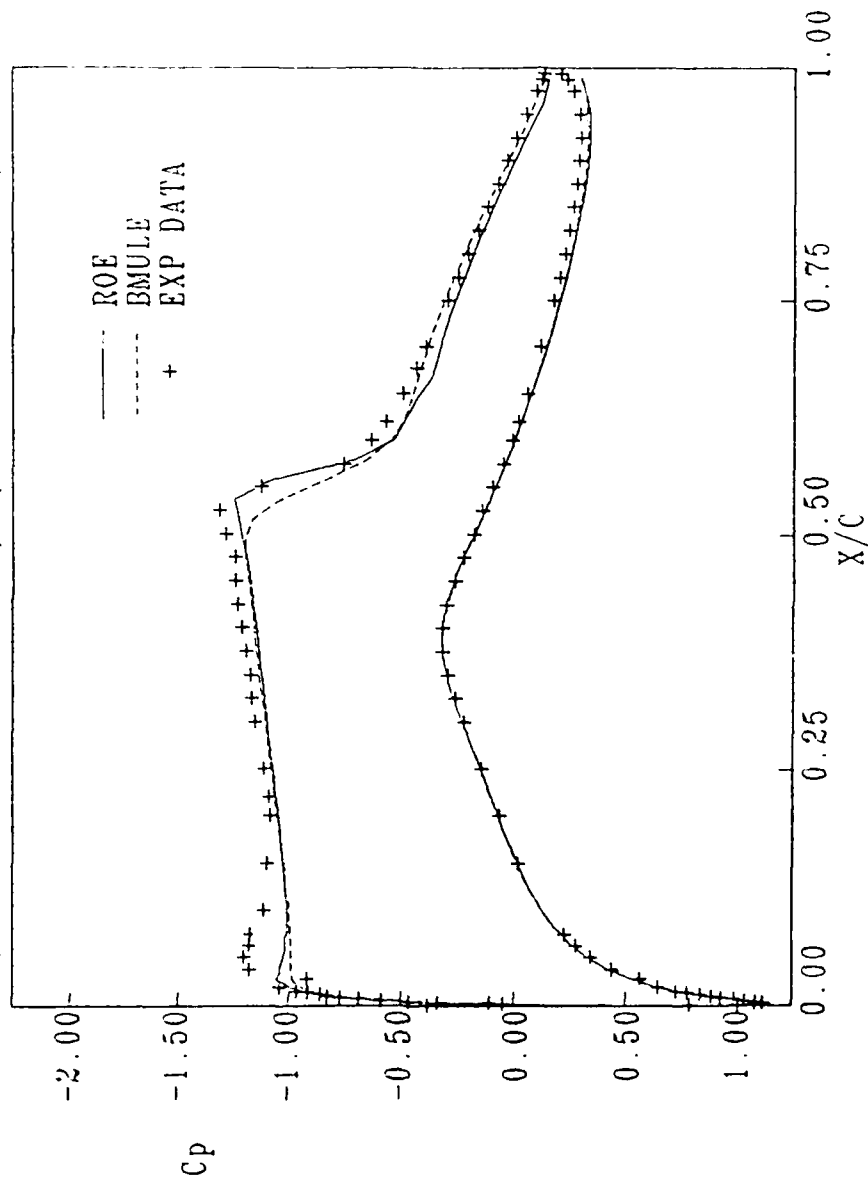
d. Upper surface skin friction

Figure 11. (concluded)



# RAE 2822 STEADY PRESSURE DISTRIBUTION

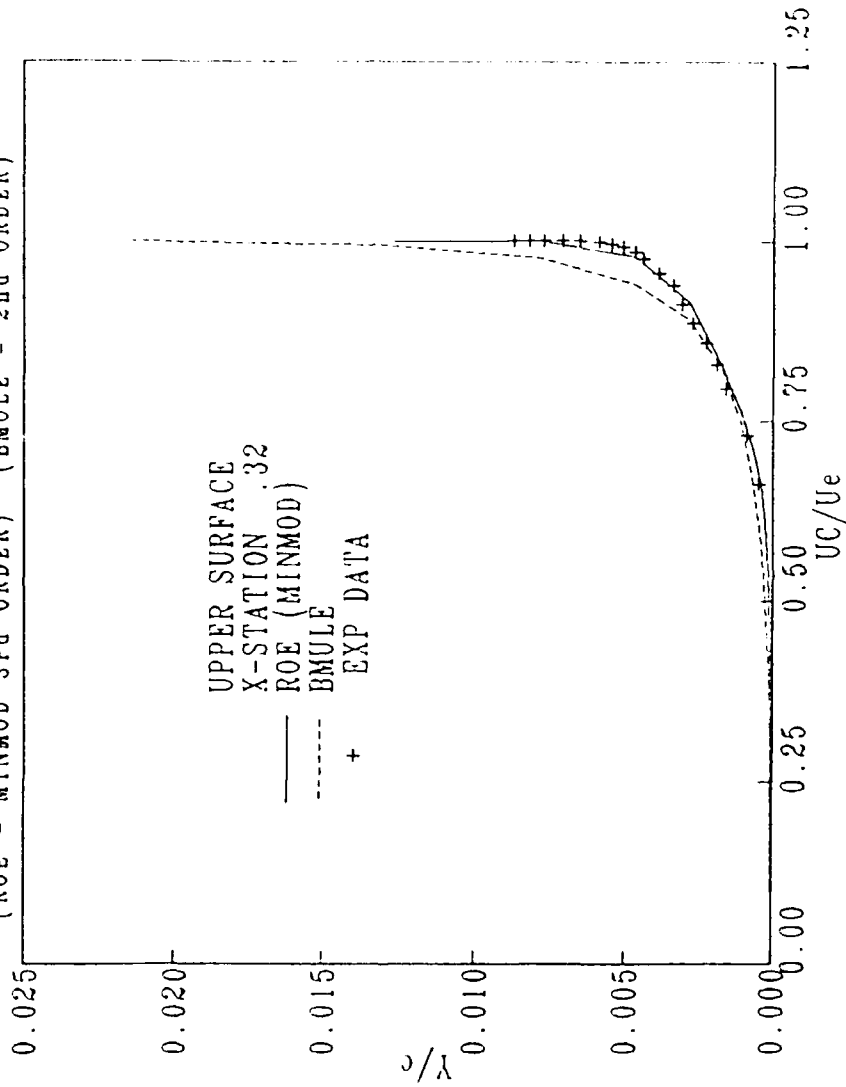
CASE=9 MACH=0.734 RE=5.5E06 ALPHA=2.79  
(ROE - MINMOD 3rd ORDER) (BMULE - 2nd ORDER)



a. Steady pressure distributions

Figure 12. Comparison of minmod 3rd order with BMULE for the RAE 2822

RAE 2822 BOUNDARY LAYER PROFILE  
CASE=9 MACH=0.734 RE=6.5E06 ALPHA=2.79  
(ROE - MINMOD 3rd ORDER) (BMULE - 2nd ORDER)

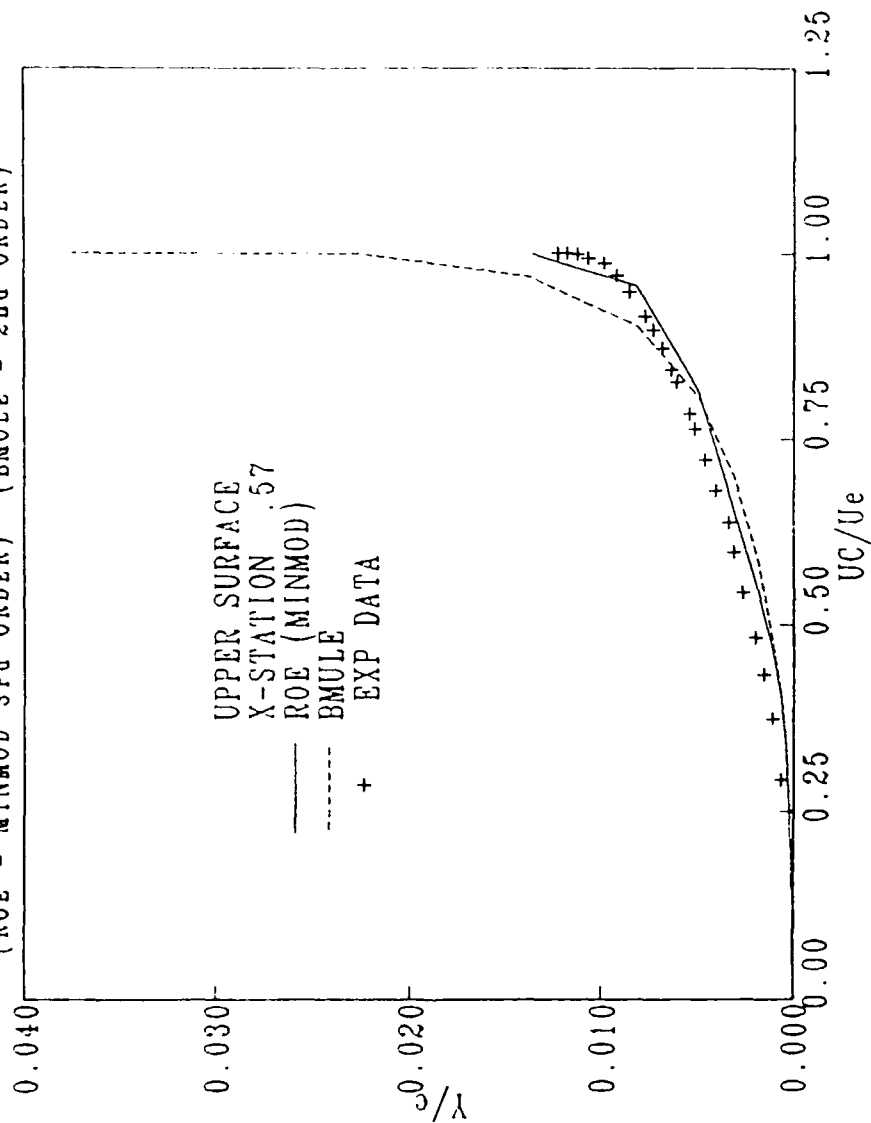


b. Boundary layer velocity profiles at 32% chord (upper surface)

Figure 12. (continued)

# RAE 2822 BOUNDARY LAYER PROFILE

CASE=9 MACH=0.734 RE=6.5E06 ALPHA=2.79  
(ROE - MINMOD 3rd ORDER) (BMULE - 2nd ORDER)

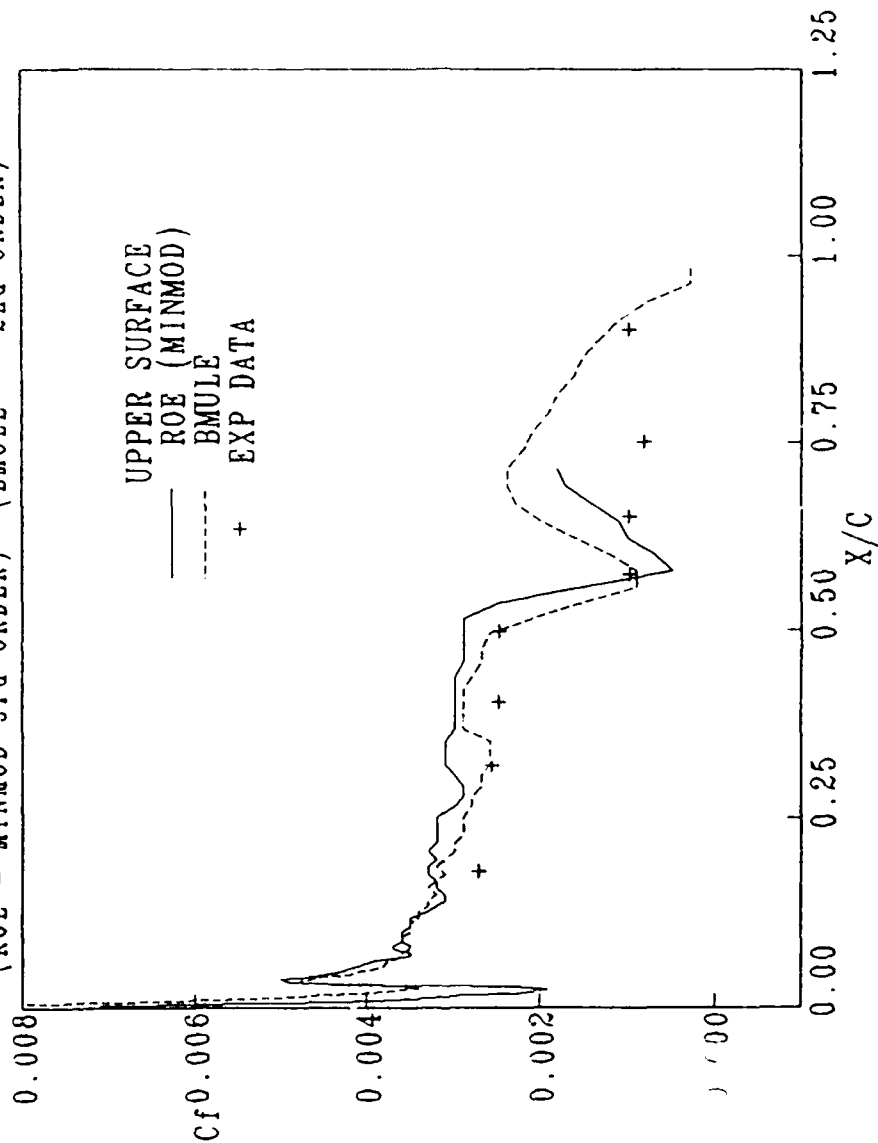


c. Boundary layer velocity profiles at 57% chord (upper surface)

Figure 12. (continued)

# RAE 2822 SKIN FRICTION

CASE=9 MACH=0.734 RE=0.5E06 ALPHA=2.79  
(ROE - MINMOD 3rd ORDER) (DMULE - 2nd ORDER)

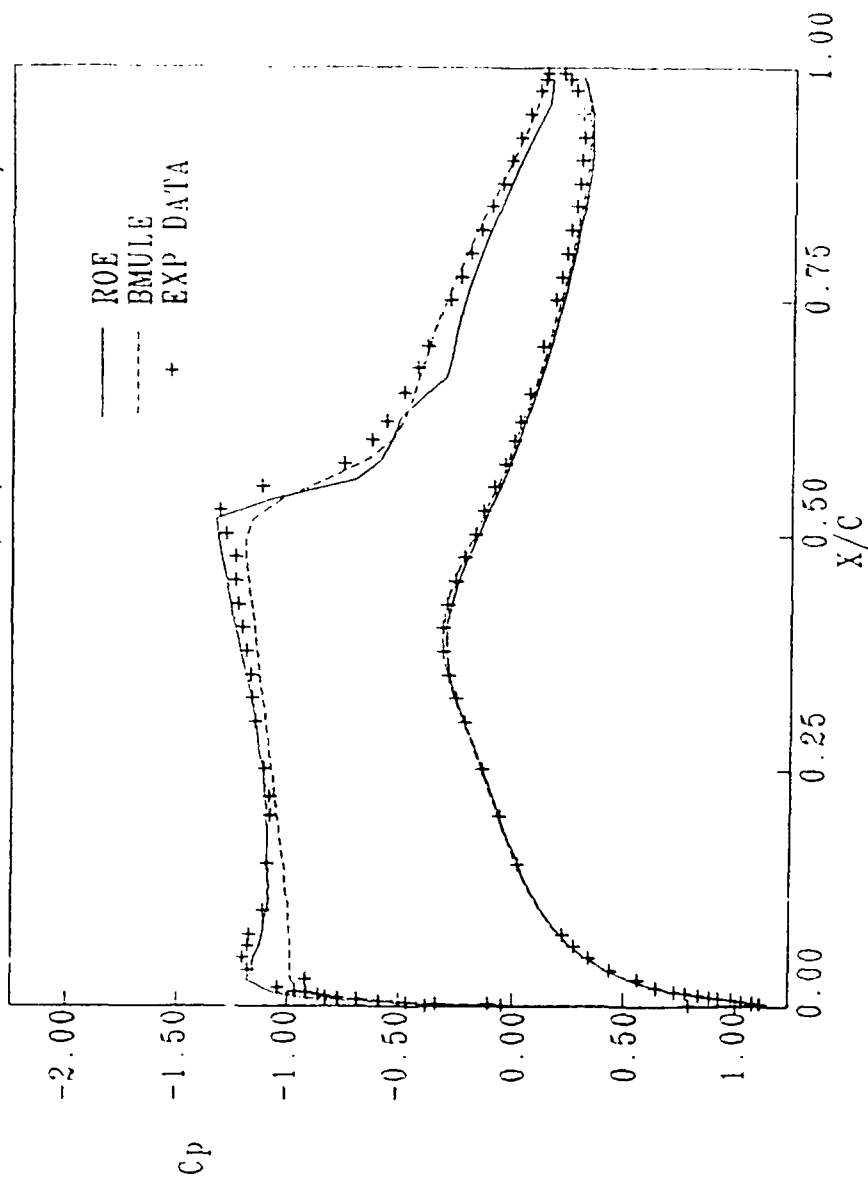


d. Upper surface skin friction

Figure 12. (concluded)

# RAE 2822 STEADY PRESSURE DISTRIBUTION

CASE=9 MACH=0.734 RE=6.5E06 ALPHA=2.79  
(ROE - SUPERBEE 2nd ORDER) (BMULE - 2nd ORDER)

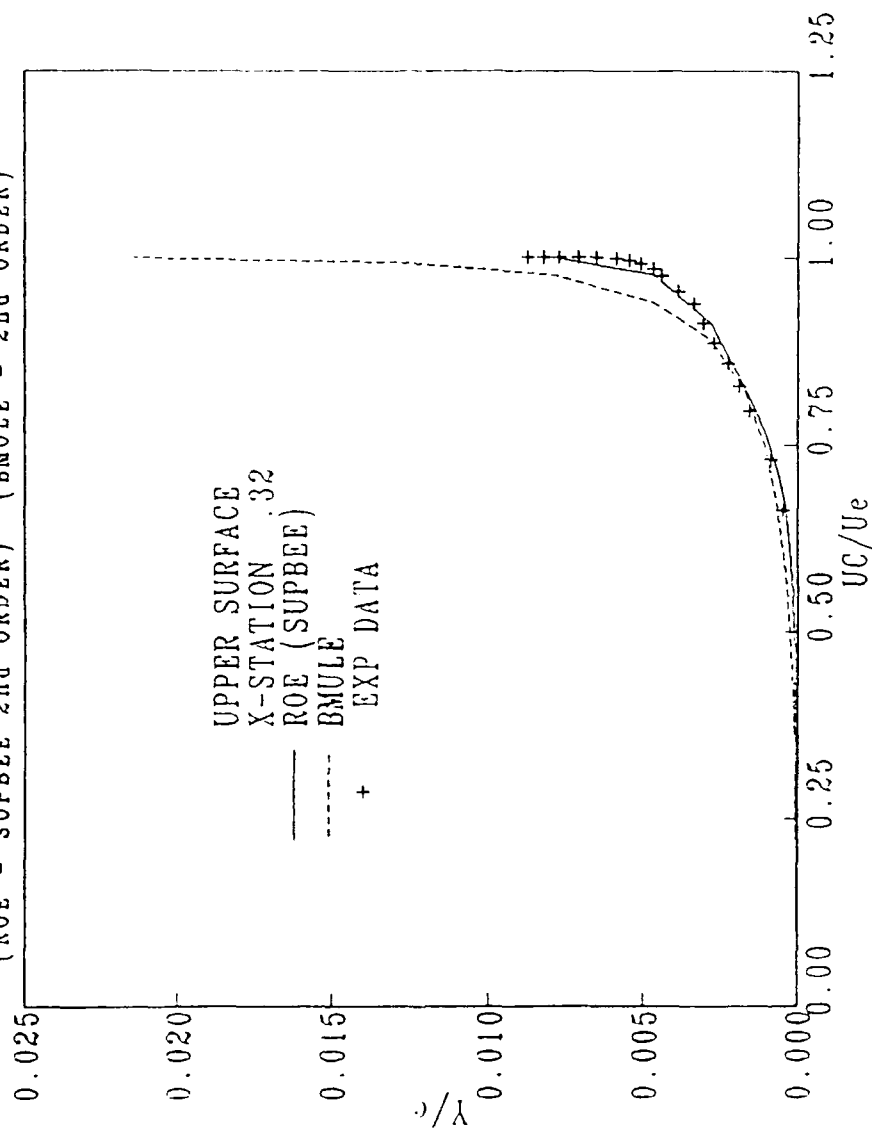


a. Steady pressure distributions

Figure 13. Comparison of superbree 2nd order with BMULE for the RAE 2822

# RAE 2822 BOUNDARY LAYER PROFILE

CASE=9 MACH=0.734 RE=6.5E06 ALPHA=2.79  
(ROE - SUPBEE 2nd ORDER) (BMULE - 2nd ORDER)

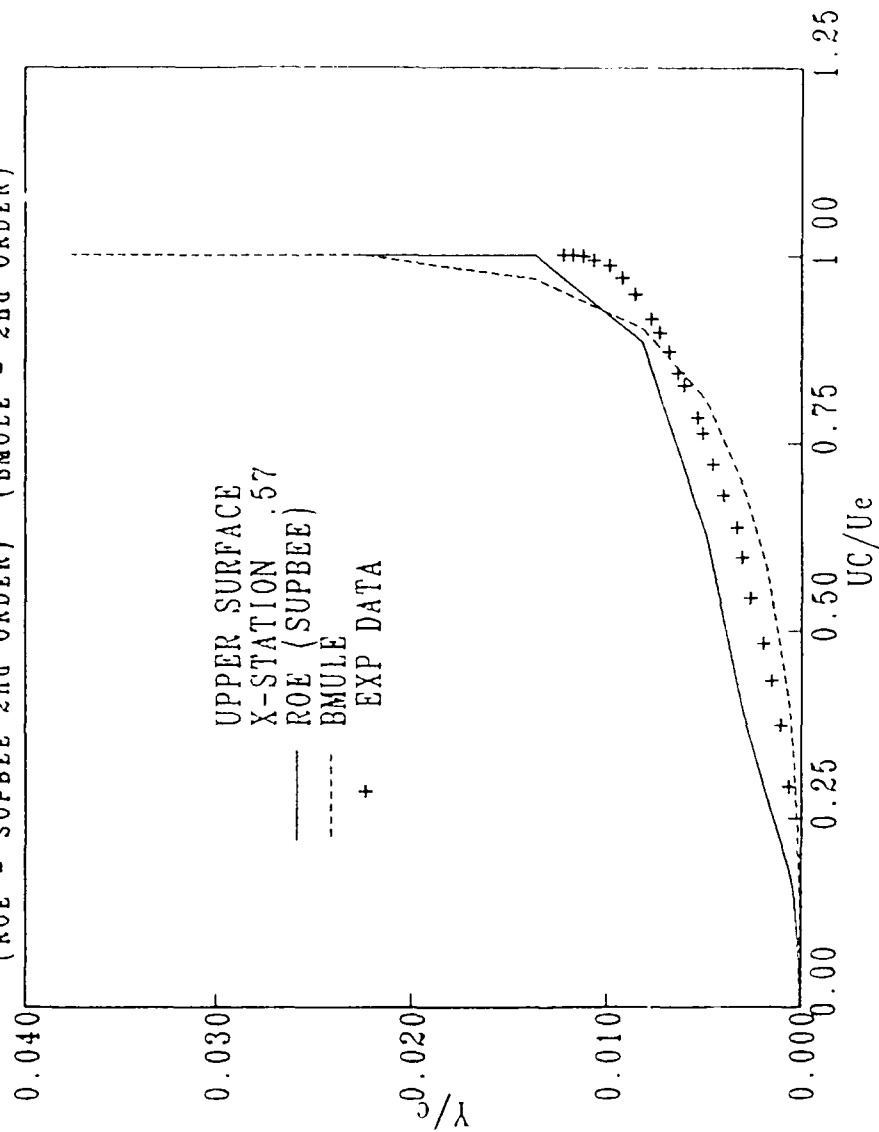


b. Boundary layer velocity profiles at 32% chord (upper surface)

Figure 13. (continued)

# RAE 2822 BOUNDARY LAYER PROFILE

CASE=9 MACH=0.734 RE=6.5E06 ALPHA=2.79  
(ROE - SUPBEE 2nd ORDER) (BMULE - 2nd ORDER)

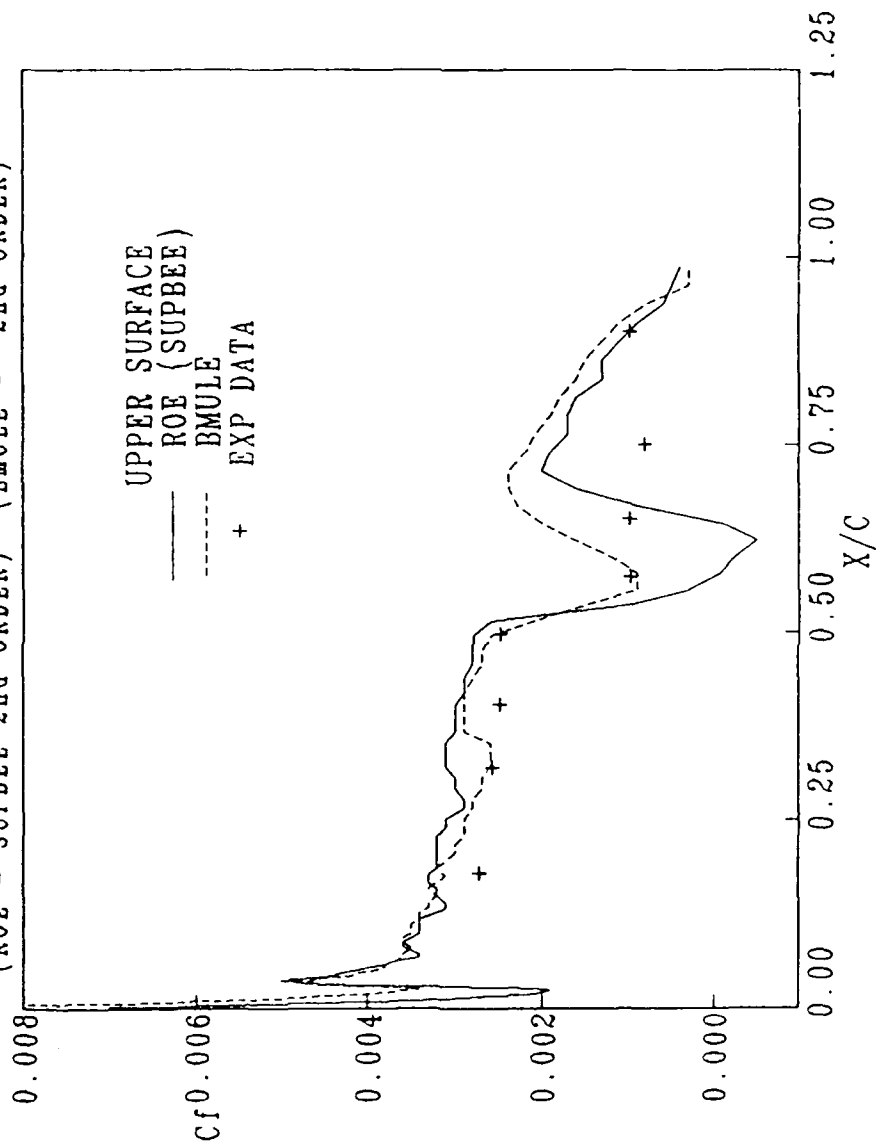


c. Boundary layer velocity profiles at 57% chord (upper surface)

Figure 13. (continued)

# RAE 2822 SKIN FRICTION

CASE=9 MACH=0.734 RE=6.5E06 ALPHA=2.79  
(ROE - SUPBEE 2nd ORDER) (BMULE - 2nd ORDER)



d. Upper surface skin friction

Figure 13. (concluded)



# RAE 2822 CONVERGENCE HISTORY

CASE=9 MACH=0.734 RE=6.5E06 ALPHA=2.79

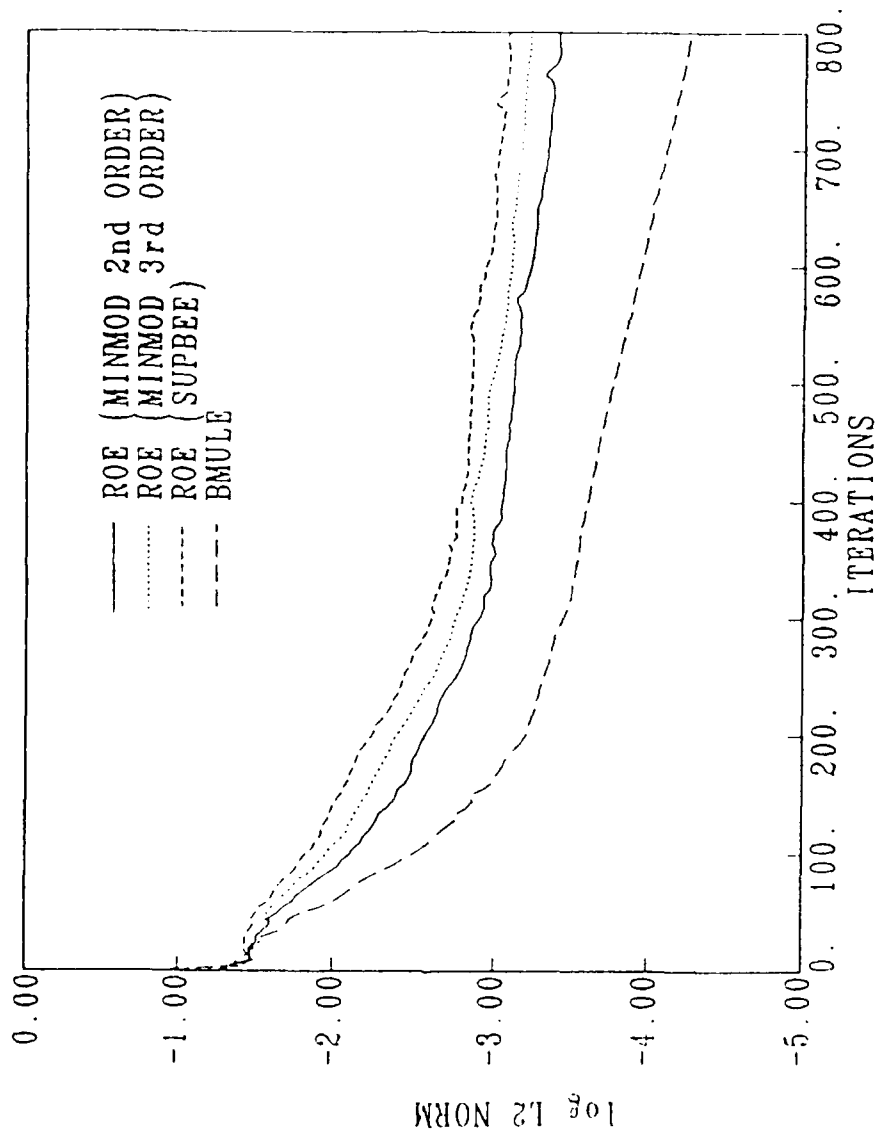
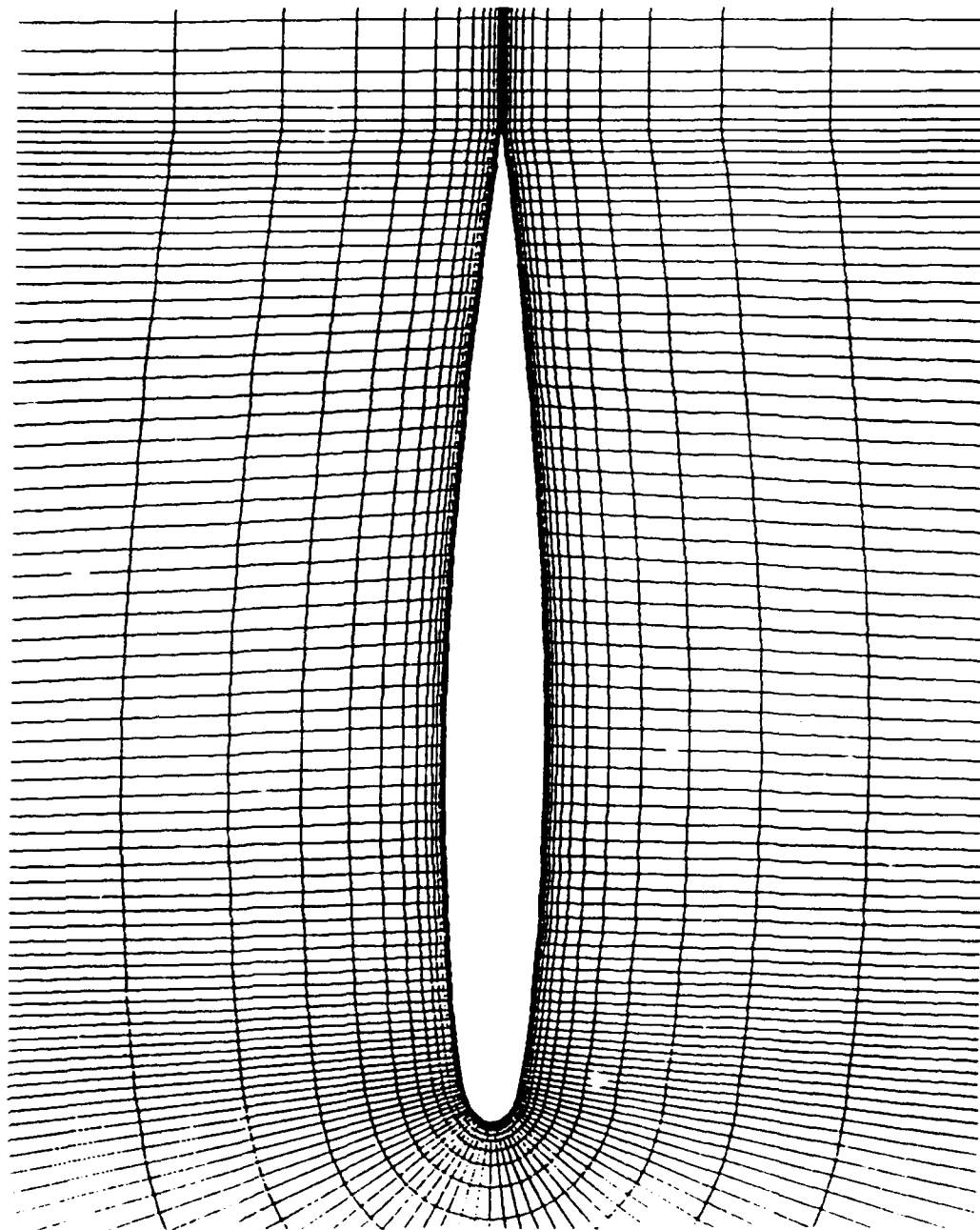
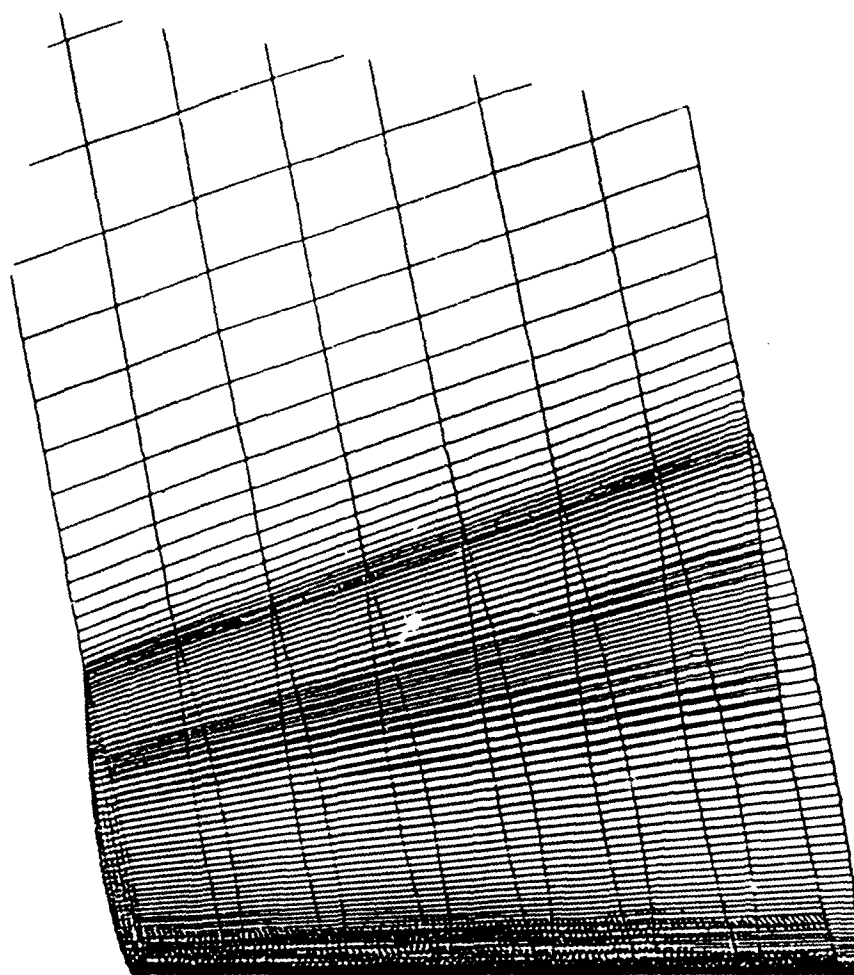


Figure 14. Convergence histories for Roe and BMULE schemes

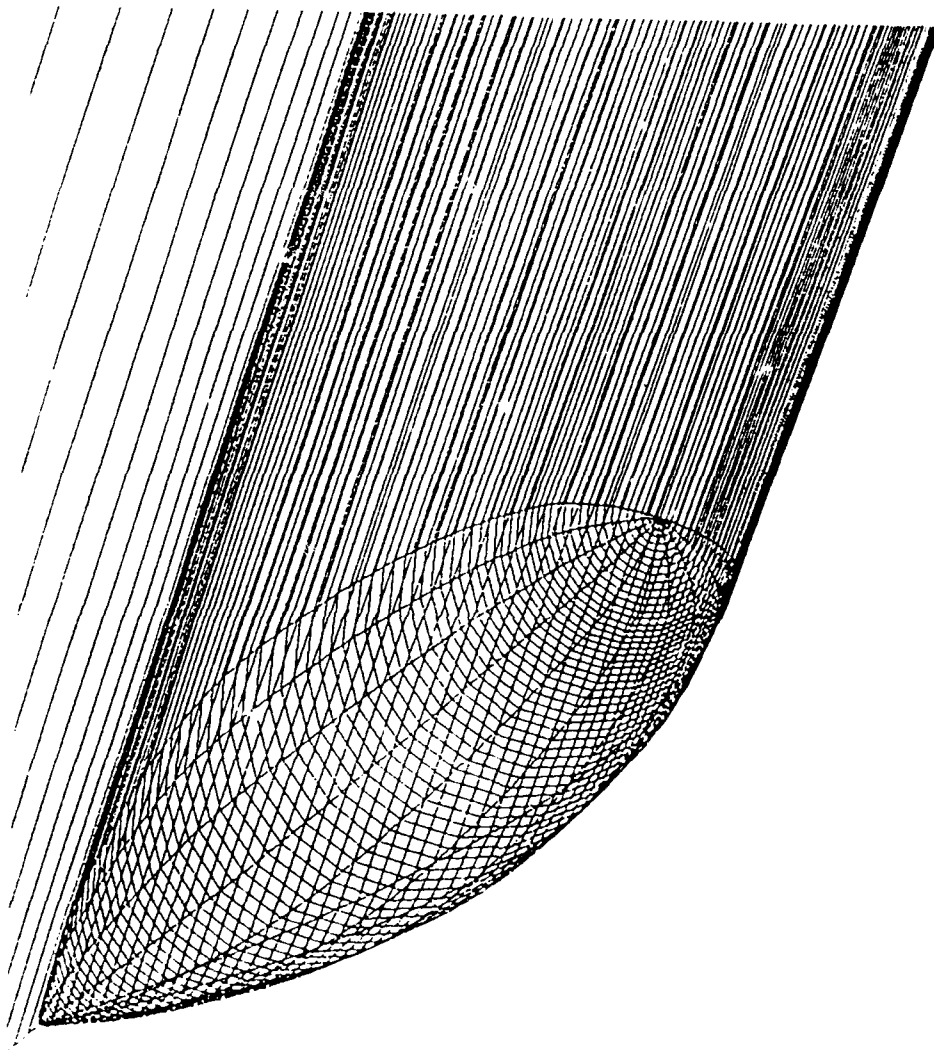


a. 111 points in the streamwise direction, 40 points in the normal direction

Figure 15. "C-0" wing grid for the ONERA M6 wing



b. Distribution of constant spanwise location planes along the wing  
Figure 15. (continued)

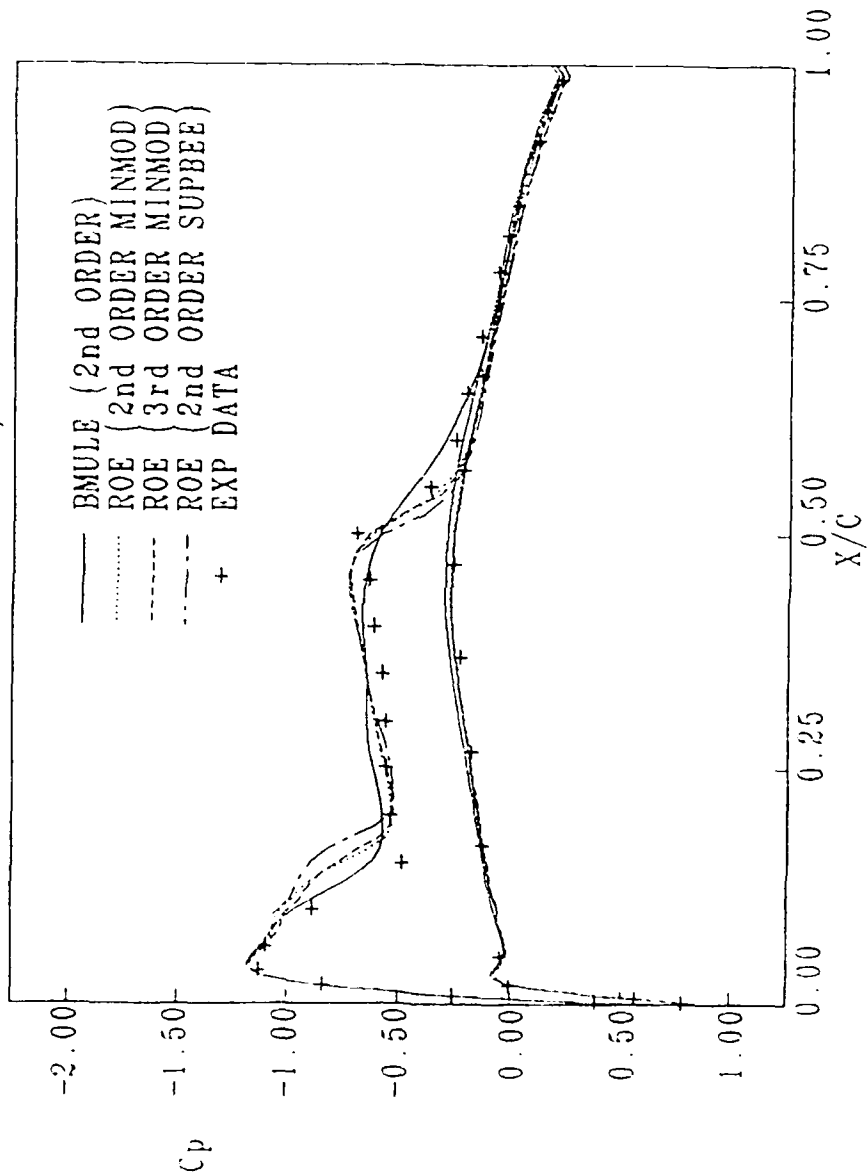


c. ONERA M6 wing tip model

Figure 15. (concluded)

# ONERA M-6 WING STEADY PRESSURE DISTRIBUTION

MACH=0.84 RE=2.6E06 ALPHA=3.06 WING STATION=2  
( BMULE vs ROE )

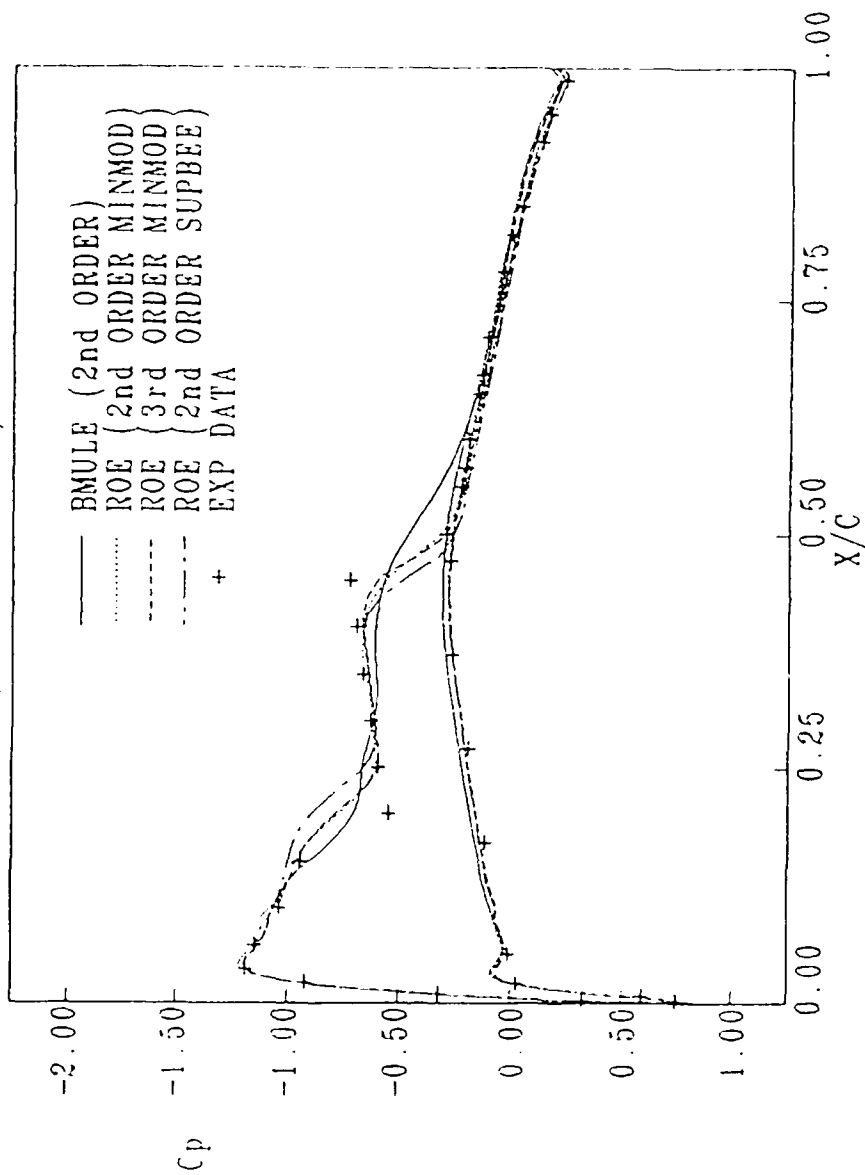


a. 44% semispan location

Figure 16. Steady pressure distributions for ONERA M6 wing comparing Roe and BMULE schemes

# ONERA M-6 WING STEADY PRESSURE DISTRIBUTION

MACH=0.84 RE=2.6E06 ALPHA=3.06 WING STATION=3  
( BMULE vs ROE )

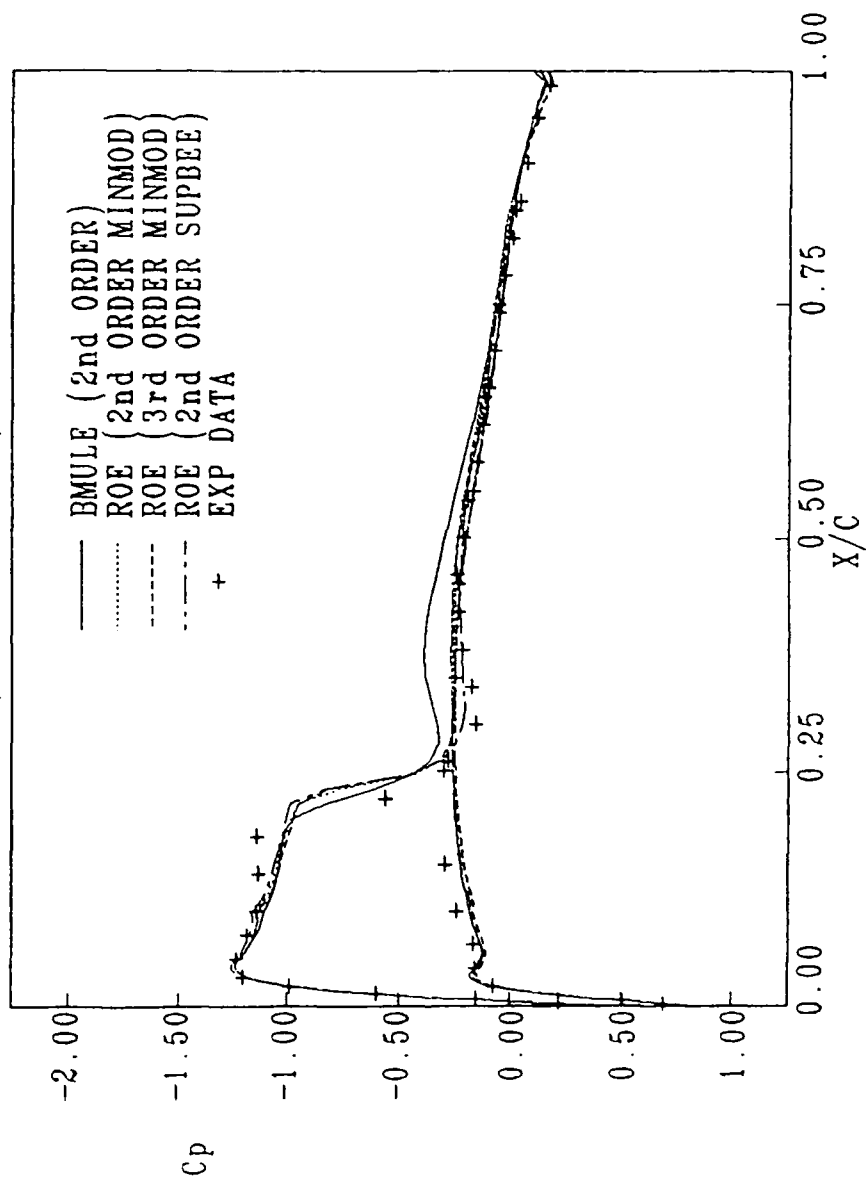


b. 65% semispan location

Figure 16. (continued)

# ONERA M-6 WING STEADY PRESSURE DISTRIBUTION

MACH=0.84 RE=2.0E06 ALPHA=3.06 WING STATION=6  
( BMULE vs ROE )



c. 95% semispan location

Figure 16. (concluded)

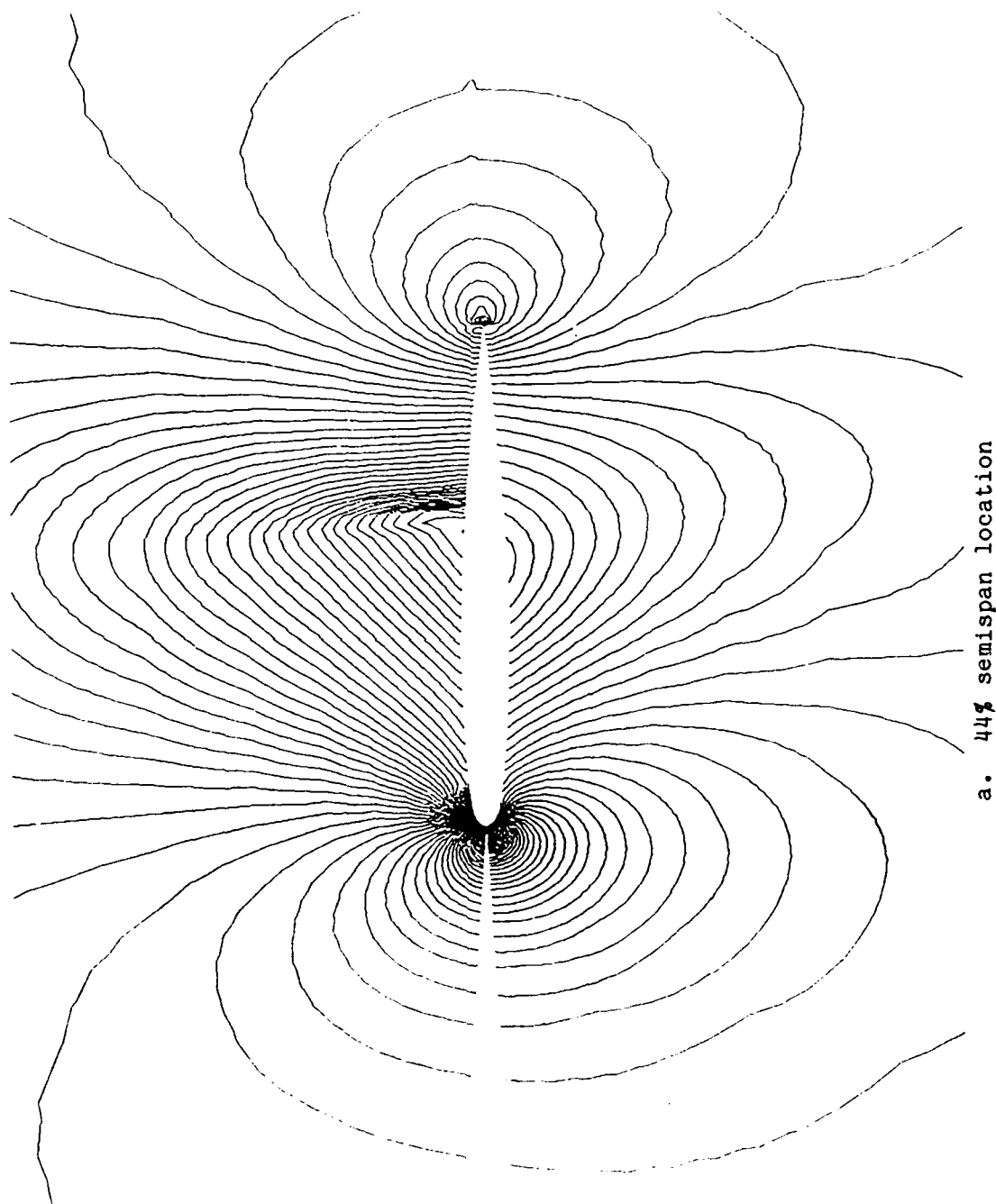
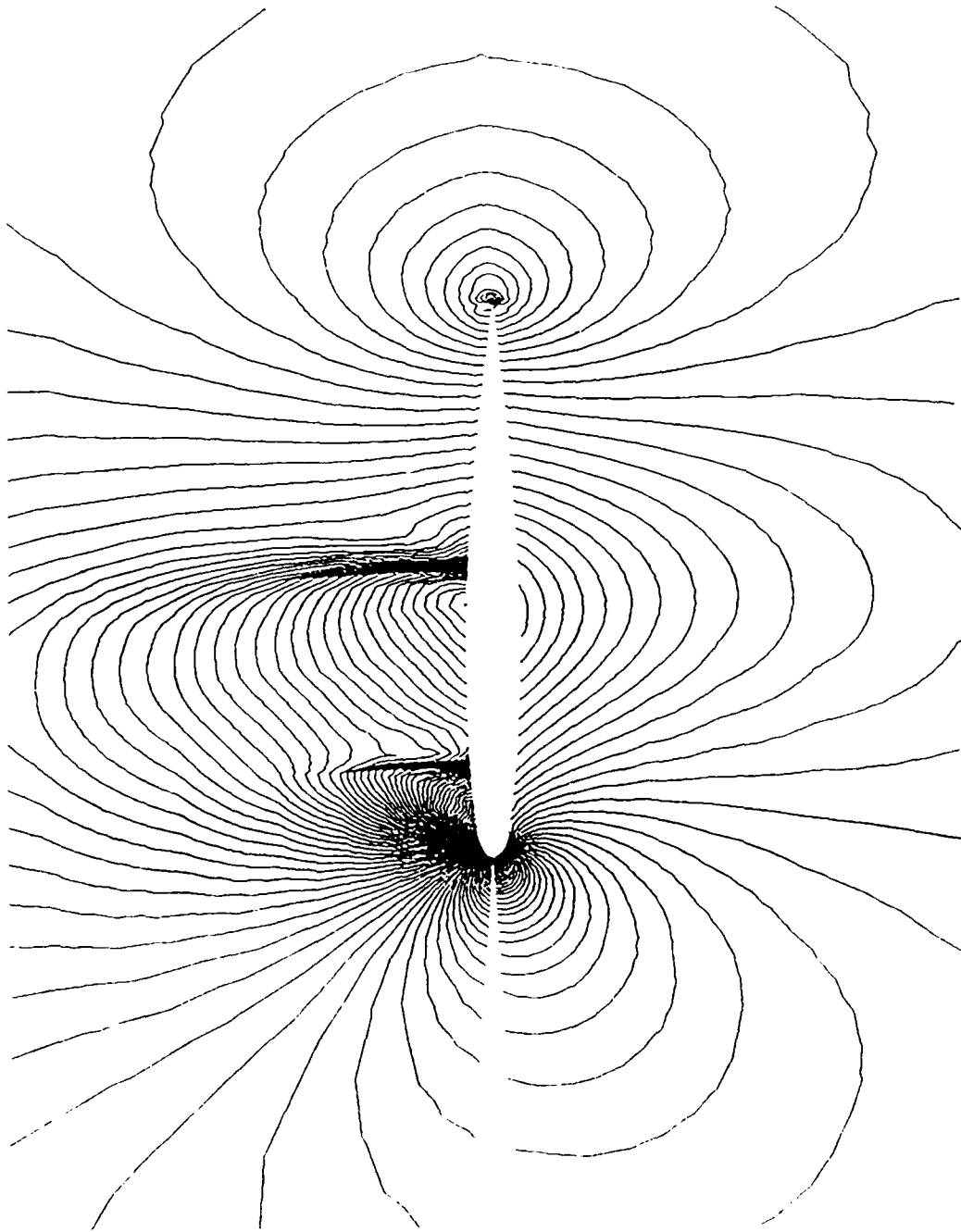


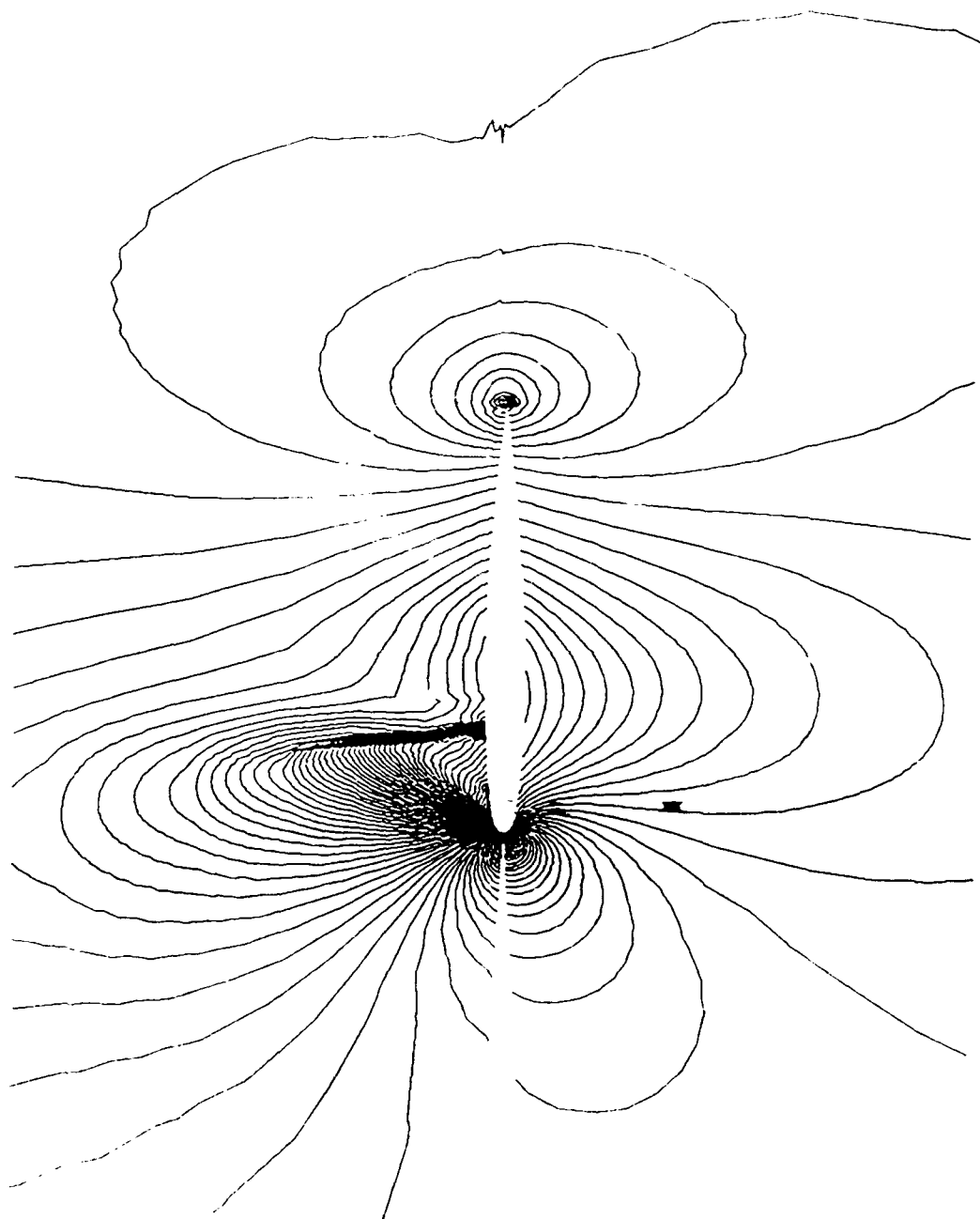
Figure 17. Pressure contours for ONERA M6 wing using minmod 3rd





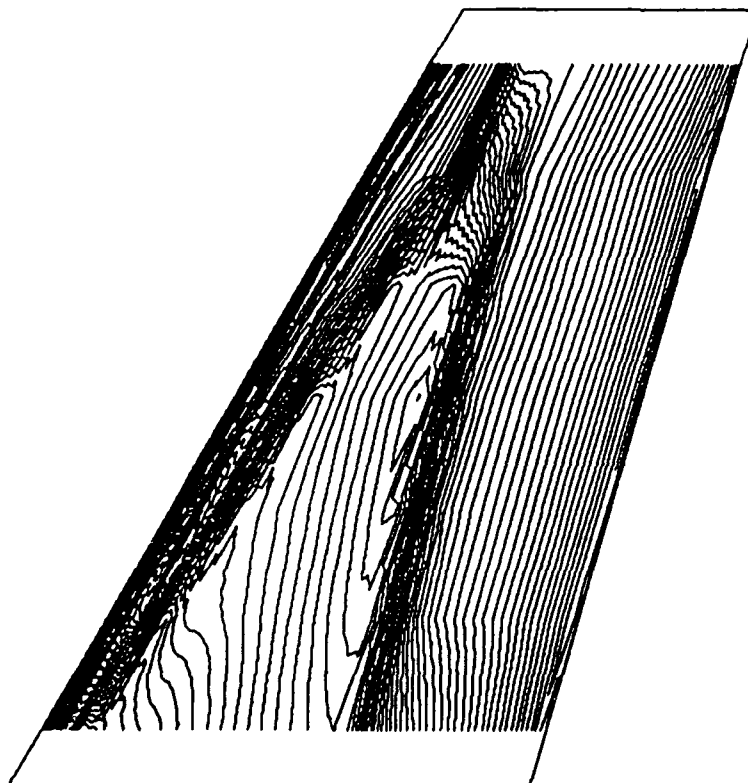
b. 65% semispan location

Figure 17. (continued)



c. 95% semispan location

Figure 17. (continued)

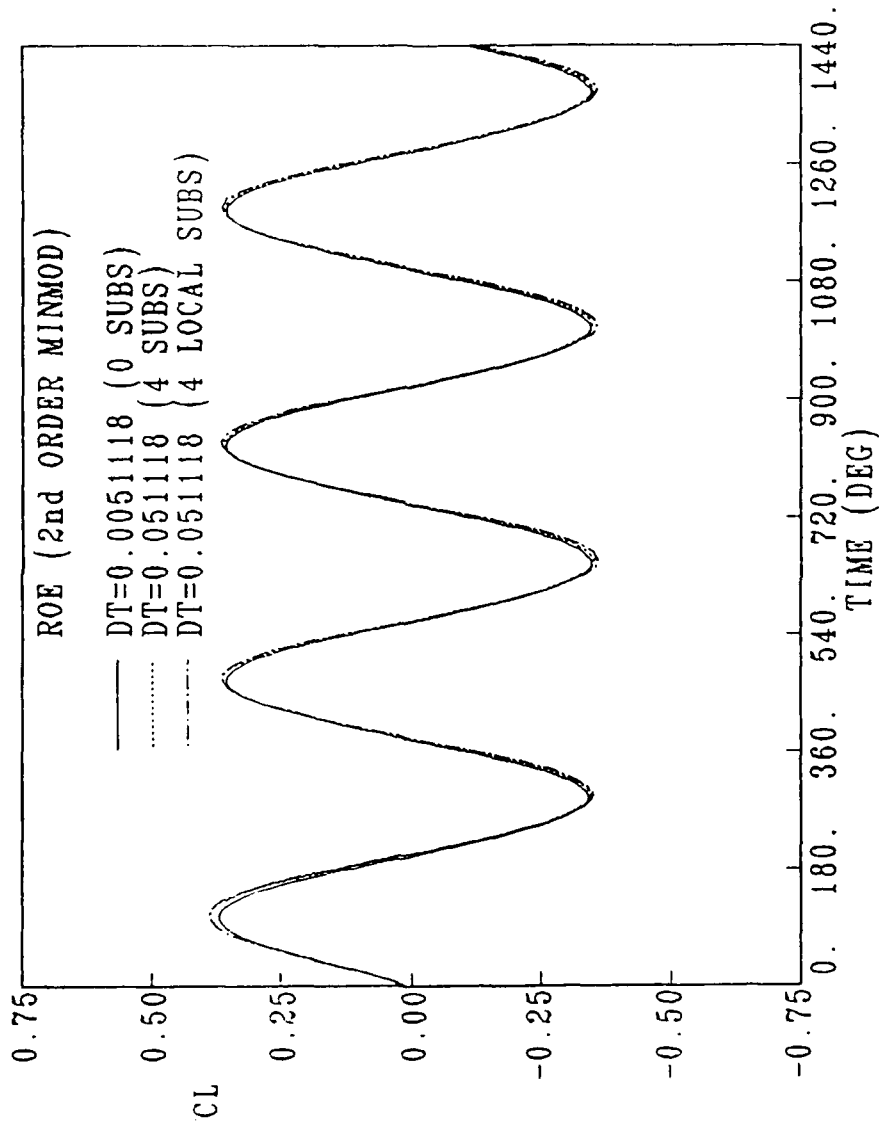


d. Upper surface pressure contours

Figure 17. (concluded)

# LIFT COEFFICIENT NACA 0012

MACH=0.755 MEAN ALPHA=0.016 DALPHA=2.51 K=0.1628

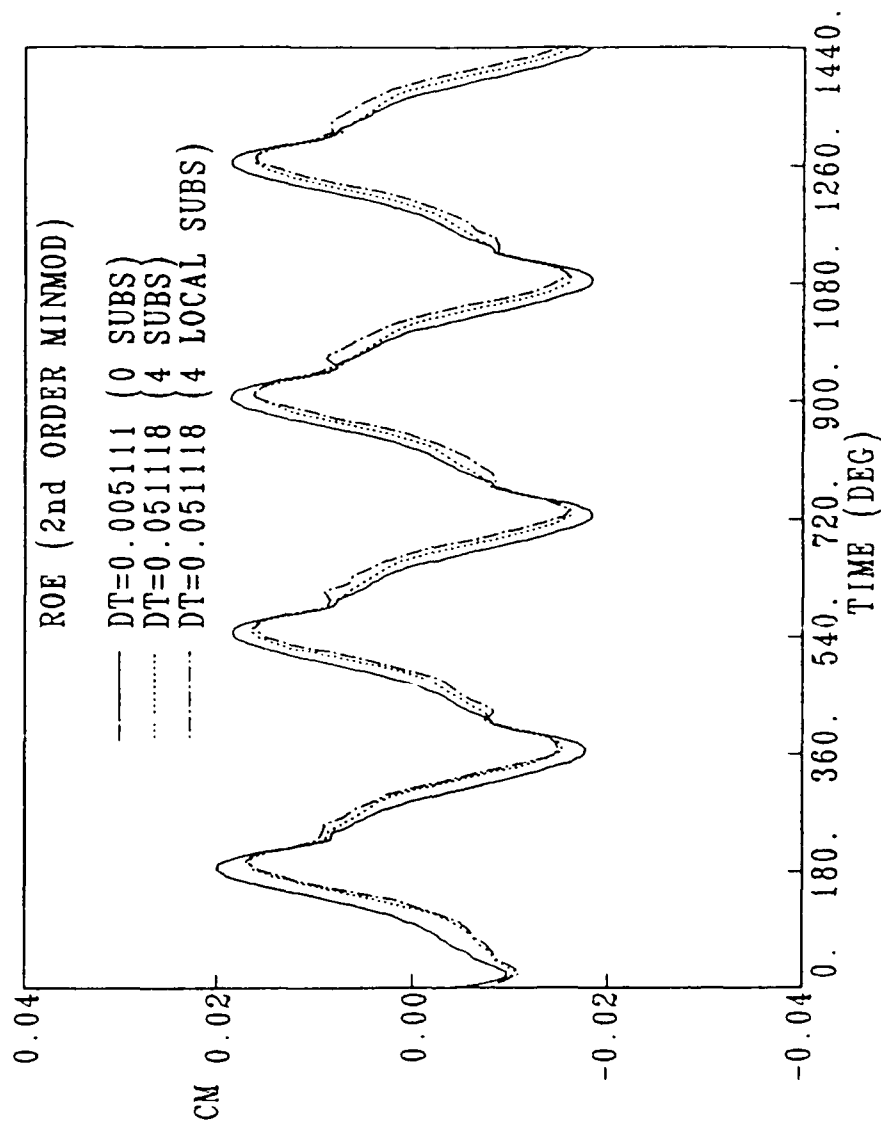


a. Lift coefficient vs time

Figure 18. Comparisons of lift and moment coefficients using 4 min and 4 local subiterations

# MOMENT COEFFICIENT NACA 0012

MACH=0.755 MEAN ALPHA=0.016 DALPHA=2.51 K=0.1628



b. Moment coefficient vs time

Figure 18. (concluded)

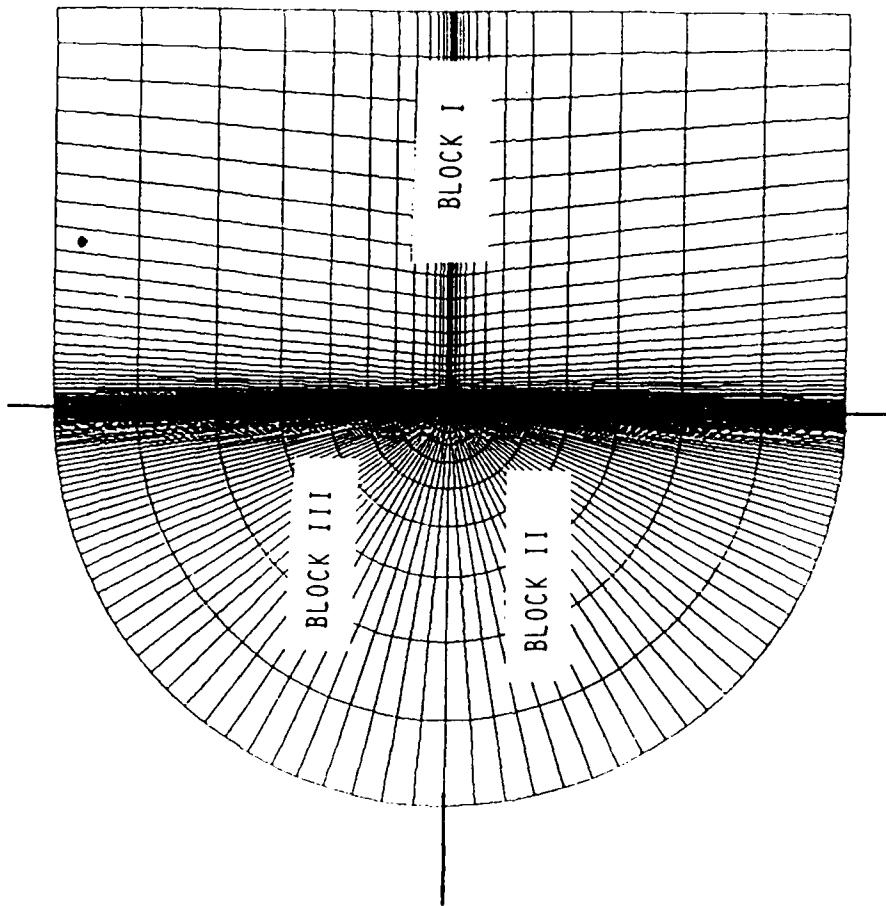
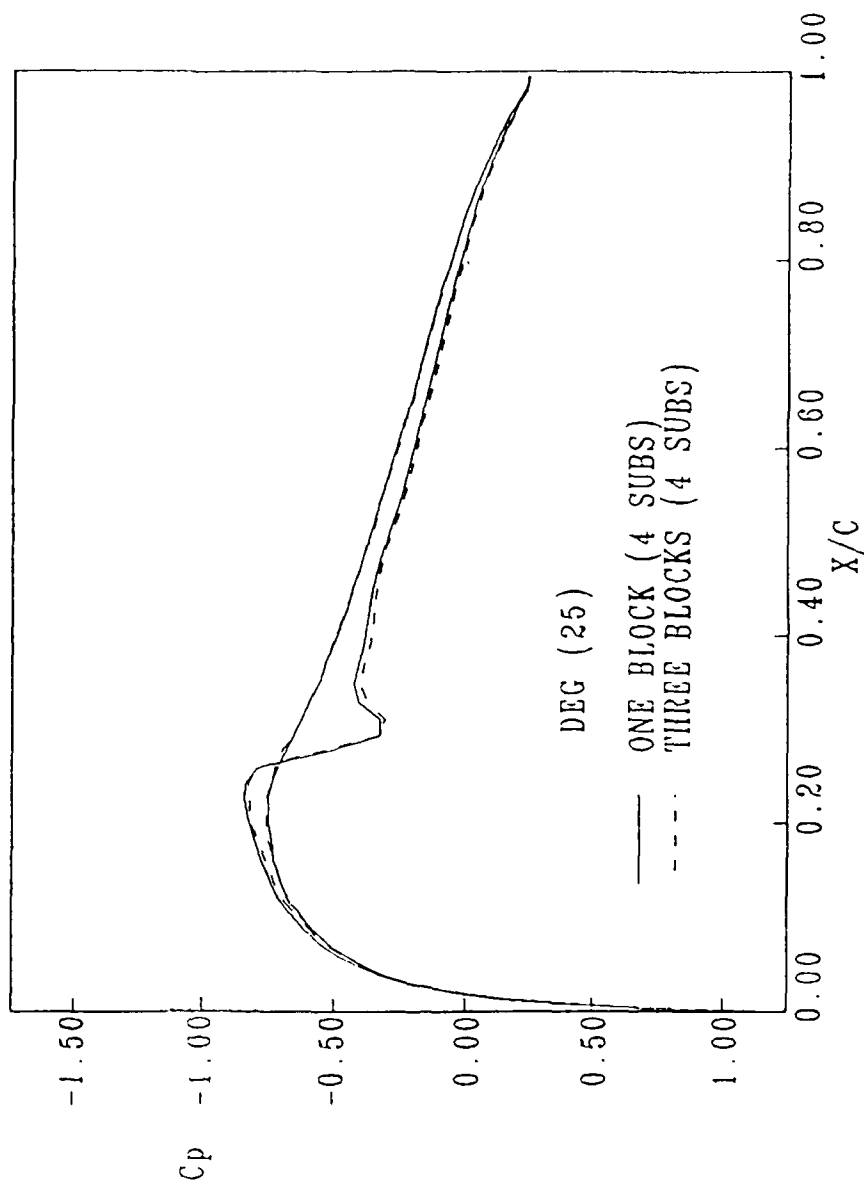


Figure 19. Three block version of "C" grid for NACA 0012

# NACA 0012 UNSTEADY PRESSURE DISTRIBUTION

MACH=0.755 RE=5.5E06 ALPHA=0.016 K=0.1628

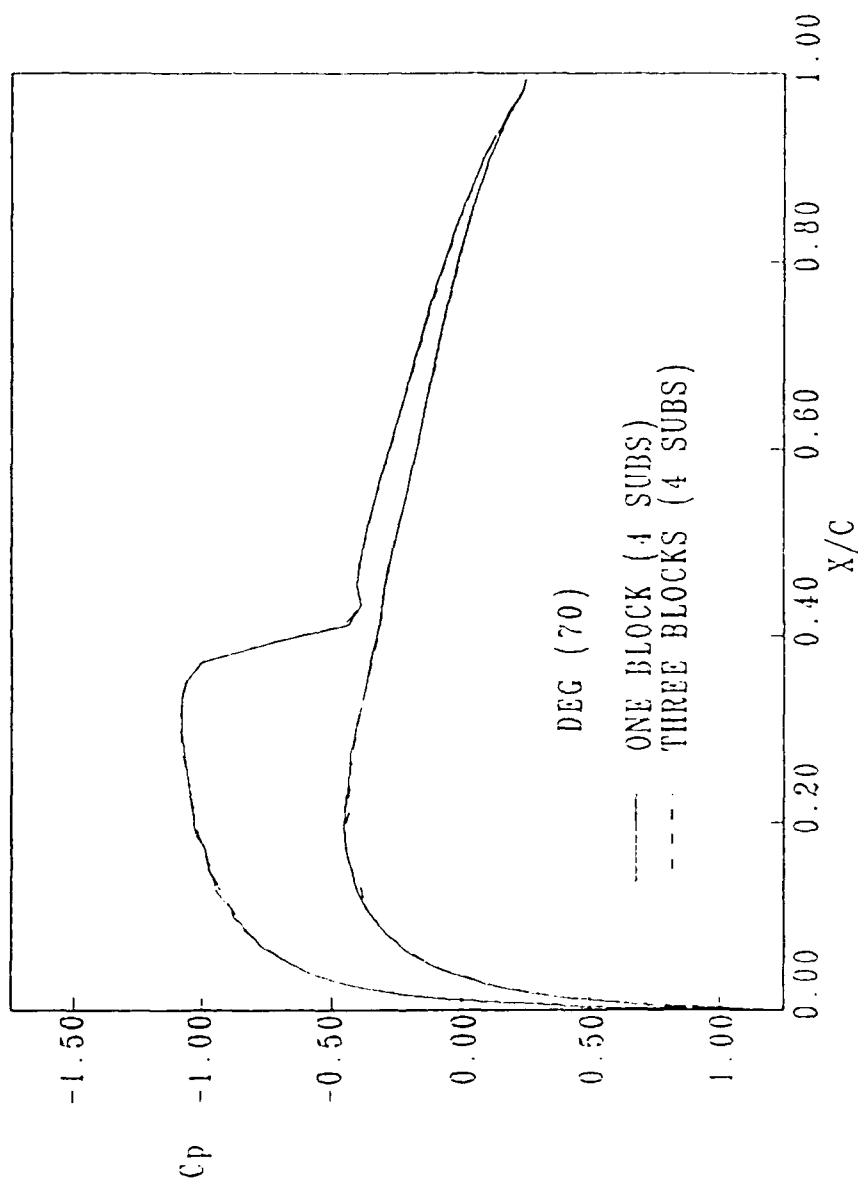


a. 25 degrees of oscillatory motion, AOA increasing (1.09)

Figure 20. Unsteady pressure distributions for 1 and 3 blocks

# NACA 0012 UNSTEADY PRESSURE DISTRIBUTION

MACH=0.755 RE=5.5E06 ALPHA=0.016 K=0.1628



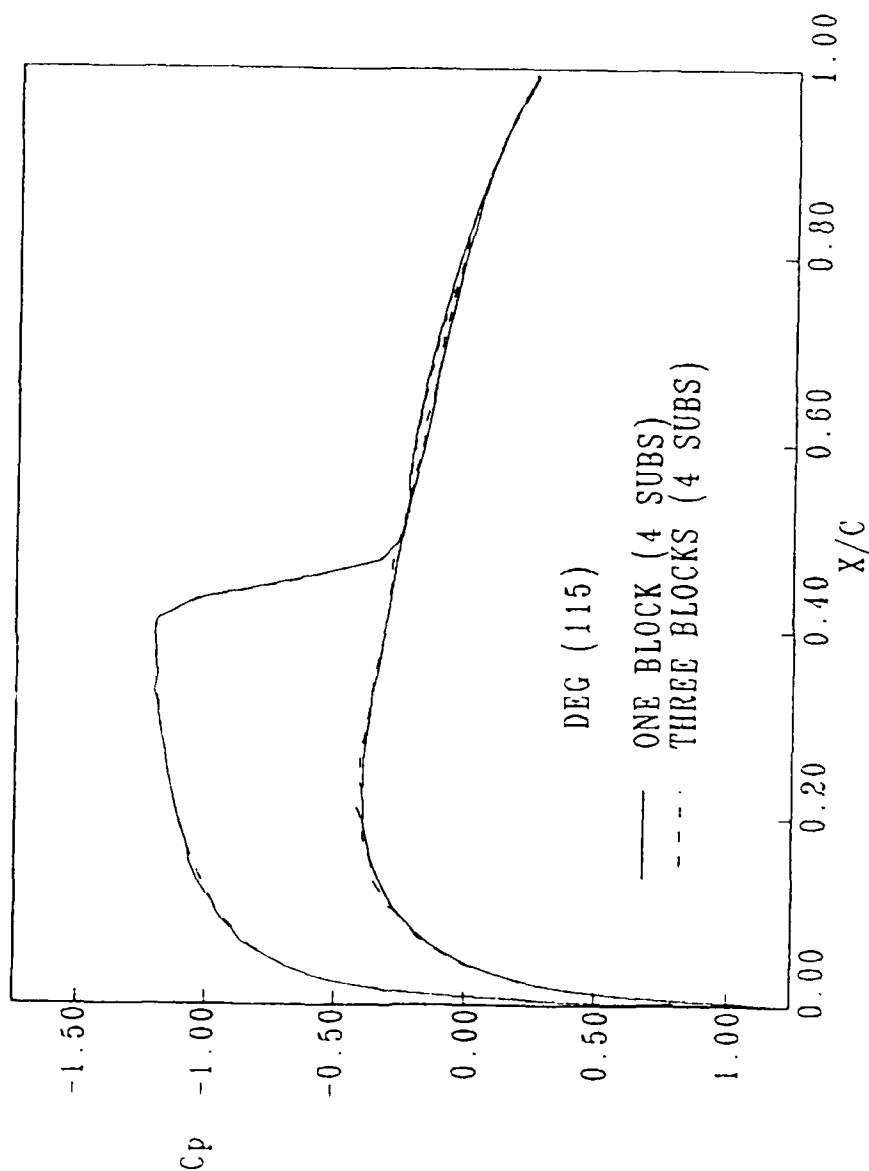
b. 70 degrees of oscillatory motion, AOA increasing (2.37)

Figure 20. (continued)



# NACA 0012 UNSTEADY PRESSURE DISTRIBUTION

MACH=0.755 RE=5.5E06 ALPHA=0.016 K=0.1628

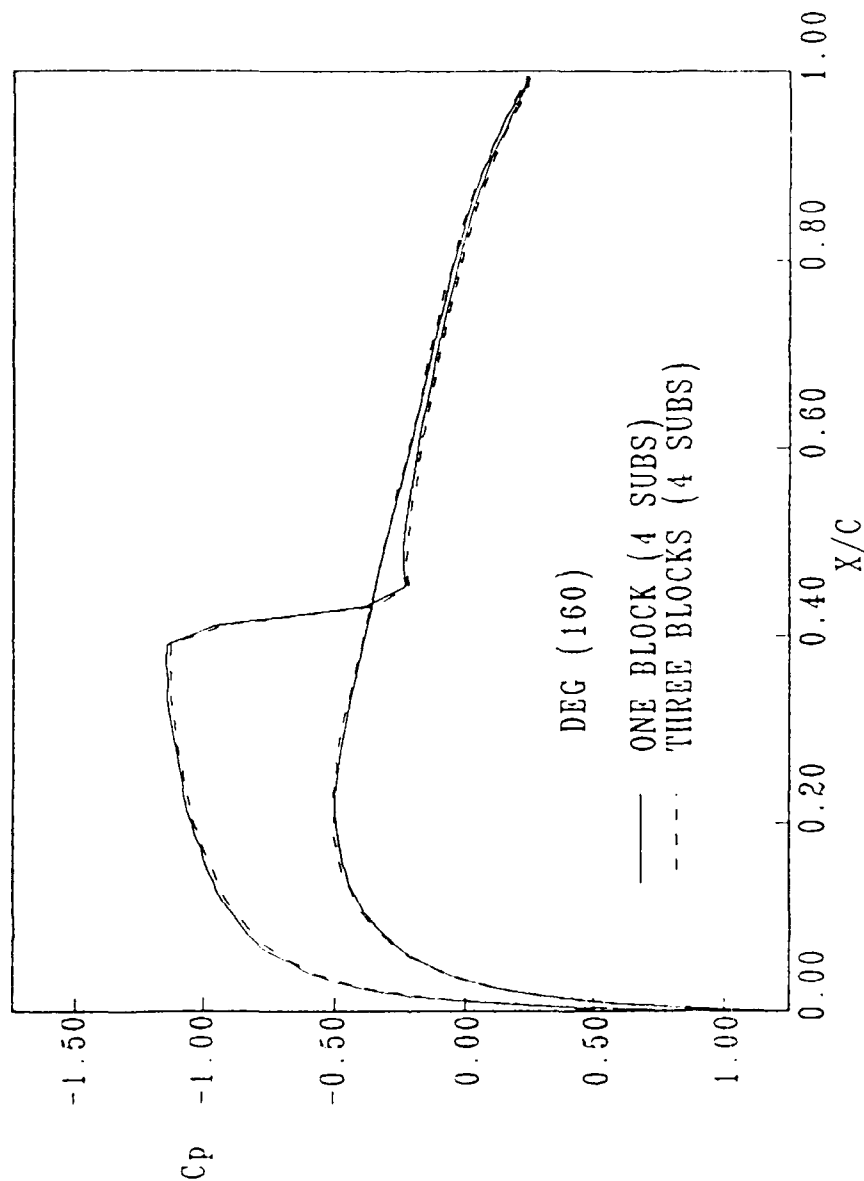


c. 115 degrees of oscillatory motion, AOA decreasing (2.29)

Figure 20. (Continued)

# NACA 0012 UNSTEADY PRESSURE DISTRIBUTION

MACH=0.755 RE=5.5E06 ALPHA=0.016 K=0.1620

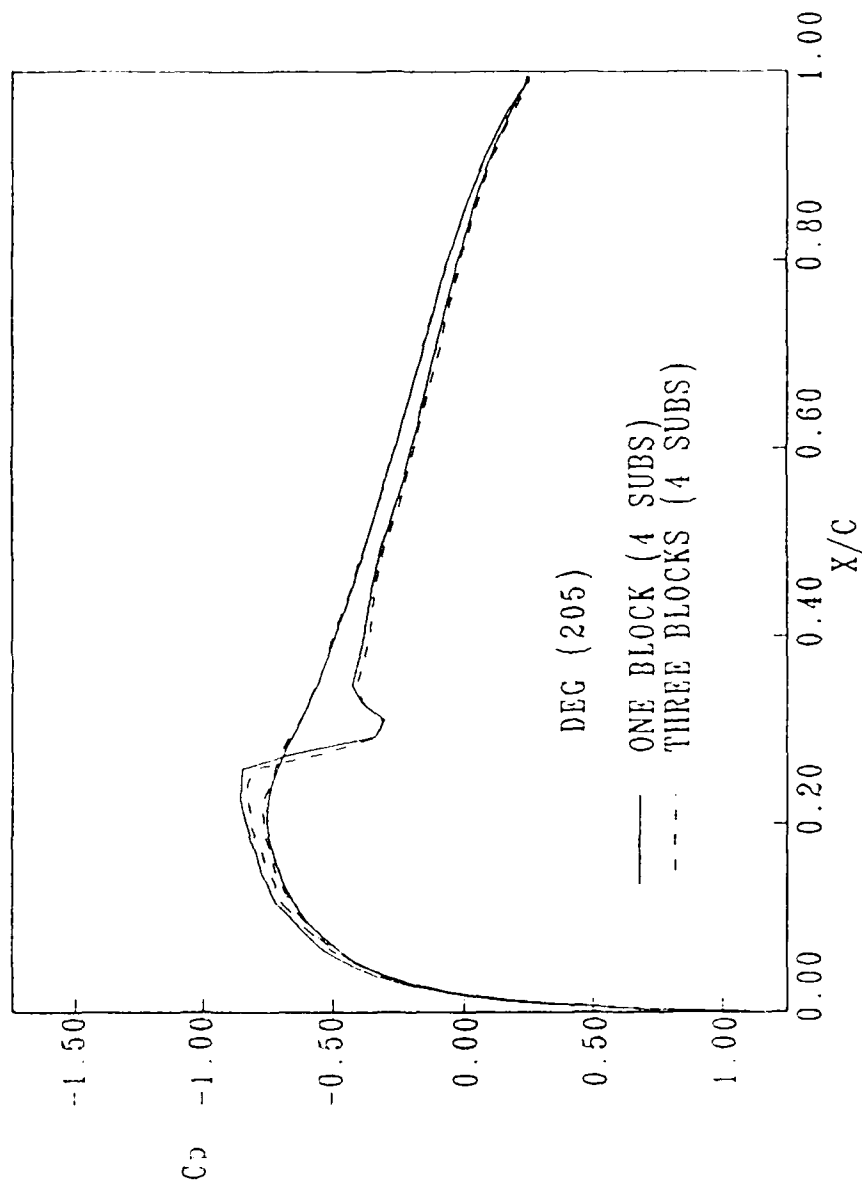


d. 160 degrees of oscillatory motion, AOA decreasing (0.87)

Figure 20. (continued)

# NACA 0012 UNSTEADY PRESSURE DISTRIBUTION

MACH=0.755 RE=5.5E06 ALPHA=0.016 K=0.1620

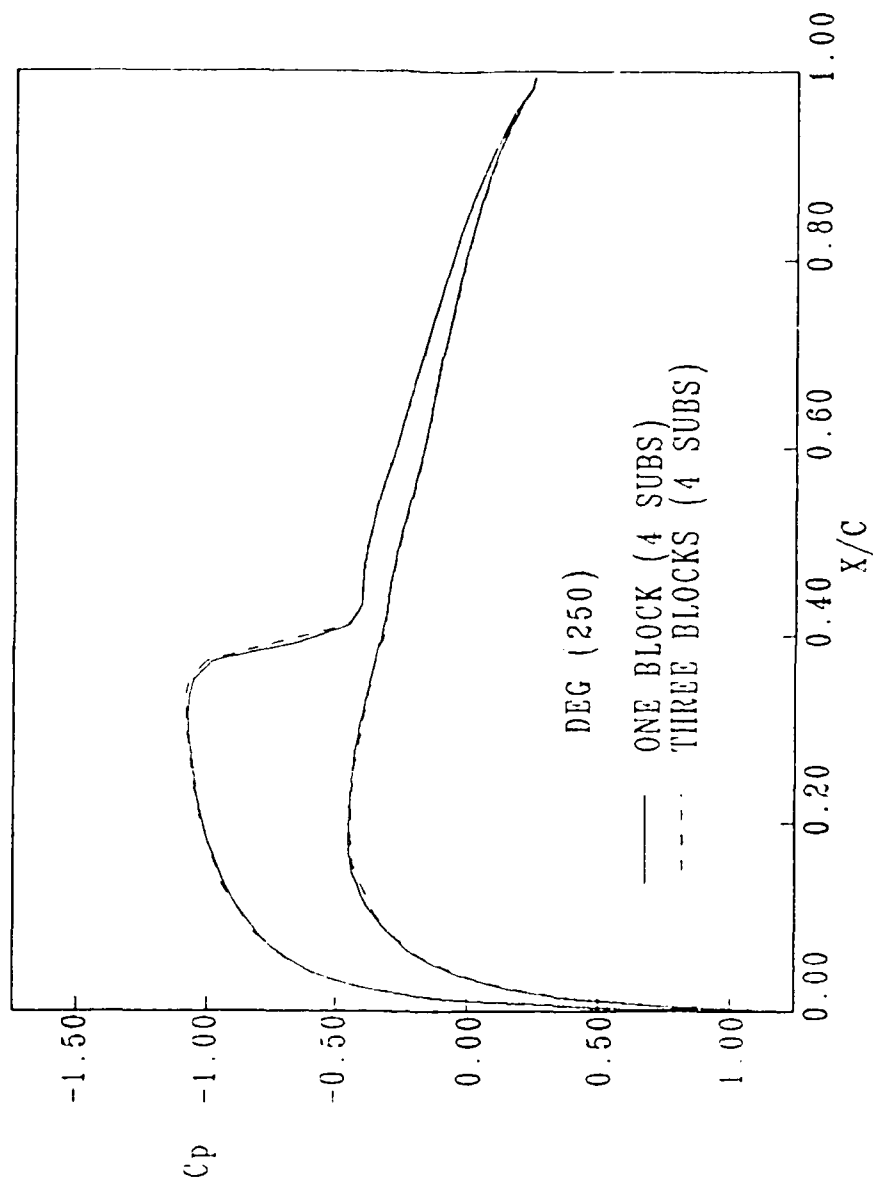


e. 205 degrees of oscillatory motion, AOA decreasing (-1.04)

Figure 20. (continued)

# NACA 0012 UNSTEADY PRESSURE DISTRIBUTION

MACH=0.755 RE=5.5E06 ALPHA=0.016 K=0.1628

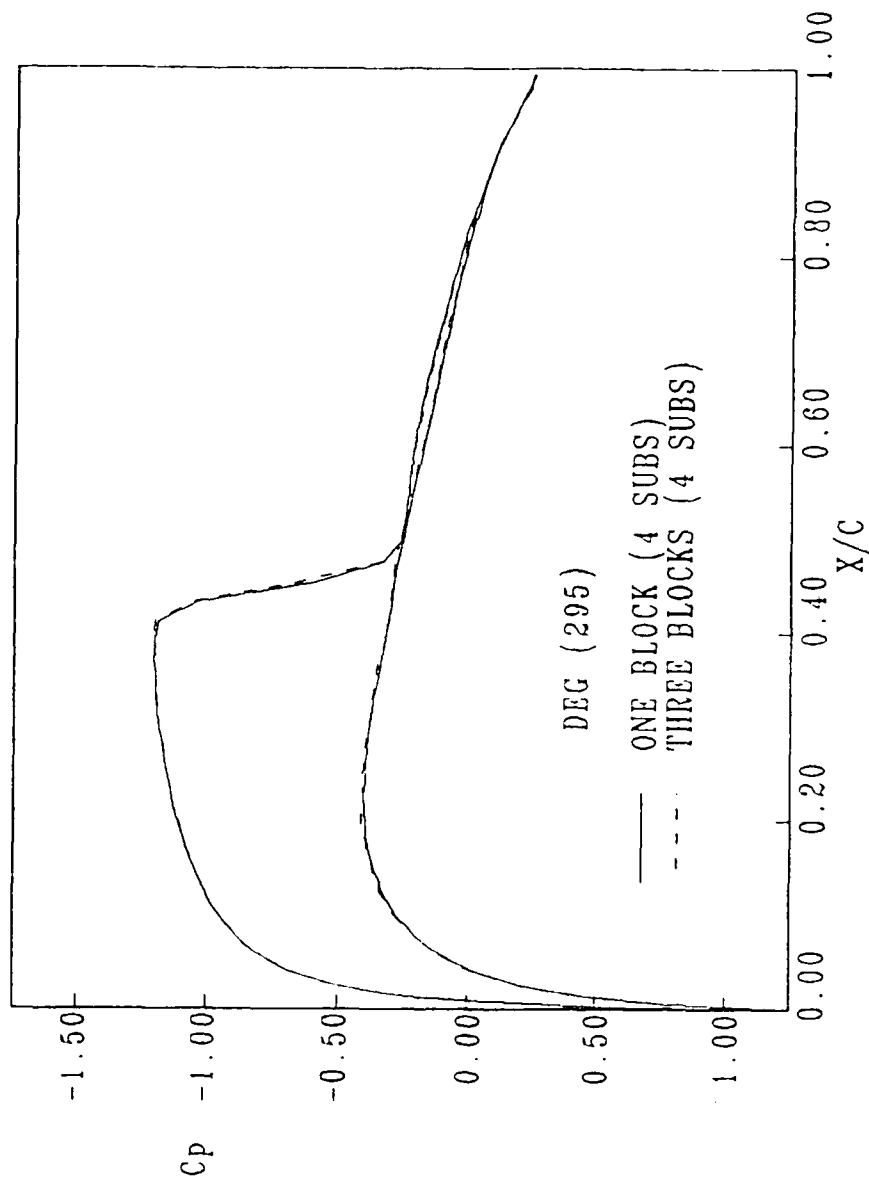


f. 250 degrees of oscillatory motion, AOA decreasing (-2.34)

Figure 20. (continued)

# NACA 0012 UNSTEADY PRESSURE DISTRIBUTION

MACH=0.755 RE=5.5E06 ALPHA=0.016 K=0.1620

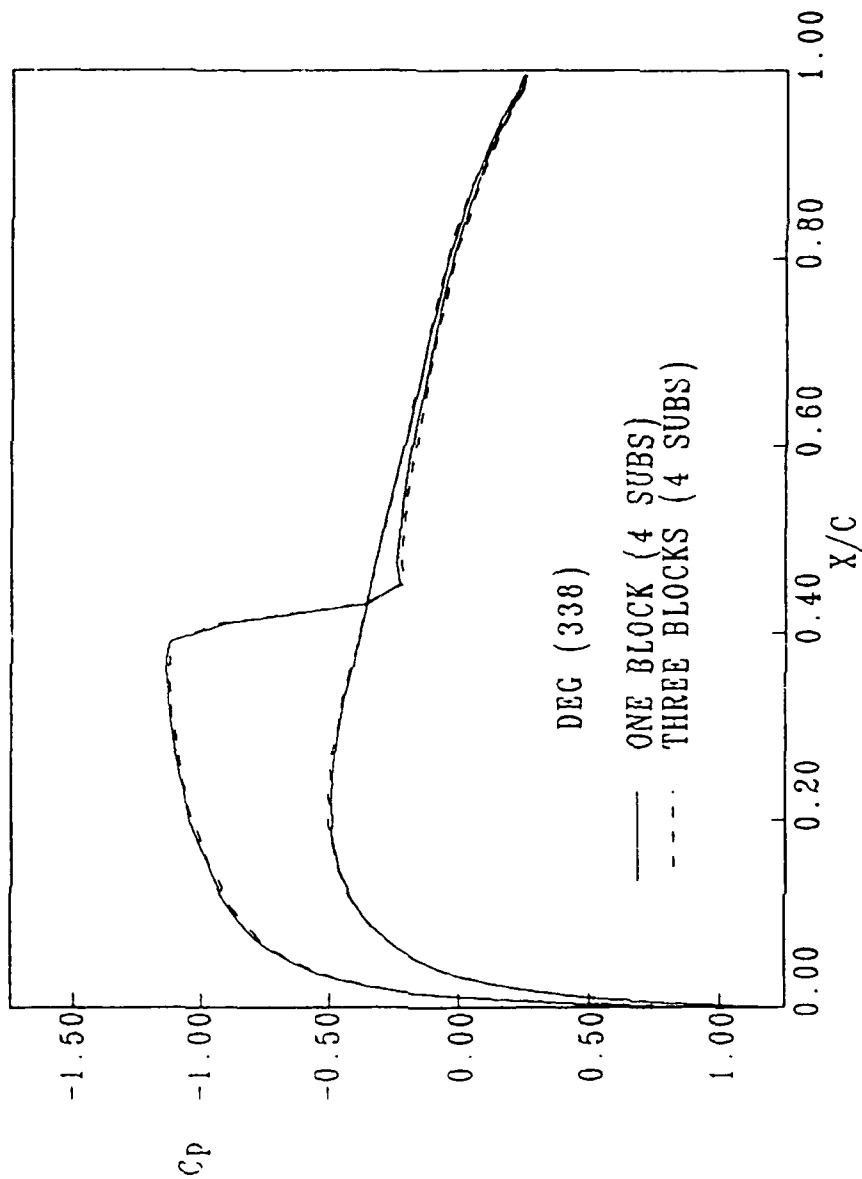


3. 295 degrees of oscillatory motion, AOA increasing (-2.26)

Figure 20. (continued)

# NACA 0012 UNSTEADY PRESSURE DISTRIBUTION

MACH=0.755 RE=5.5E06 ALPHA=0.016 K=0.1628



h. 338 degrees of oscillatory motion, AOA increasing (-0.84)

Figure 20. (concluded)

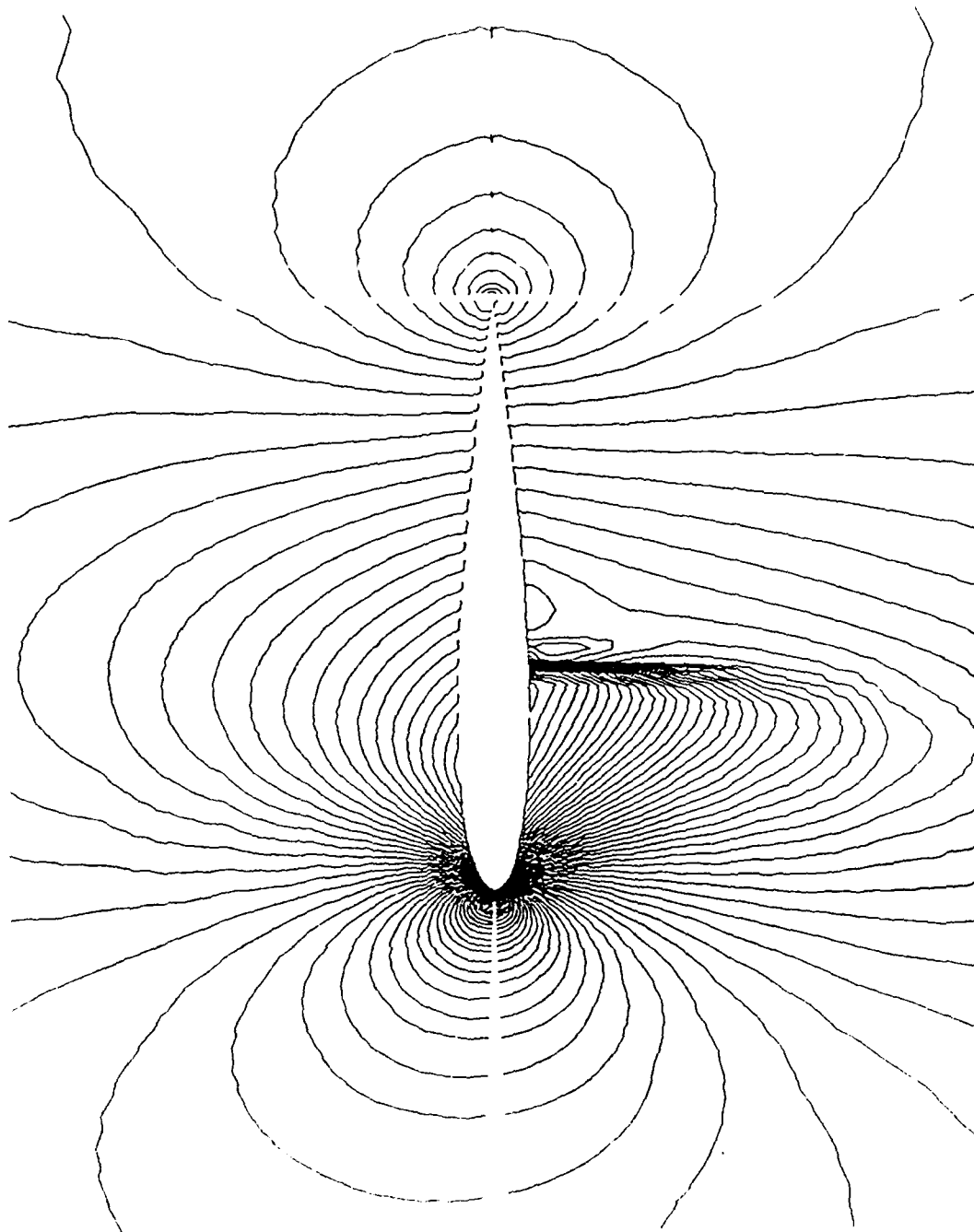
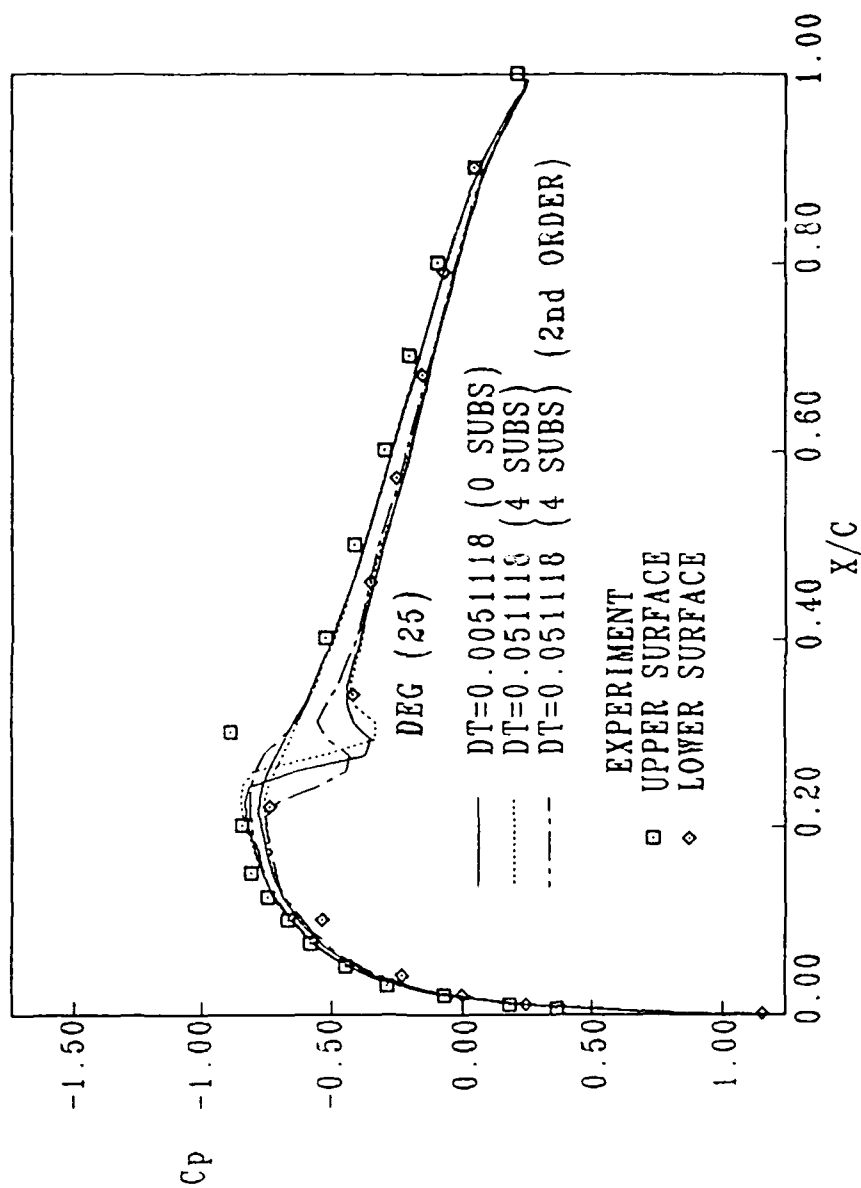


Figure 21. Pressure contours for 3 block NACA 0012 at 360 degrees of oscillatory motion

# NACA 0012 UNSTEADY PRESSURE DISTRIBUTION

MACH=0.755 RE=5.5E06 ALPHA=0.016 K=0.1628



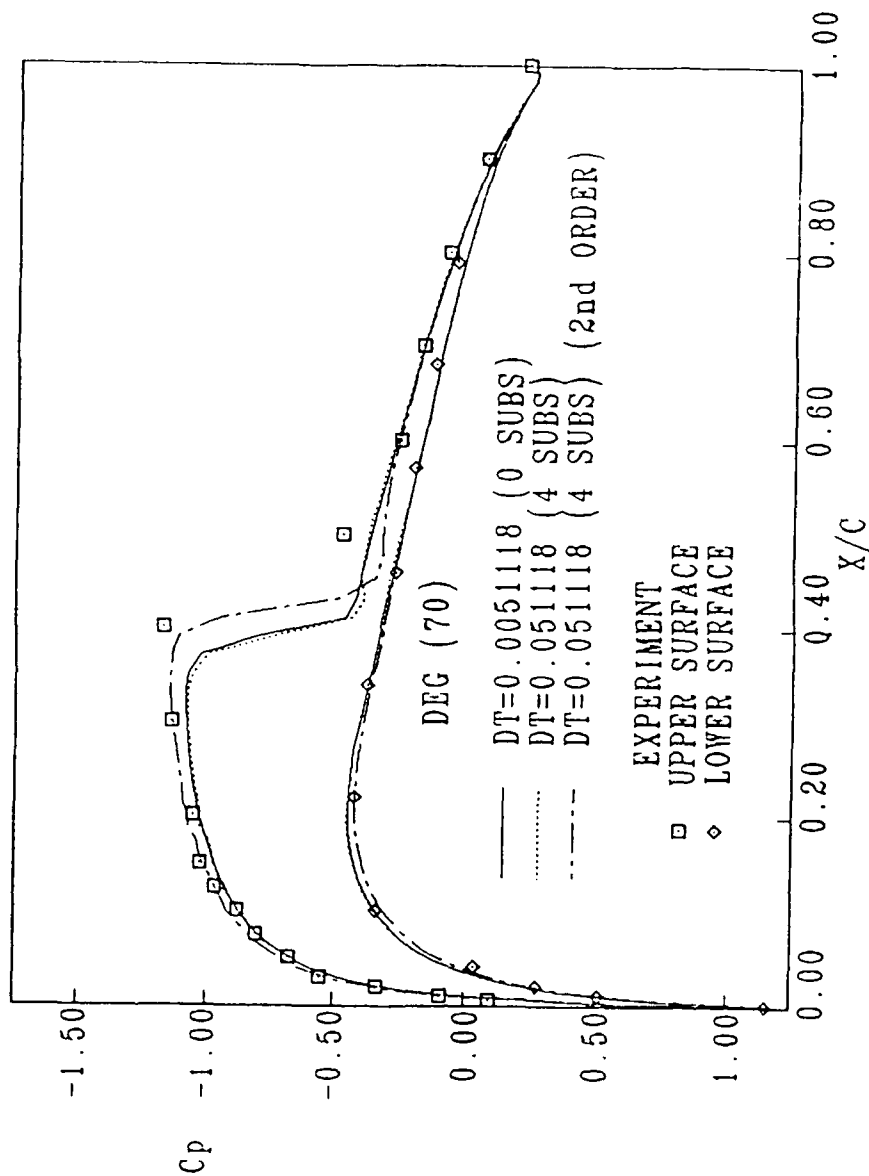
a. 25 degrees of oscillatory motion

Figure 22. Unsteady pressure distributions for 1st and 2nd order time accuracy using 4 min subiterations and  $DT = .0511$



# NACA 0012 UNSTEADY PRESSURE DISTRIBUTION

MACH=0.755 RE=5.5E06 ALPHA=0.016 K=0.1628

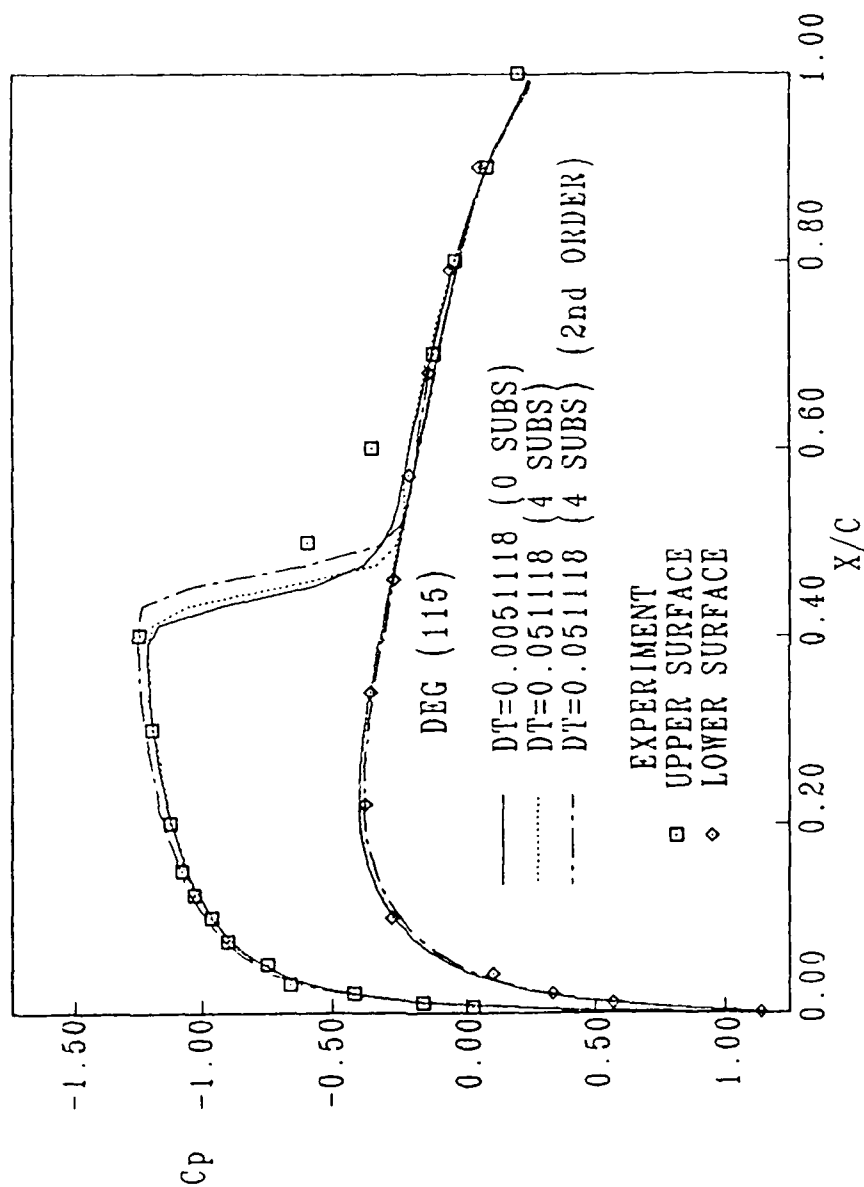


b. 70 degrees of oscillatory motion

Figure 22. (continued)

# NACA 0012 UNSTEADY PRESSURE DISTRIBUTION

MACH=0.755 RE=5.5E06 ALPHA=0.016 K=0.1628

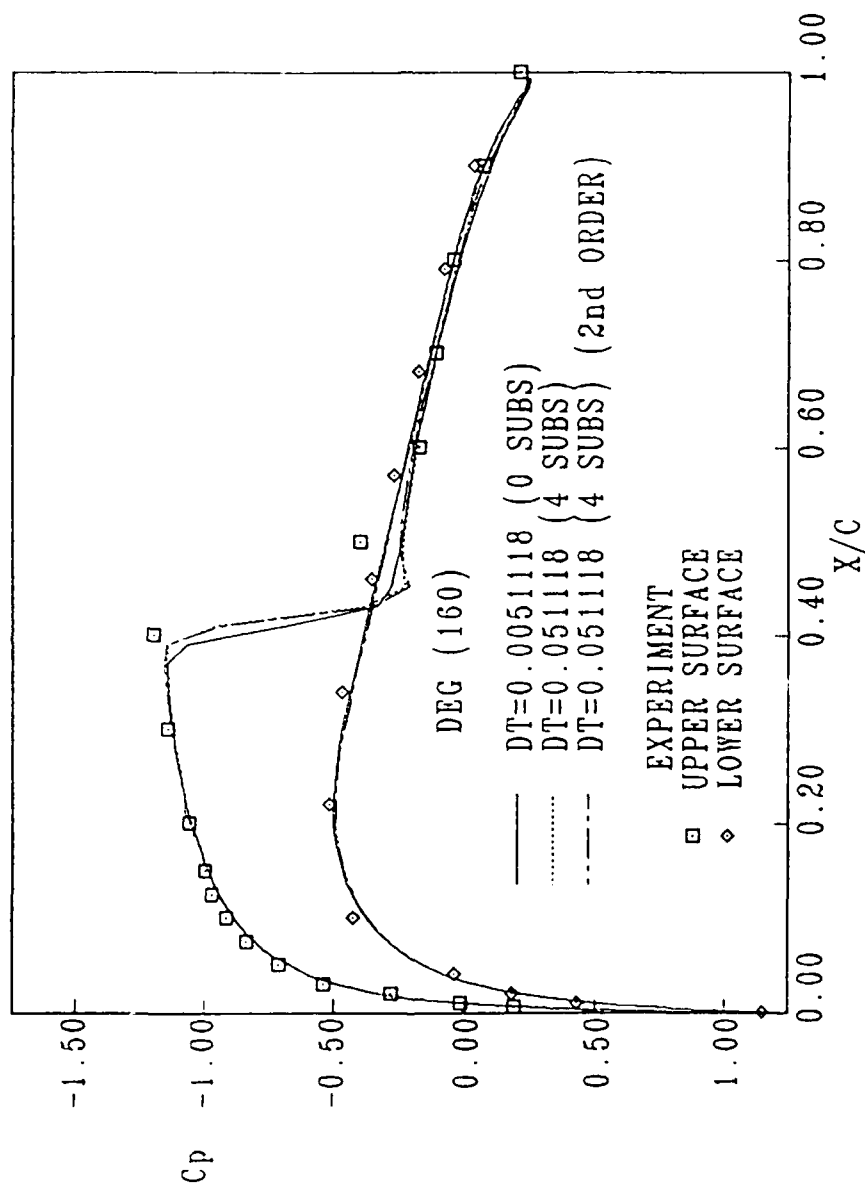


c. 115 degrees of oscillatory motion

Figure 22. (continued)

# NACA 0012 UNSTEADY PRESSURE DISTRIBUTION

MACH=0.755 RE=5.5E06 ALPHA=0.016 K=0.1628

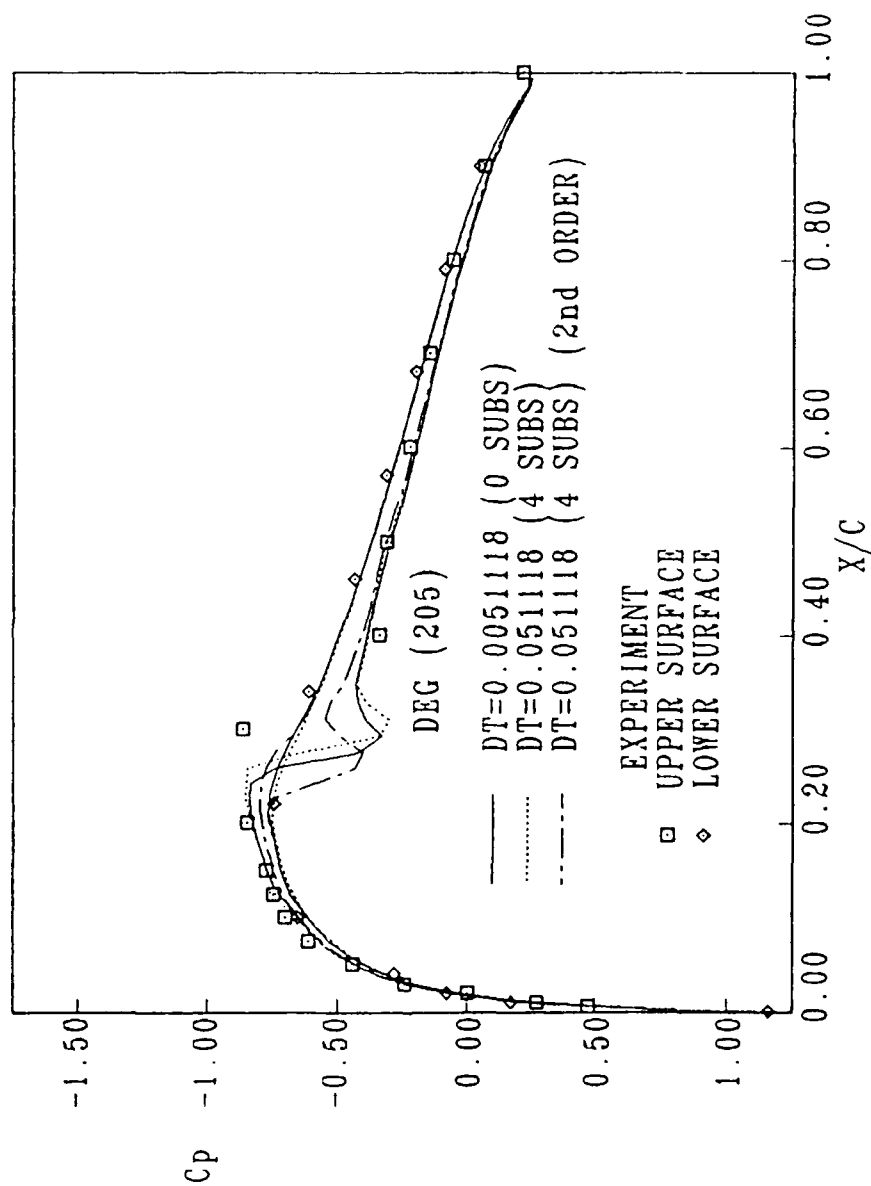


d. 160 degrees of oscillatory motion

Figure 22. (continued)

# NACA 0012 UNSTEADY PRESSURE DISTRIBUTION

MACH=0.755 RE=5.5E06 ALPHA=0.016 K=0.162U

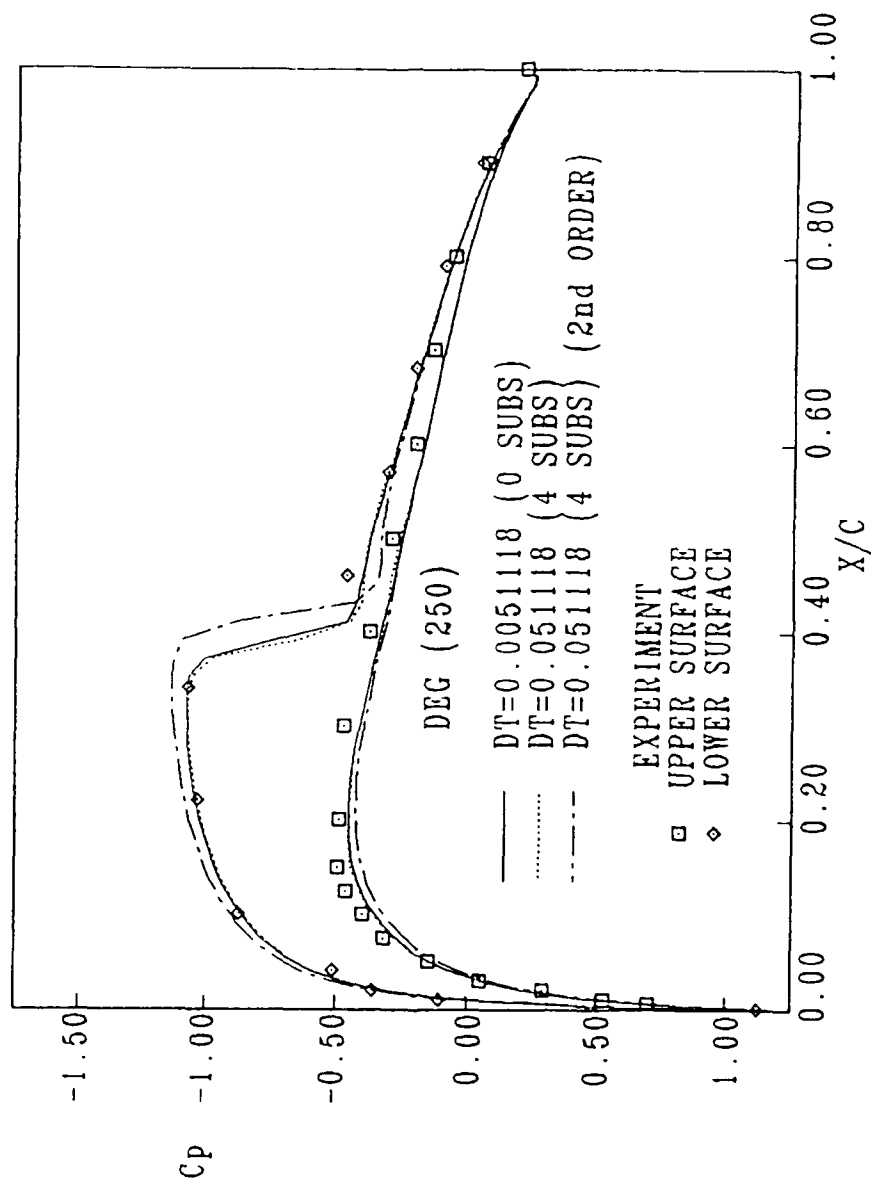


e. 205 degrees of oscillatory motion

Figure 22. (continued)

# NACA 0012 UNSTEADY PRESSURE DISTRIBUTION

MACI=0.755 RE=5.5E06 ALPHA=0.016 K=0.1628

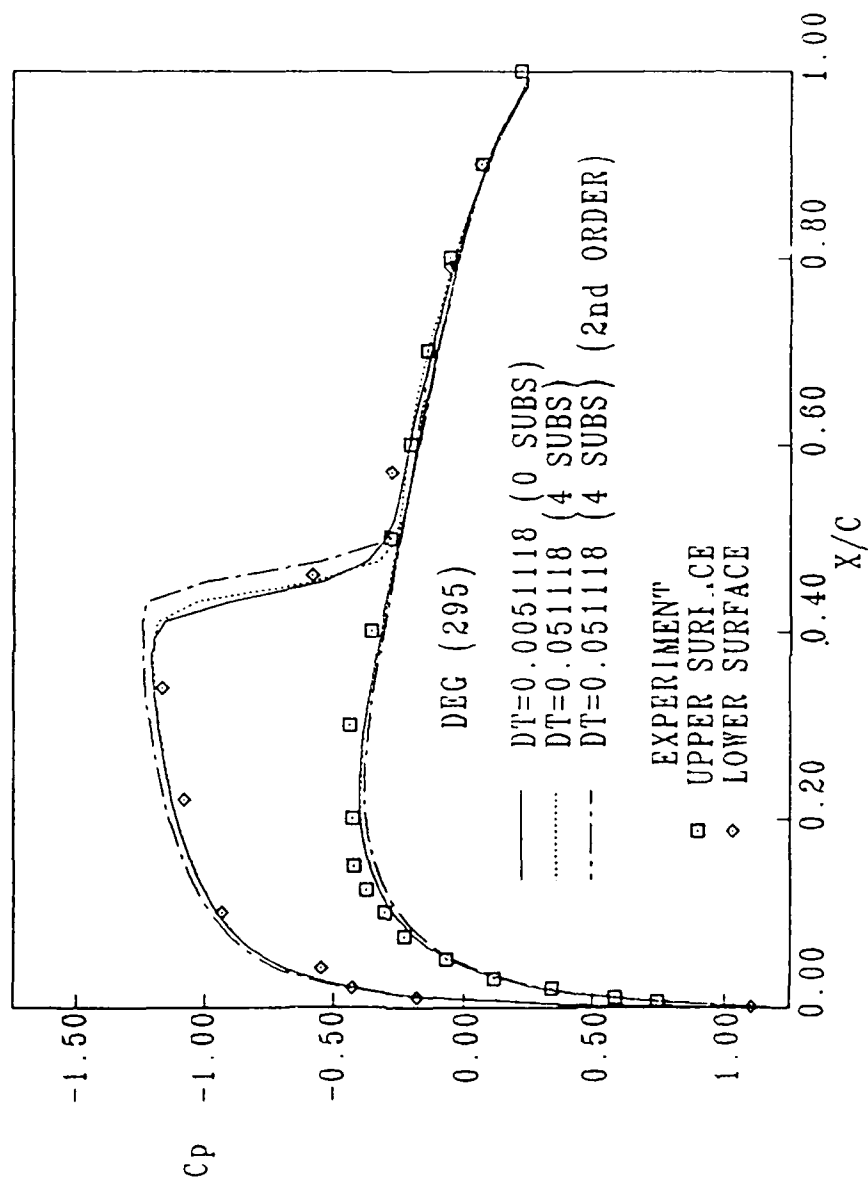


f. 250 degrees of oscillatory motion

Figure 22. (continued)

# NACA 0012 UNSTEADY PRESSURE DISTRIBUTION

MACH=0.755 RE=5.5E06 ALPHA=0.016 K=0.1628

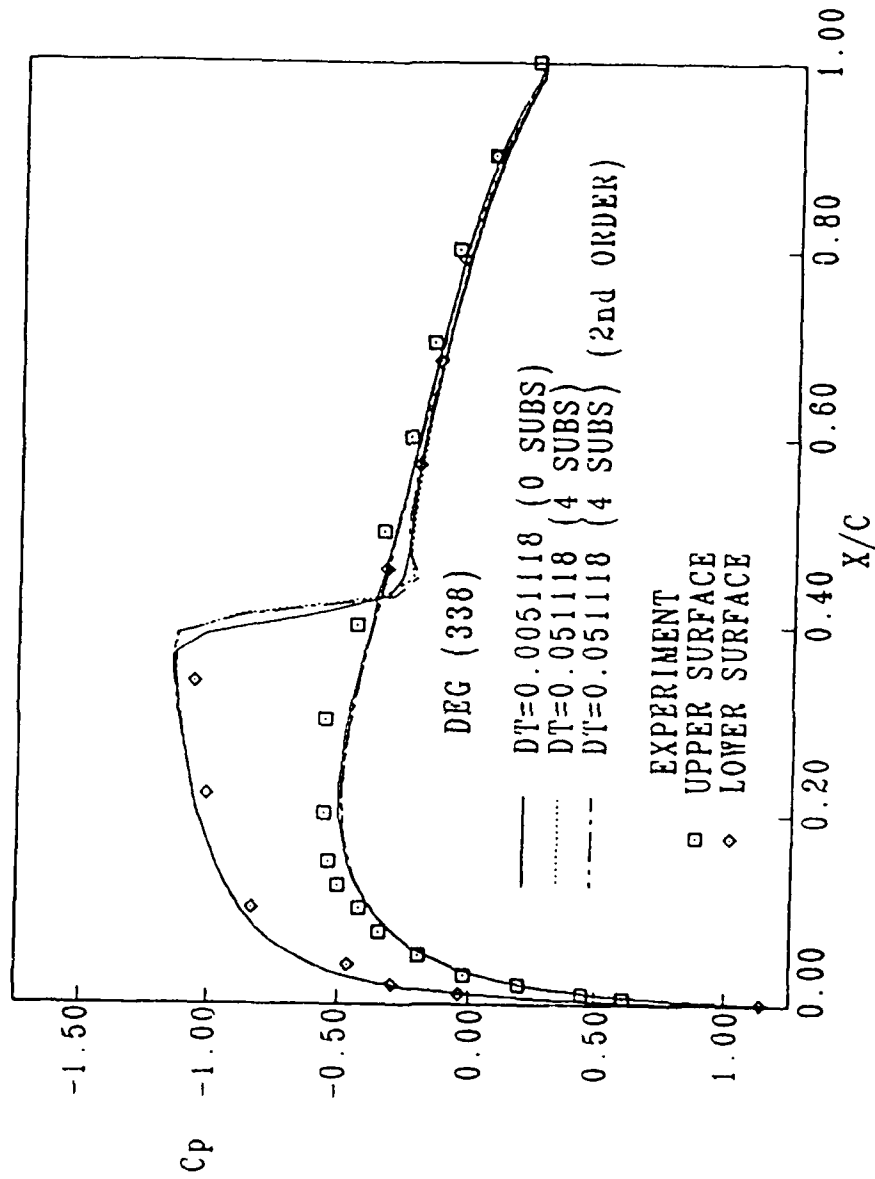


g. 295 degrees of oscillatory motion

Figure 22. (continued)

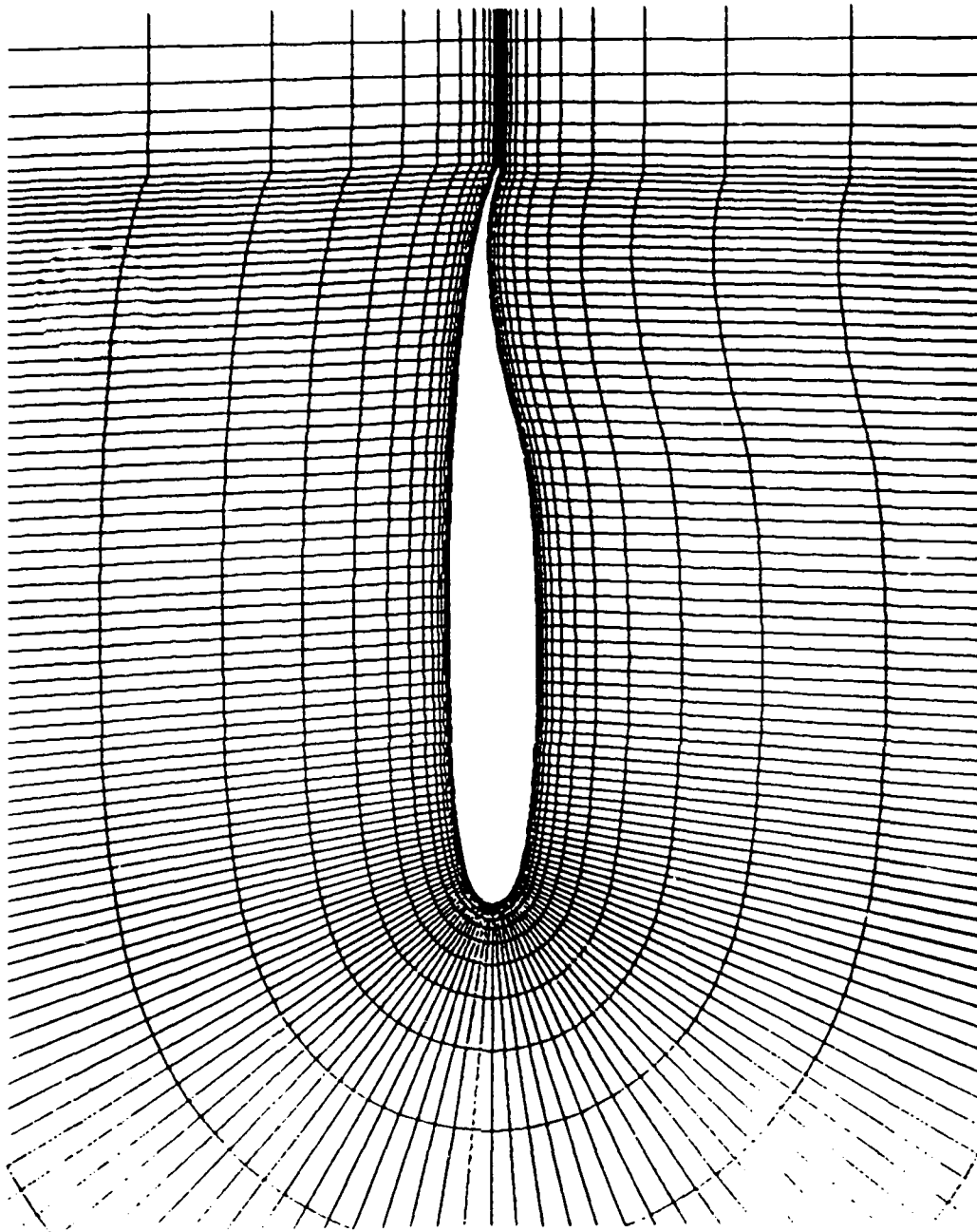
# NACA 0012 UNSTEADY PRESSURE DISTRIBUTION

MACH=0.755 RE=5.5E06 ALPHA=0.016 K=0.1620



h. 338 degrees of oscillatory motion

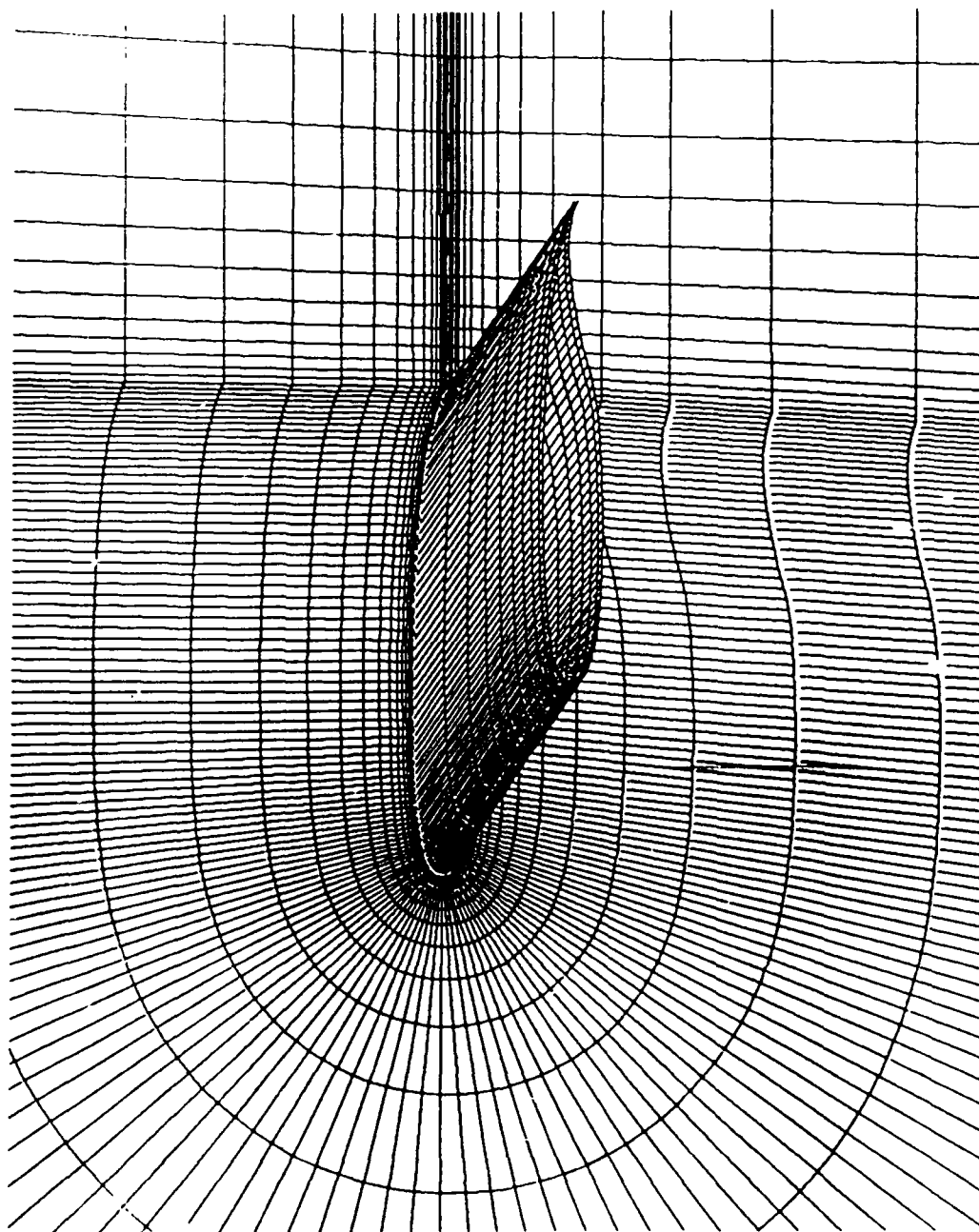
Figure 22. (concluded)



a. 221 points in the streamwise direction, 40 points in the normal direction

Figure 23. "C-H" grid for rectangular supercritical wing



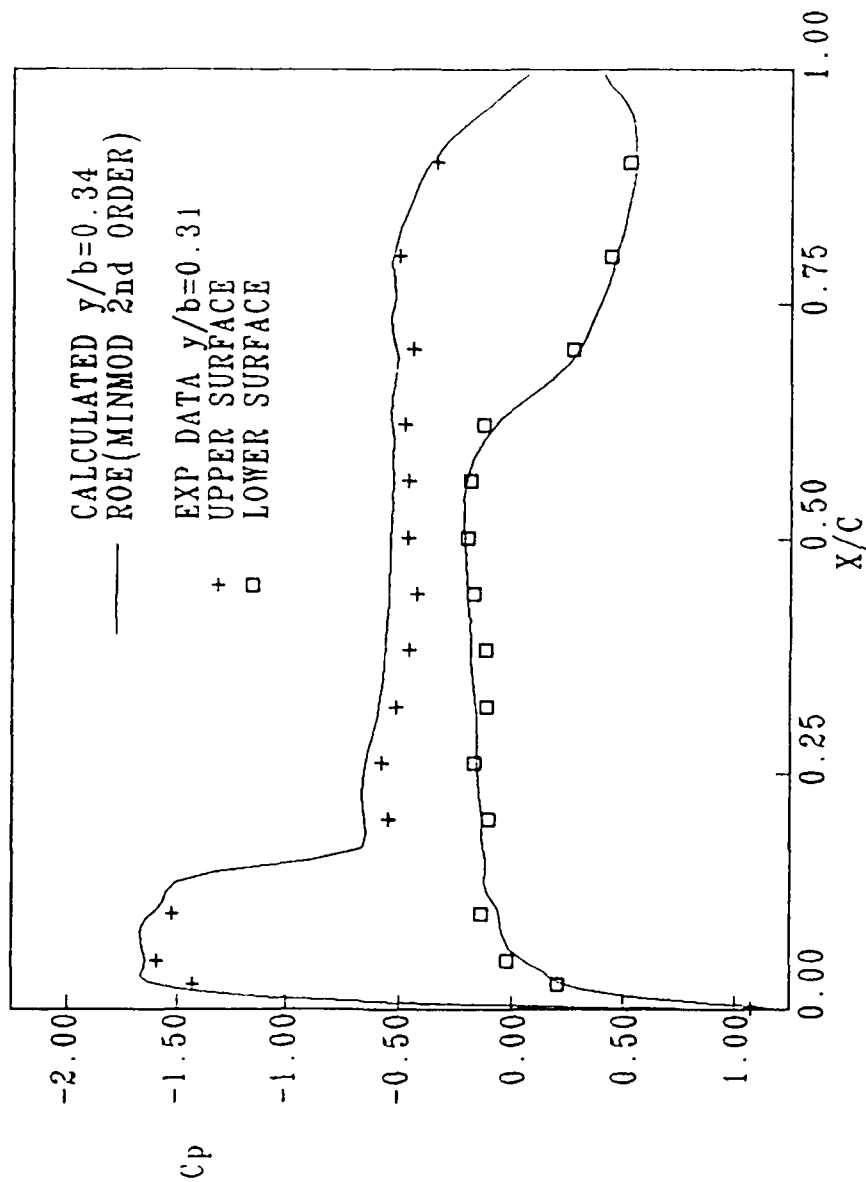


b. Distribution of constant spanwise location planes along the wing

Figure 23. (concluded)

# RECTANGULAR SUPERCRITICAL WING STEADY PRESSURE DISTRIBUTION

MACH=0.704 RE=4.03E06 ALPHA=4.00

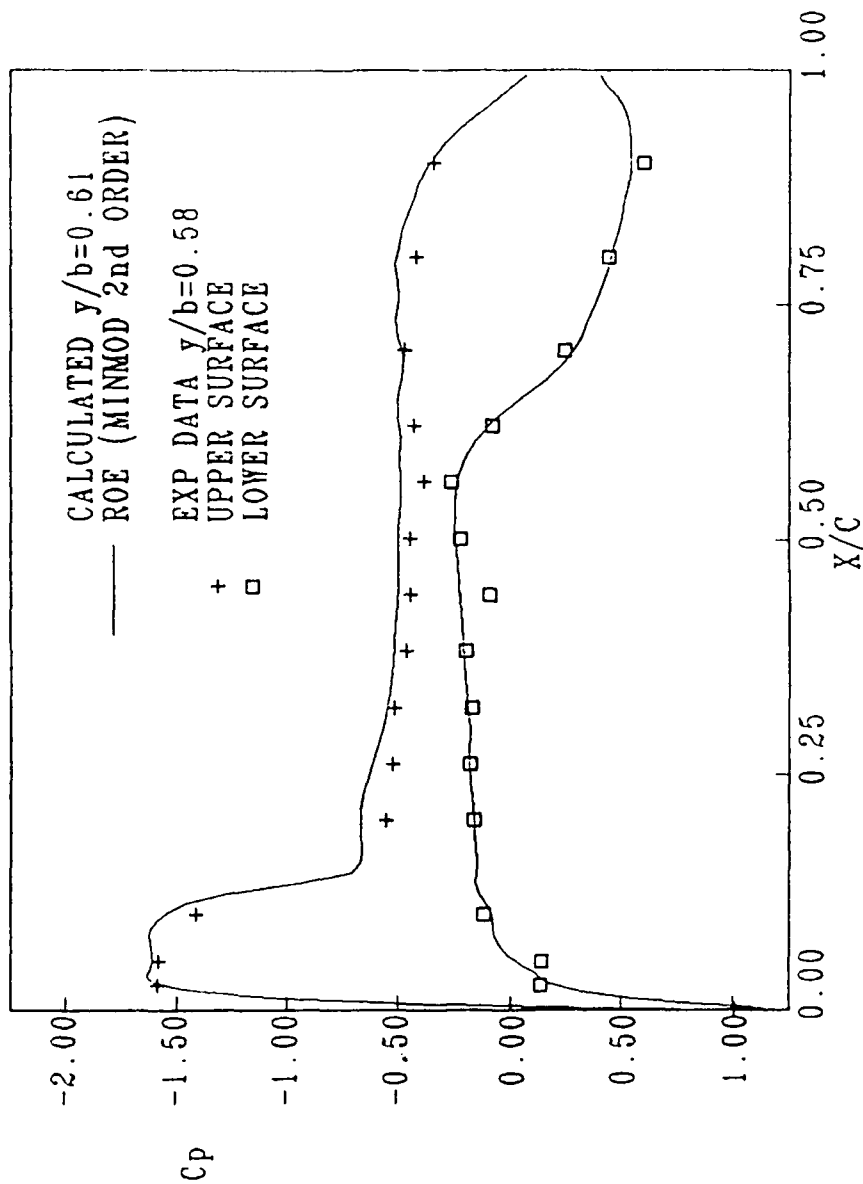


a. 34% semispan calculated, 31% experiment

Figure 24. Steady pressure distributions for the rectangular supercritical wing compared with experiment

# RECTANGULAR SUPERCritical WING STEADY PRESSURE DISTRIBUTION

MACH=0.704 RE=4.03E06 ALPHA=4.00

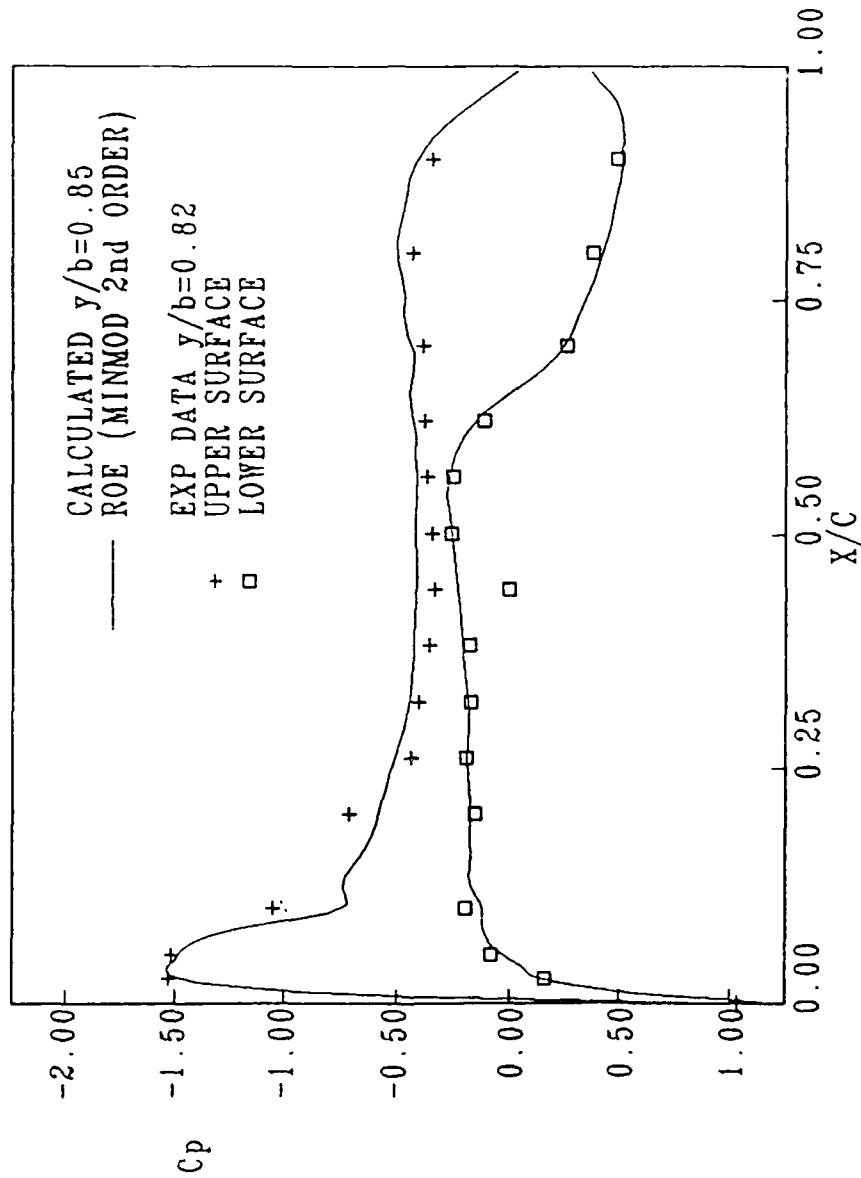


b. 61% semispan calculated, 58% experiment

Figure 24. (continued)

# RECTANGULAR SUPERCRITICAL WING STEADY PRESSURE DISTRIBUTION

MACH=0.704 RE=4.03E06 ALPHA=4.00

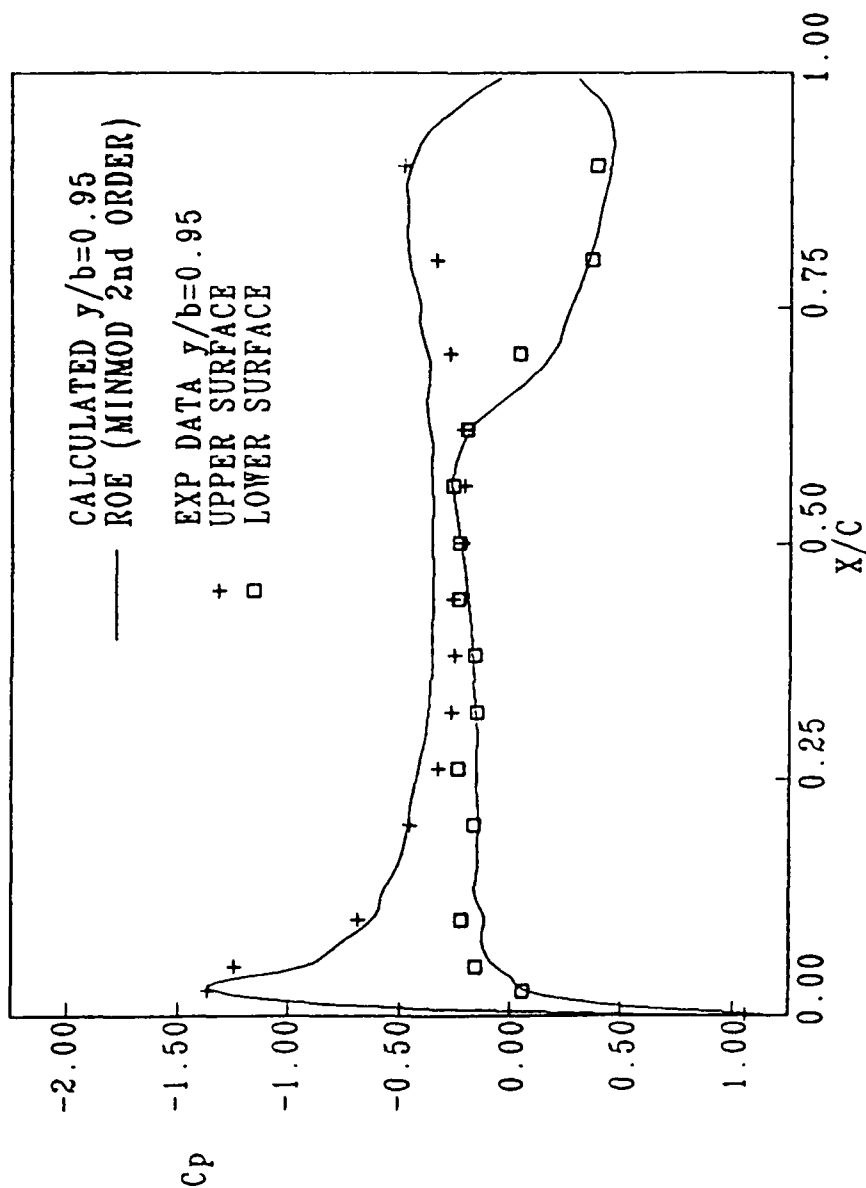


c. 85% semispan calculated, 82% experiment

Figure 24. (continued)

# RECTANGULAR SUPERCritical WING STEADY PRESSURE DISTRIBUTION

MACH=0.704 RE=4.03E06 ALPHA=4.00

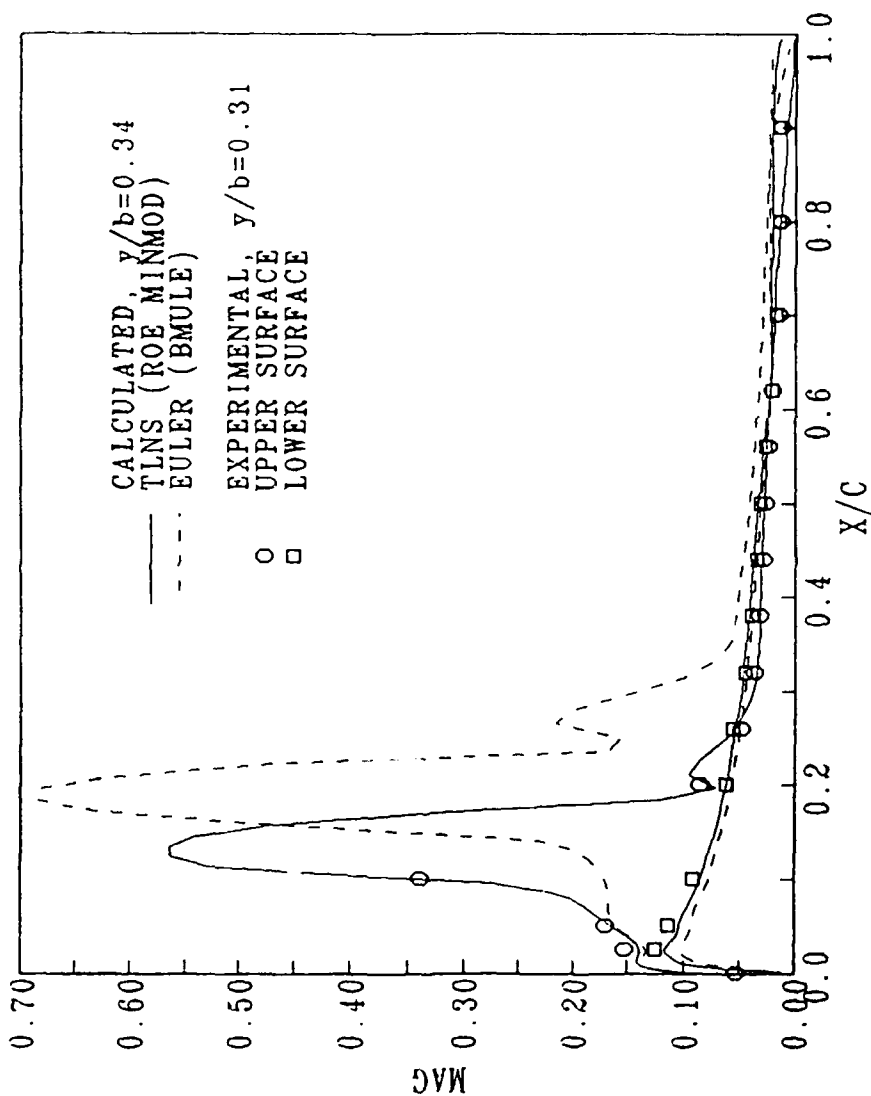


d. 95% semispan calculated, 95% experiment

Figure 24. (concluded)

# RECTANGULAR SUPERCRITICAL WING

MACH=0.699; 4 DEG STEADY ALPHA; 1 DEG UNSTEADY ALPHA,  $k=0.358$   
UNSTEADY PRESSURE DISTRIBUTIONS

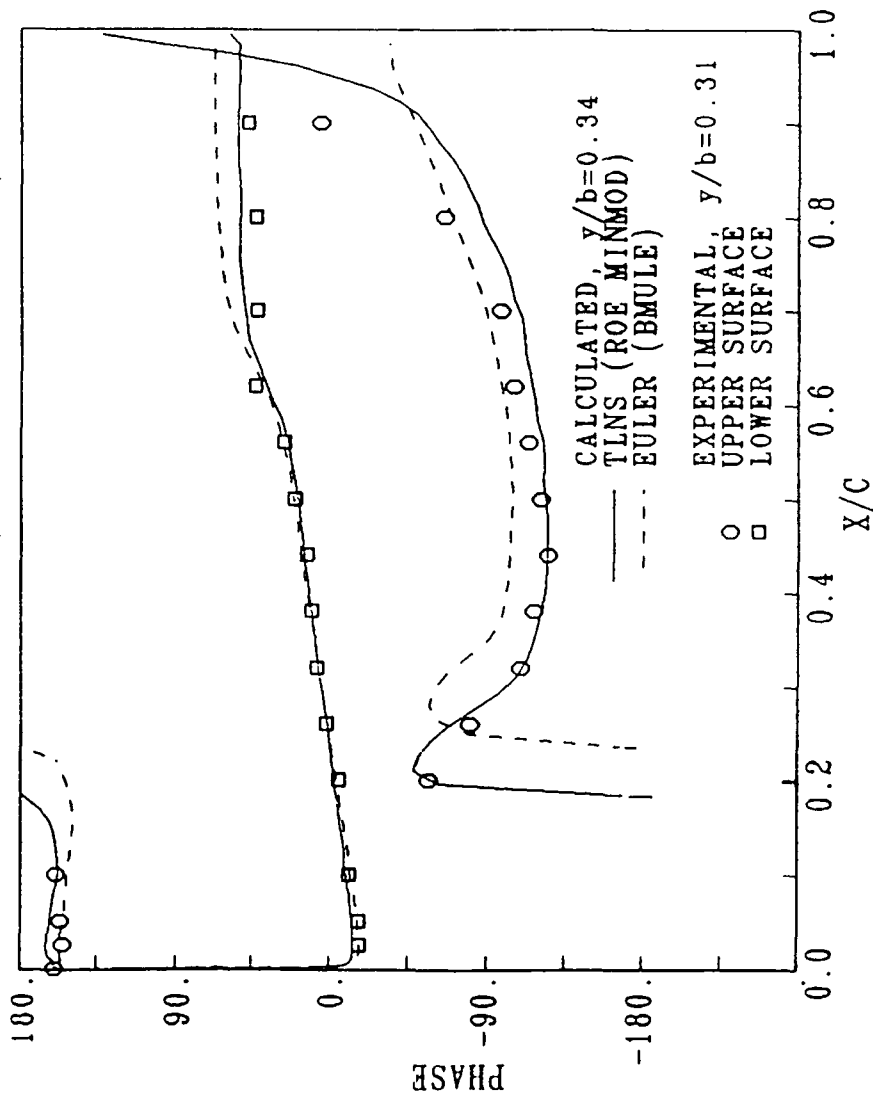


a. Magnitude at 34% semispan

Figure 25. Magnitude and phase of unsteady rectangular wing pressure distributions

# RECTANGULAR SUPERCritical WING

UNSTEADY PRESSURE DISTRIBUTIONS  
MACH=0.699; 4 DEG STEADY ALPHA; 1 DEG UNSTEADY ALPHA,  $k=0.358$

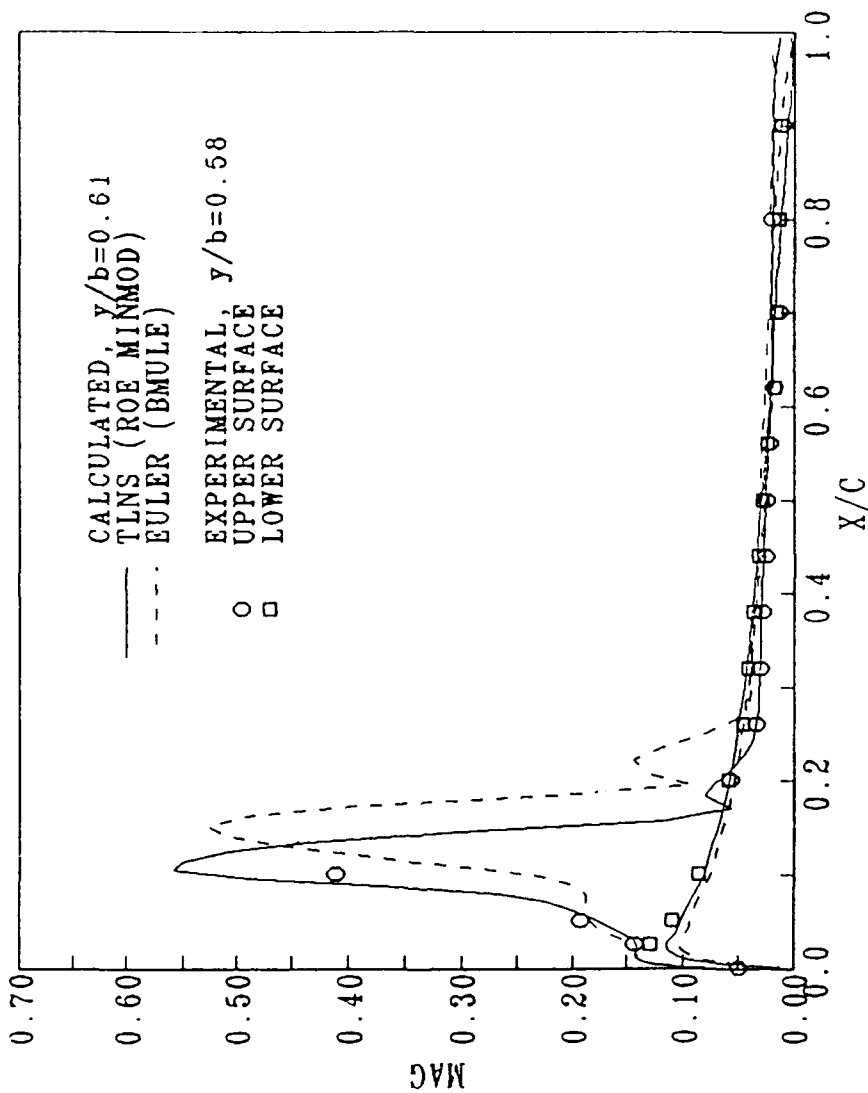


b. Phase at 34% semispan

Figure 25. (continued)

# RECTANGULAR SUPERCRITICAL WING

UNSTEADY PRESSURE DISTRIBUTIONS  
 $MACH=0.699$ ;  $4 \text{ DEG STEADY ALPHA}$ ;  $1 \text{ DEG UNSTEADY ALPHA}$ ,  $k=0.358$



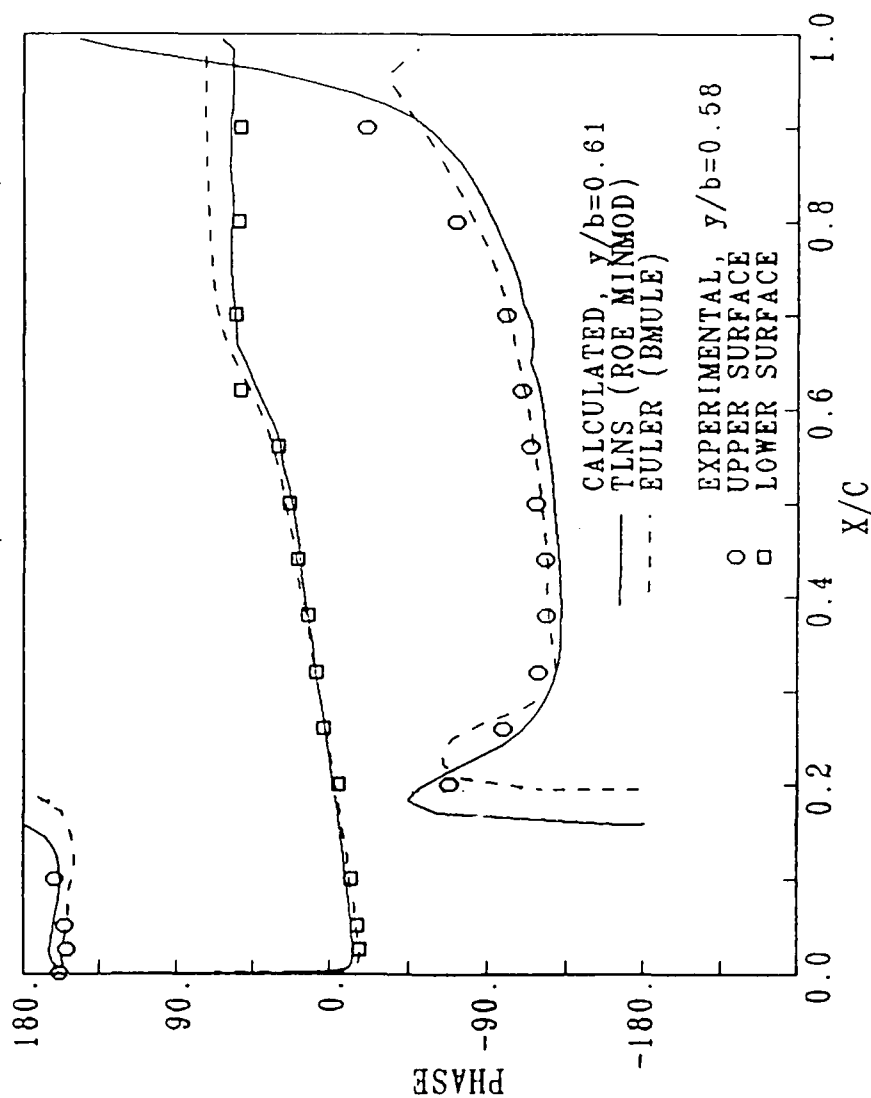
c. Magnitude at 61% semispan

Figure 25. (continued)



# RECTANGULAR SUPERCRITICAL WING

UNSTEADY PRESSURE DISTRIBUTIONS  
MACH=0.699; 4 DEG STEADY ALPHA; 1 DEG UNSTEADY ALPHA,  $k=0.358$

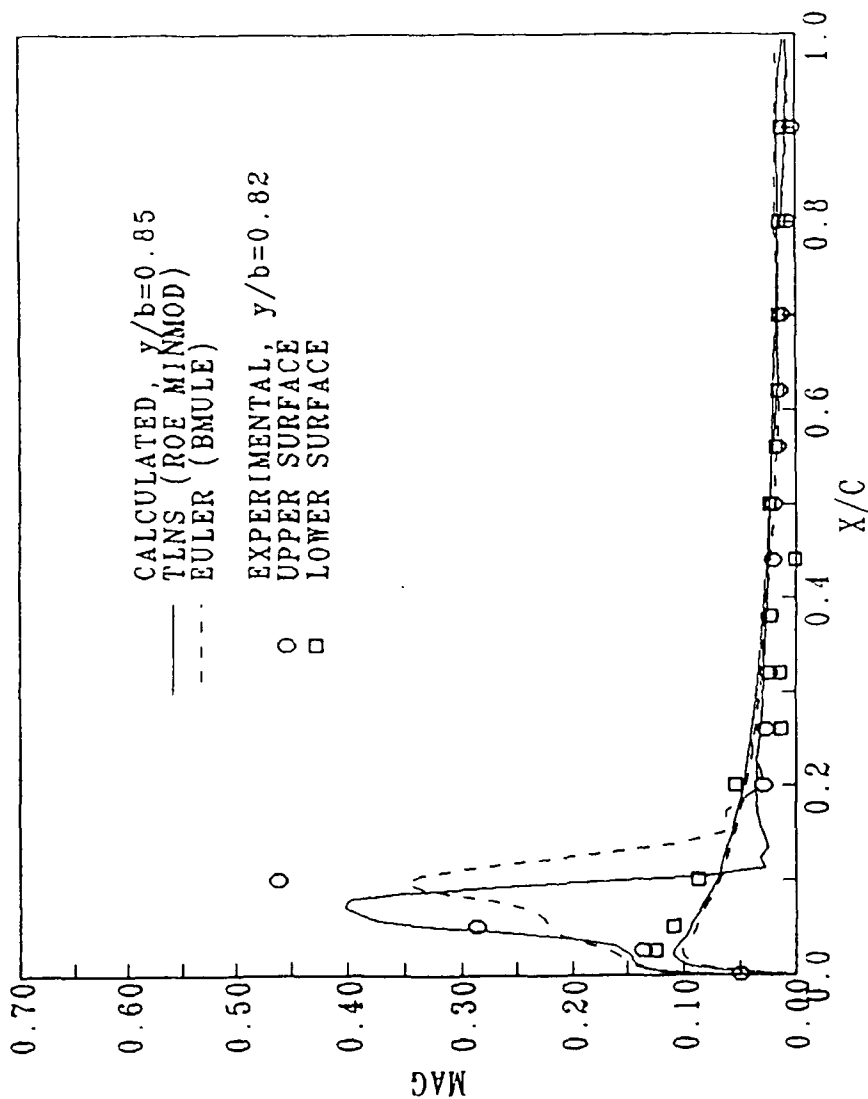


d. Phase at 61% semispan

Figure 25. (continued)

# RECTANGULAR SUPERCRITICAL WING

UNSTEADY PRESSURE DISTRIBUTIONS  
 MACH=0.699; 4 DEG STEADY ALPHA; 1 DEG UNSTEADY ALPHA,  $k=0.358$

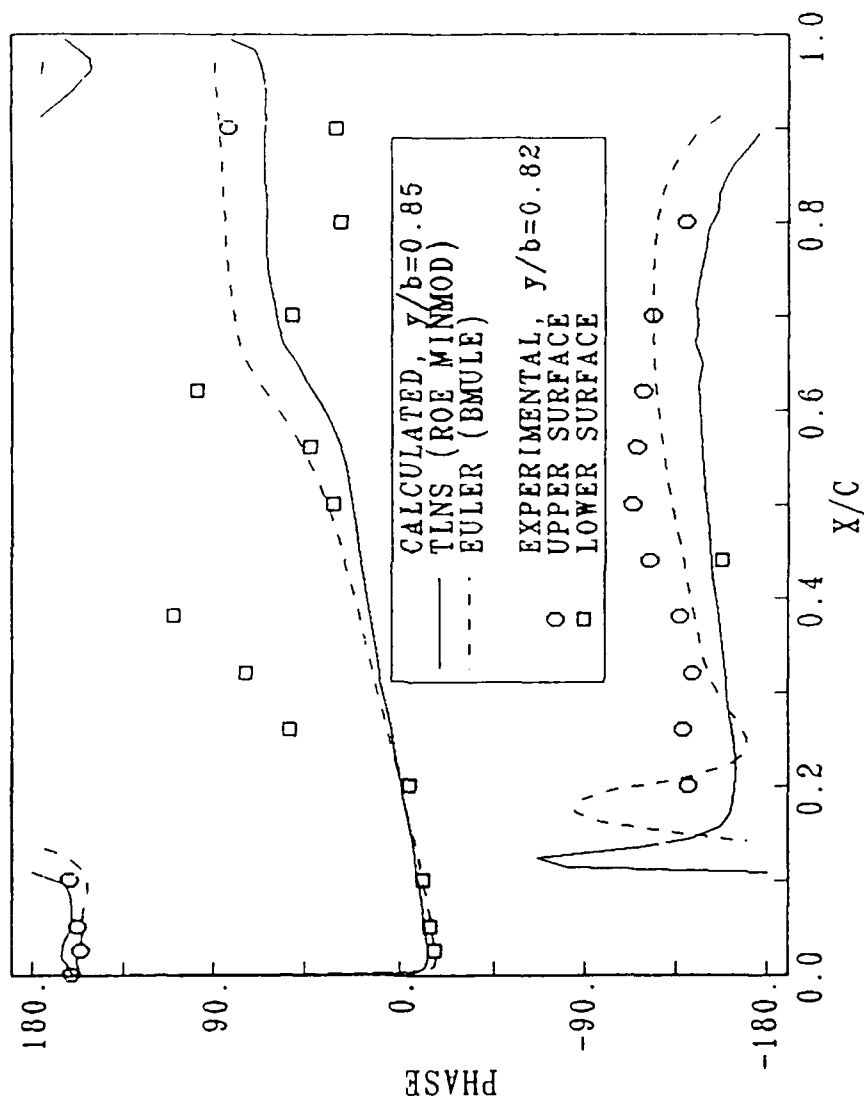


e. Magnitude at 85% semispan

Figure 25. (continued)

# RECTANGULAR SUPERCritical WING

UNSTEADY PRESSURE DISTRIBUTIONS  
 $MACH=0.699$ ;  $4 \text{ DEG STEADY ALPHA}$ ;  $1 \text{ DEG UNSTEADY ALPHA}$ ,  $k=0.350$

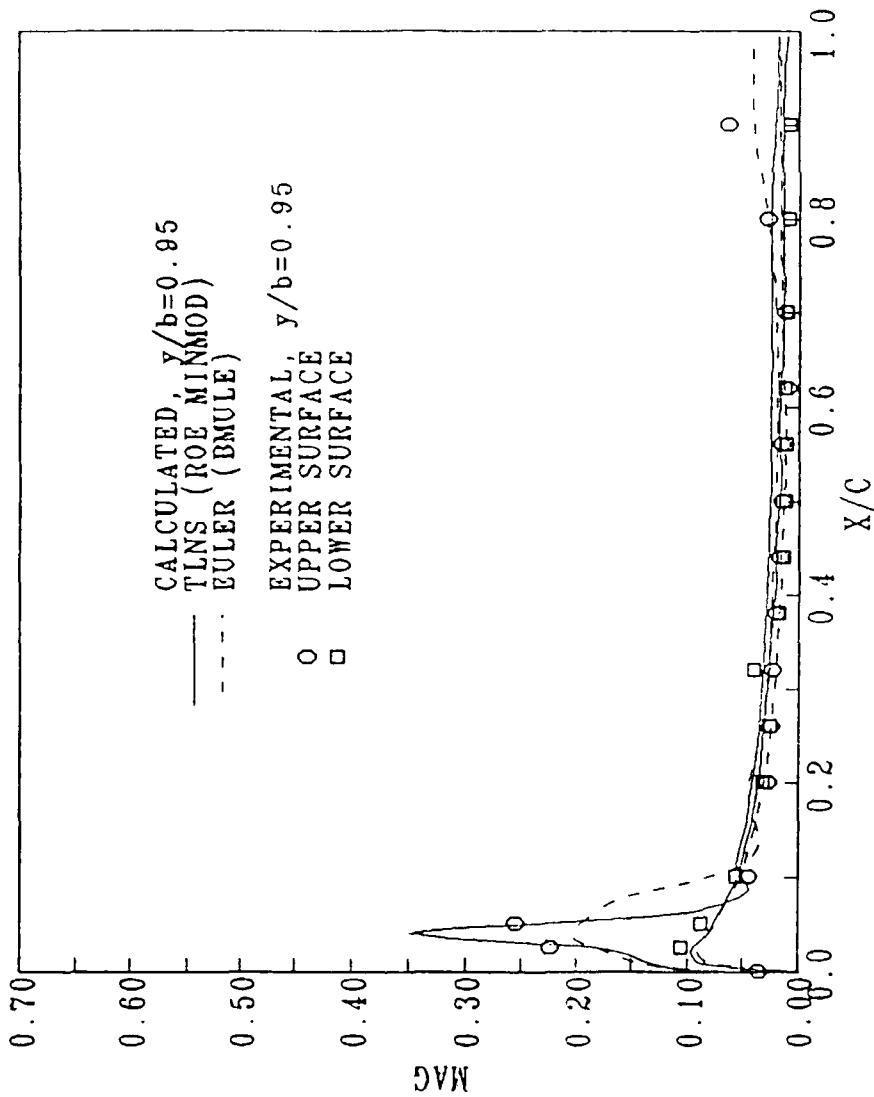


f. Phase at 85% semispan

Figure 25. (continued)

# RECTANGULAR SUPERCRITICAL WING

UNSTEADY PRESSURE DISTRIBUTIONS  
 MACH=0.699; 4 DEG STEADY ALPHA; 1 DEG UNSTEADY ALPHA,  $k=0.358$

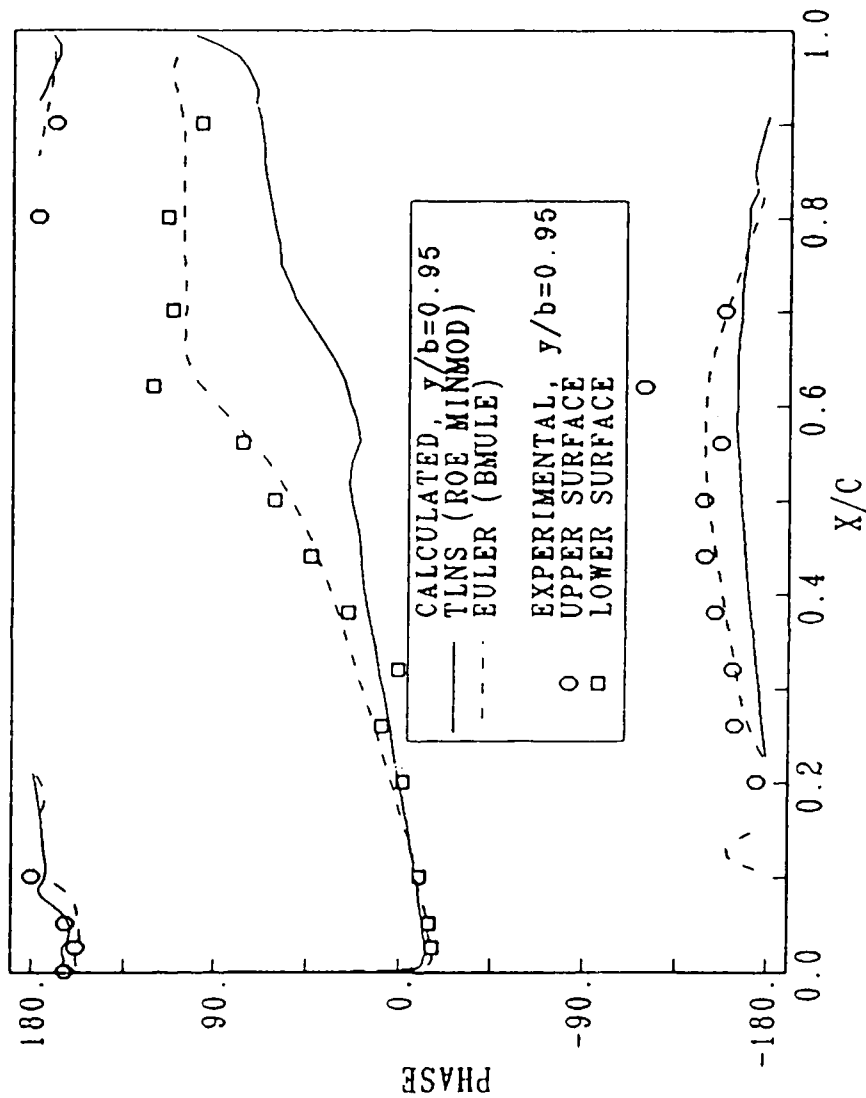


g. Magnitude at 95% semispan

Figure 25. (continued)

# RECTANGULAR SUPERCRITICAL WING

UNSTEADY PRESSURE DISTRIBUTIONS  
MACH=0.699; 4 DEG STEADY ALPHA; 1 DEG UNSTEADY ALPHA,  $k=0.358$



h. Phase at 95% semispan

Figure 25. (concluded)

# APPENDIX A CURVILINEAR TRANSFORMATION

The Navier-Stokes equations in Cartesian coordinates from Equation (2.7) are

$$\frac{\partial q}{\partial t} + \frac{\partial f}{\partial x} + \frac{\partial g}{\partial y} + \frac{\partial h}{\partial z} = 0 \quad (A.1)$$

The general curvilinear coordinates are given as

$$\begin{aligned} \xi &= \xi(x, y, z, t) \\ \eta &= \eta(x, y, z, t) \\ \zeta &= \zeta(x, y, z, t) \\ \tau &= \tau(t) \end{aligned} \quad (A.2)$$

Expanding the Cartesian coordinates in terms of the curvilinear coordinates using the chain rule gives

$$\begin{aligned} \frac{\partial}{\partial t} &= \frac{\partial \tau}{\partial t} \frac{\partial}{\partial \tau} + \frac{\partial \xi}{\partial t} \frac{\partial}{\partial \xi} + \frac{\partial \eta}{\partial t} \frac{\partial}{\partial \eta} + \frac{\partial \zeta}{\partial t} \frac{\partial}{\partial \zeta} \\ \frac{\partial}{\partial x} &= \frac{\partial \xi}{\partial x} \frac{\partial}{\partial \xi} + \frac{\partial \eta}{\partial x} \frac{\partial}{\partial \eta} + \frac{\partial \zeta}{\partial x} \frac{\partial}{\partial \zeta} \\ \frac{\partial}{\partial y} &= \frac{\partial \xi}{\partial y} \frac{\partial}{\partial \xi} + \frac{\partial \eta}{\partial y} \frac{\partial}{\partial \eta} + \frac{\partial \zeta}{\partial y} \frac{\partial}{\partial \zeta} \\ \frac{\partial}{\partial z} &= \frac{\partial \xi}{\partial z} \frac{\partial}{\partial \xi} + \frac{\partial \eta}{\partial z} \frac{\partial}{\partial \eta} + \frac{\partial \zeta}{\partial z} \frac{\partial}{\partial \zeta} \end{aligned} \quad (A.3)$$

The inverse of this relationship is determined by expanding the curvilinear coordinates in terms of Cartesian coordinates (in matrix form) as

$$\begin{bmatrix} \frac{\partial}{\partial \tau} \\ \frac{\partial}{\partial \xi} \\ \frac{\partial}{\partial \eta} \\ \frac{\partial}{\partial \zeta} \end{bmatrix} = \begin{bmatrix} t_T & x_T & y_T & z_T \\ 0 & x_\xi & y_\xi & z_\xi \\ 0 & x_\eta & y_\eta & z_\eta \\ 0 & x_\zeta & y_\zeta & z_\zeta \end{bmatrix} \begin{bmatrix} \frac{\partial}{\partial t} \\ \frac{\partial}{\partial x} \\ \frac{\partial}{\partial y} \\ \frac{\partial}{\partial z} \end{bmatrix} \quad (\text{A.4})$$

Let Equation (A.4) be written as

$$[ ] = [A]^{-1} [ ]$$

The jacobian of the transformation is given by the det of  $[A]$  defined as

$$\begin{aligned} J' &= |A| \\ &= t_T [x_\xi y_\eta z_\zeta + y_\xi z_\eta x_\zeta + z_\xi x_\eta y_\zeta - z_\xi y_\eta x_\zeta - y_\xi x_\eta z_\zeta - x_\xi z_\eta y_\zeta] \\ &= t_T J \end{aligned}$$

where,

$$J = [x_\xi (y_\eta z_\zeta - z_\eta y_\zeta) + y_\xi (z_\eta x_\zeta - x_\eta z_\zeta) + z_\xi (x_\eta y_\zeta - y_\eta x_\zeta)] \quad (\text{A.5})$$

The metric coefficients are determined by inverting the matrix  $A$  to yield

$$\xi_X = J^{-1} (y_\eta z_\zeta - z_\eta y_\zeta)$$

$$\xi_Y = J^{-1} (z_\eta x_\zeta - x_\eta z_\zeta)$$

$$\xi_Z = J^{-1} (x_\eta y_\zeta - y_\eta x_\zeta)$$

$$\eta_X = J^{-1} (z_\xi y_\zeta - y_\xi z_\zeta)$$

$$\eta_Y = J^{-1} (x_\xi z_\zeta - z_\xi x_\zeta)$$

$$\eta_Z = J^{-1} (y_\xi x_\zeta - x_\xi y_\zeta)$$

$$\zeta_x = J^{-1} (y_\xi z_\eta - z_\xi y_\eta)$$

$$\zeta_y = J^{-1} (z_\xi x_\eta - x_\xi z_\eta)$$

$$\zeta_z = J^{-1} (x_\xi y_\eta - y_\xi x_\eta)$$

$$\tau_t = \frac{1}{t_T} \quad (A.6)$$

$$\xi_t = \tau_t (-x_T \xi_x - y_T \xi_y - z_T \xi_z)$$

$$\eta_t = \tau_t (-x_T \eta_x - y_T \eta_y - z_T \eta_z)$$

$$\zeta_t = \tau_t (-x_T \zeta_x - y_T \zeta_y - z_T \zeta_z)$$

Substituting the expanded derivatives in Cartesian coordinates (Equation (A.3)) into the Navier-Stokes equations (Equation (A.1)) results in

$$\begin{aligned} & \tau_t \frac{\partial q}{\partial \tau} + \xi_t \frac{\partial q}{\partial \xi} + \eta_t \frac{\partial q}{\partial \eta} + \zeta_t \frac{\partial q}{\partial \zeta} + \\ & \xi_x \frac{\partial f}{\partial \xi} + \eta_x \frac{\partial f}{\partial \eta} + \zeta_x \frac{\partial f}{\partial \zeta} + \\ & \xi_y \frac{\partial g}{\partial \xi} + \eta_y \frac{\partial g}{\partial \eta} + \zeta_y \frac{\partial g}{\partial \zeta} + \\ & \xi_z \frac{\partial h}{\partial \xi} + \eta_z \frac{\partial h}{\partial \eta} + \zeta_z \frac{\partial h}{\partial \zeta} = 0 \end{aligned} \quad (A.7)$$

Then by multiplying Equation (A.7) by  $J'$  and using the chain rule Equation (A.1) becomes

$$\frac{\partial Q}{\partial \tau} + \frac{\partial F}{\partial \xi} + \frac{\partial G}{\partial \eta} + \frac{\partial H}{\partial \zeta} = 0 \quad (A.8)$$

where,



$$Q = J' T_t \begin{bmatrix} \rho \\ \rho u \\ \rho v \\ \rho w \\ e \end{bmatrix}$$

$$F = J' \begin{bmatrix} \rho U \\ \rho u U + \xi_x p - \tilde{T}_{\xi x} \\ \rho v U + \xi_y p - \tilde{T}_{\xi y} \\ \rho w U + \xi_z p - \tilde{T}_{\xi z} \\ (e+p)U - \xi_1 p - u\tilde{T}_{\xi x} - v\tilde{T}_{\xi y} - w\tilde{T}_{\xi z} + \Gamma_\xi \end{bmatrix}$$

$$G = J' \begin{bmatrix} \rho V \\ \rho u V + \eta_x p - \tilde{T}_{\eta x} \\ \rho v V + \eta_y p - \tilde{T}_{\eta y} \\ \rho w V + \eta_z p - \tilde{T}_{\eta z} \\ (e+p)V - \eta_1 p - u\tilde{T}_{\eta x} - v\tilde{T}_{\eta y} - w\tilde{T}_{\eta z} + \Gamma_\eta \end{bmatrix} \quad (A.9)$$

$$H = J' \begin{bmatrix} \rho W \\ \rho u W + \zeta_x p - \tilde{T}_{\zeta x} \\ \rho v W + \zeta_y p - \tilde{T}_{\zeta y} \\ \rho w W + \zeta_z p - \tilde{T}_{\zeta z} \\ (e+p)W - \zeta_1 p - u\tilde{T}_{\zeta x} - v\tilde{T}_{\zeta y} - w\tilde{T}_{\zeta z} + \Gamma_\zeta \end{bmatrix}$$

and

$$U = \xi_l + \xi_x u + \xi_y v + \xi_z w$$

$$V = \eta_l + \eta_x u + \eta_y v + \eta_z w$$

$$W = \zeta_l + \zeta_x u + \zeta_y v + \zeta_z w$$

$$\tilde{T}_{\xi x} = \xi_x \tau_{xx} + \xi_y \tau_{yx} + \xi_z \tau_{xz}$$

$$\tilde{T}_{\xi y} = \xi_x \tau_{xy} + \xi_y \tau_{yy} + \xi_z \tau_{zy}$$

$$\tilde{T}_{\xi z} = \xi_x \tau_{xz} + \xi_y \tau_{yz} + \xi_z \tau_{zz}$$

$$\tilde{T}_{\eta x} = \eta_x \tau_{xx} + \eta_y \tau_{yx} + \eta_z \tau_{xz}$$

$$\tilde{T}_{\eta y} = \eta_x \tau_{xy} + \eta_y \tau_{yy} + \eta_z \tau_{zy}$$

$$\tilde{T}_{\eta z} = \eta_x \tau_{xz} + \eta_y \tau_{yz} + \eta_z \tau_{zz}$$

(A.10)

$$\tilde{T}_{\zeta x} = \zeta_x \tau_{xx} + \zeta_y \tau_{yx} + \zeta_z \tau_{xz}$$

$$\tilde{T}_{\zeta y} = \zeta_x \tau_{xy} + \zeta_y \tau_{yy} + \zeta_z \tau_{zy}$$

$$\tilde{T}_{\zeta z} = \zeta_x \tau_{xz} + \zeta_y \tau_{yz} + \zeta_z \tau_{zz}$$

$$\Gamma_\xi = \xi_x q_x + \xi_y q_y + \xi_z q_z$$

$$\Gamma_\eta = \eta_x q_x + \eta_y q_y + \eta_z q_z$$

$$\Gamma_\zeta = \zeta_x q_x + \zeta_y q_y + \zeta_z q_z$$

The viscous stress tensors for the full Navier-Stokes equations are

$$\tau_{xx} = \frac{2\mu M_0}{3R_e} [2(\xi_x u_\xi + \eta_x u_\eta + \zeta_x u_\zeta) - (\xi_y v_\xi + \eta_y v_\eta + \zeta_y v_\zeta) - (\xi_z w_\xi + \eta_z w_\eta + \zeta_z w_\zeta)]$$

$$\tau_{yy} = \frac{2\mu M_0}{3R_e} [2(\xi_y v_\xi + \eta_y v_\eta + \zeta_y v_\zeta) - (\xi_x u_\xi + \eta_x u_\eta + \zeta_x u_\zeta) - (\xi_z w_\xi + \eta_z w_\eta + \zeta_z w_\zeta)]$$

$$\tau_{zz} = \frac{2\mu M_0}{3R_e} [2(\xi_z w_\xi + \eta_z w_\eta + \zeta_z w_\zeta) - (\xi_x u_\xi + \eta_x u_\eta + \zeta_x u_\zeta) - (\xi_y v_\xi + \eta_y v_\eta + \zeta_y v_\zeta)]$$

$$\tau_{xy} = \frac{\mu M_0}{R_e} [\xi_y u_\xi + \eta_y u_\eta + \zeta_y u_\zeta + \xi_x v_\xi + \eta_x v_\eta + \zeta_x v_\zeta]$$

$$\tau_{xz} = \frac{\mu M_0}{R_e} [\xi_z u_\xi + \eta_z u_\eta + \zeta_z u_\zeta + \xi_x w_\xi + \eta_x w_\eta + \zeta_x w_\zeta]$$

$$\tau_{yz} = \frac{\mu M_0}{R_e} [\xi_z v_\xi + \eta_z v_\eta + \zeta_z v_\zeta + \xi_y w_\xi + \eta_y w_\eta + \zeta_y w_\zeta]$$

and the heat flux terms are

$$q_x = \frac{1}{\gamma-1} \frac{\mu M_0}{P_r R_e} [\xi_x T_\xi + \eta_x T_\eta + \zeta_x T_\zeta]$$

$$q_y = \frac{1}{\gamma-1} \frac{\mu M_0}{P_r R_e} [\xi_y T_\xi + \eta_y T_\eta + \zeta_y T_\zeta]$$

$$q_z = \frac{1}{\gamma-1} \frac{\mu M_0}{P_r R_e} [\xi_z T_\xi + \eta_z T_\eta + \zeta_z T_\zeta]$$

## REFERENCES

1. Arabshahi, A., A Dynamic Multi-Block Approach to Solution of the Three-Dimensional Time-Dependent Euler Equations About Complex Configurations, Ph.D. Dissertation, Mississippi State University, to be published May 1989.
2. Belk, D. M., Unsteady Three-Dimensional Euler Equations Solutions on Dynamic Blocked Grids, Ph.D. Dissertation, Mississippi State University, Aug. 1986.
3. Whitfield, D. L., Janus, J. M., and Simpson, L. B., "Implicit Finite Volume High Resolution Wave-Split Scheme for Solving the Unsteady Three-Dimensional Euler and Navier-Stokes Equations on Stationary or Dynamic Grids," Mississippi State University Report MSSU-EIRS-ASE-88-2, Feb. 1988.
4. Steger, J. L., and Warming, R. F., "Flux Vector Splitting of the Inviscid Gasdynamic Equations with Application to Finite-Difference Methods," Journal of Computational Physics, Vol. 40, No. 2, pp. 263-293, April 1981.
5. Roe, P. L., "Approximate Riemann Solvers, Parameter Vector, and Difference Schemes," Journal of Computational Physics, Vol. 43 1981, pp. 357-372.
6. Gatlin, B., An Implicit, Upwind Method for Obtaining Symbiotic Solutions to the Thin-Layer Navier-Stokes Equations, Ph.D. Dissertation, Mississippi State University, Aug. 1987.
7. Whitfield, D. L., "Implicit Upwind Finite-Volume Scheme for the Three-Dimensional Euler Equations," Mississippi State University Report MSSU-EIRS-ASE-85-1, Sept. 1985.
8. Lijewski, L. E., "Transonic Flow Solutions on a Blunt, Body-Wing-Canard Configuration Using an Explicit Euler Solver," AIAA-87-2273, 5th Applied Aerodynamics Conference, Monterey, CA, August 1987.
9. Belk, D. M., and Whitfield, D. L., "Time-Accurate Euler Equation Solutions on Dynamic Blocked Grids," AIAA-87-1127-CP, Proceedings of the 8th Computational Fluid Dynamics Conference, Honolulu HI, June 1987.
10. van Leer, B., Thomas, J. L., Roe, P.L., and Newsome, R. W., "A Comparison of Numerical Flux Formulas for the Euler and Navier-Stokes Equations," Proceedings of the AIAA 8th Computational Fluid Dynamics Conference, pp. 36-39, AIAA paper 87-1104-CP, June 1987.
11. Chakravarthy, S. R., and Osher, S., "A New Class of High Accuracy TVD Schemes for Hyperbolic Conservation Laws," AIAA Paper 85-0363,

- Jan. 1985.
12. Chakravarthy, S. R., Szema, K-Y., Goldberg, U. C., Gorski, J. J., and Osher, S., "Application of a New Class of High Accuracy TVD Schemes to the Navier-Stokes Equations," AIAA Paper 85-0165, Jan. 1985.
  13. Chakravarthy, S. R., "The Versatility and Reliability of Euler Solvers Based on High-Accuracy TVD Formulations," AIAA Paper 86-0243, Jan. 1986.
  14. Chakravarthy, S. R., "Essentially Non-Oscillatory Shock-Capturing Schemes of Arbitrarily-High Accuracy," AIAA Paper 86-0339, Jan. 1986.
  15. Janus, J. M., Advanced 3-D CFD Algorithm for Turbomachinery, Ph.D. Dissertation, Mississippi State University, to be published May 1989.
  16. Lijewski, L. E., "Transonic Euler Solutions on Mutually Interfering Finned Bodies," AIAA-89-264, to be presented at AIAA 27th Aerospace Sciences Meeting, Reno, Jan. 1989.
  17. Rai, M. M., and Chakravarthy, S. R., "An Implicit Form for the Osher Upwind Scheme," AIAA Journal, Vol. 24, No. 5, pp. 735 - 743, May 1986.
  18. Pulliam, T. H., and Steger, J. L., "Implicit Finite-Difference Simulations of Three-Dimensional Compressible Flow," AIAA Journal, Vol. 18, No. 2, pp. 159-167, Feb. 1980.
  19. Briley, W. R., and McDonald, H., "Solution of the Multidimensional Compressible Navier-Stokes Equations by a Generalized Implicit Method," Journal of Computational Physics, Vol. 24, pp. 372-397, 1977.
  20. Beam, R. M., and Warming, R. F., "An Implicit Finite-Difference Algorithm for Hyperbolic Systems in Conservation Law Form," Journal of Computational Physics, Vol. 22, pp. 87-110, 1976.
  21. Whitfield, D. L., and Janus, J. M., "Three-Dimensional Unsteady Euler Equations Solutions Using Flux Vector Splitting," AIAA Paper 84-1552, June 1985.
  22. Barth, T. J., "Analysis of Implicit Local Linearization Techniques for Upwind and TVD Algorithms," AIAA Paper 87-0595, Jan. 1987.
  23. Jeffery, A., Quasilinear Hyperbolic Systems and Waves, Pitman Publishing, San Francisco, 1976.
  24. Roe, P. L., and Pike, J., "Efficient Construction and Utilization of Approximate Riemann Solutions," In Computing Methods in Applied

Sciences and Engineering, ed. R. Glowinski and J. L. Lions, 6:499-518. Amsterdam: North-Holland, 1984.

25. Osher, S., and Chakravarthy, S. R., "Very High Order Accurate TVD Schemes," ICASE Report No. 84-44, Sept. 1984.
26. Baldwin, B. S., and Lomax, H., "Thin-Layer Approximation and Algebraic Model for Separated Turbulent Flows," AIAA Paper 78-257, Jan. 1978.
27. Landon, R. H., "NACA 0012. Oscillatory and Transient Pitching," Compendium of Unsteady Aerodynamic Measurements, AGARD-R-702, August 1982.
28. Thompson, J. F., and Gatlin, B., "Program Eagle User's Manual," AFATL-TR-88-117, VOL II and III, Sept. 1988.
29. Ortega, J. M., and Rheinboldt, W. C., Iterative Solution of Nonlinear Equations in Several Variables, Academic Press, 1970, pp. 181-187.
30. Swanson, R. C., and Turkel, E., "Artificial Dissipation and Central Difference Schemes for the Euler and Navier-Stokes Equations," Proceedings of the AIAA 8th Computational Fluid Dynamics Conference, pp. 55-69, AIAA Paper 87-1107-CP, June 1987.
31. Cook, P. J., McDonald, M. A., and Firmin, M. C. P., "Aerofoil RAE 2822—Pressure Distributions and Boundary Layer and Wake Measurements," AGARD-AR-138, 1979.
32. Coakley, T. J., "Numerical Simulation of Transonic Airfoil Flows," AIAA Paper 87-0416, Jan. 1987.
33. Rumsey, C. L., Taylor, S. L., Thomas, J. L., and Anderson, W. K., "Application of an Upwind Navier-Stokes Code to Two-Dimensional Transonic Airfoil Flow," AIAA Paper 87-0413, Jan. 1987.
34. Schmitt, V., and Charpin, F., "Pressure Distributions of the ONERA-M6 Wing in Transonic Flow," AIAA Paper 83-1804, July 1983.
35. Ricketts, R. H., Sandford, M. C., Watson, J. J., and Seidel, D. A., "Subsonic and Transonic Unsteady and Steady-Pressure Measurements on a Rectangular Supercritical Wing Oscillated in Pitch," NASA TM-85765, August 1984.